Analysis and control of a tunneling current measurement system

Irfan Ahmad

▶ To cite this version:

Irfan Ahmad. Analysis and control of a tunneling current measurement system. Automatic Control Engineering. Université de Grenoble, 2011. English. NNT : . tel-00663060v1

HAL Id: tel-00663060
https://theses.hal.science/tel-00663060v1

Submitted on 25 Jan 2012 (v1), last revised 25 Jul 2012 (v2)

UNIVERSITÉ DE GRENOBLE

THÈSE

Pour obtenir le grade de

DOCTEUR DE L'UNIVERSITÉ DE GRENOBLE

Spécialité : **AUTOMATIQUE - PRODUCTIQUE**

Arrêté ministériel : 7 août 2006

Présentée par

« Irfan AHMAD »

Thèse dirigée par **« Alina VODA »** et
codirigée par **« Gildas BESANÇON »**

préparée au sein du **Laboratoire GIPSA-Lab (Grenoble Images Parole Signal Automatique)**
dans **l'École Doctorale EEATS (Electronique, Electrotechnique, Automatique et Traitement du Signal)**

Analyse et commande d'un système de mesure à courant tunnel

Thèse soutenue publiquement le **20 juillet 2011**,
devant le jury composé de :

M. Jean-Marc THIRIET
Professeur, Université Joseph Fourier, France (Président)
M. Antoine FERREIRA
Professeur, ENSI de Bourges, France (Rapporteur)
M. Adrian FILIPESCU
Professeur, Université Dunarea de Jos de Galati, Roumanie (Rapporteur)
M. Alireza KARIMI
Professeur, Ecole Polytechnique Fédérale de Lausanne, Suisse (Examinateur)
Mme. Alina VODA
Maître de conférences, Université Joseph Fourier, France (Directeur de thèse)
M. Gildas BESANÇON
Professeur, Grenoble INP, France (Codirecteur de thèse)
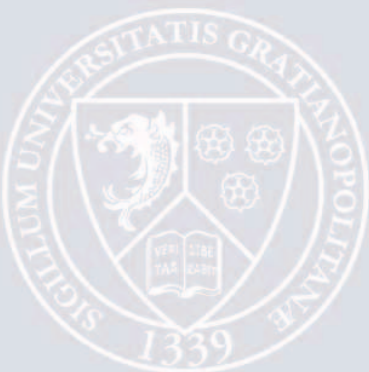
To my father (R.I.P)

Acknowledgements

Table of contents

List of Figures

List of Tables

List of Notations

Chapter 2: State of the Art

$\hbar$	Reduced Planck constant
m	Electron mass
E	Electron energy
p	Electron momentum
$V(x)$	Potential barrier
$\psi(x)$	Wave function of electron
ψ_I and ψ_{III}	Wave function of electron outside potential barrier
ψ_{II}	Wave function of electron within potential barrier
k_1	Wave number outside the potential barrier
k_2	Wave number within the potential barrier
A	Amplitude of the incoming wave function of electron
B	Amplitude of the reflected portion of wave function of electron
C	Amplitude of the wave function crossing within the potential barrier
D	Amplitude of the wave function reflecting within the potential barrier
F	Amplitude of the wave function transmitted through the potential barrier
T	Transmission coefficient
R	Reflection coefficient
i_t	Tunneling current
$L = d$	Distance between two electrodes
v_b	Potential difference applied between two electrodes
g	Proportionality constant of tunneling current
k	Constant of tunneling current ($k = 2\sqrt{2m}/\hbar = 1.025\ eV^{1/2-1}$)
ϕ	Work function
G_{amp}	Current sensor gain
C_1	Constant term ($C_1 = log_{10}(G_{amp} \cdot g \cdot v_b)$)
γ_0	Sensitivity of piezoelectric actuator
ω_0	Resonance frequency of piezoelectric actuator
Q	Quality factor of piezoelectric actuator
$G_a(s)$	Transfer function of piezoelectric actuator

Chapter 3: Control Problem and Robust Design

List of Tables

Chapter 4: Experimental Analysis and Control Results

v_y	Measured voltage
v_e	Error voltage
v_{ref}	Reference voltage
$y(t)$	Output signal
$u(t)$	Control signal
$[a_1, b_1]$	Plant parameters
θ^T	Vector of plant parameters
$\phi^T(t)$	Vector of measurement signal
$R(q^{-1})$	Controller polynomial
$S(q^{-1})$	Controller polynomial
$T(q^{-1})$	Controller polynomial
$r(t)$	Input excitation signal
$\hat{y}^\circ(t+1)$	Predicted output at the instant t
$[\hat{a}_1(t), \hat{b}_1(t)]$	Estimated parameters of plant at time t
$\hat{\theta}^T(t)$	Vector of estimated parameters at time t
$\hat{y}^\circ(t+1)$	*A priori* prediction
$\varepsilon^\circ_{CL}(t+1)$	*A priori* prediction error
$\hat{y}(t+1)$	*A posteriori* predictor output
$\varepsilon_{CL}(t+1)$	*A posteriori* prediction error
$S_o(z^{-1})$	Output sensitivity function
$T(z^{-1})$	Complementary sensitivity function
$KS_o(z^{-1})$	Input sensitivity function
G_n	Noise transfer function
ω_M	Maximum allowed variations of sample surface
z_S	Sample surface variations
W_P	Performance weighting function
W_I	Uncertainty weighting function

Chapter 5: Towards MIMO Analysis and Control

v_{1h}	Output of the voltage amplifier (in horizontal direction)
G_v	Gain of the voltage amplifier
u_h	Input voltage of the voltage amplifier (in horizontal direction)
v_{1h}	Input voltage of the piezoelectric actuator (in horizontal direction)
z_h	Output displacement of the piezoelectric actuator (in horizontal direction)
ζ_{ah}	Damping of the piezoelectric actuator (in horizontal direction)
ω_{ah}	Bandwidth of the piezoelectric actuator (in horizontal direction)
G_{ah}	Gain of the piezoelectric actuator (in horizontal direction)

List of Tables

v_h	Output voltage of the capacitive sensor (in horizontal direction)
G_c	Gain of the capacitive sensor (in horizontal direction)
$\hat{z}_h$	Retrieved displacement of the piezoelectric actuator (in horizontal direction)
z_c	Output (positioning error) of the coupling dynamics
ω_{fc}	Bandwidth (scan speed for maximum positioning error)
G_{fc}	Gain (maximum positioning error)
u_v	Input voltage of the voltage amplifier (in vertical direction)
v_{1v}	Output voltage of the voltage amplifier (in vertical direction)
ω_{vv}	Bandwidth of the voltage amplifier (in vertical direction)
z_v	Output displacement of the piezoelectric actuator (in vertical direction)
G_{av}	Gain of the piezoelectric actuator (in vertical direction)
d	Vertical distance between tip and sample surface
z_s	Unknown surface variations
i_t	Tunneling current
i_{eq}	Tunneling current at operating point
k	Constant of tunneling current
v_{2v}	Output voltage of current sensor (CVC)
G_{cv}	Gain of the current sensor
v_v	Measured output voltage of the vertical system
n	Measurement noise
P_D	closed-loop dominant poles
P_F	Auxiliary closed-loop poles
H_S	Pre-specified fixed filter of controller
$x(t)$	State vector
$u(t)$	Input vector
$y(t)$	Output vector
A, B, C, D	System matrices
K	State feedback gain matrix
J	Cost function
Q	Weighting matrix for the states
R	Weighting matrix for the input signals

List of Publications

Journal paper

- **2011**

    1 **Robust digital control for high performance tunneling current measurement system** (Ahmad I., Voda A., Besançon G., Buche G.), *In IFAC Control Engineering Practice*, 2011. (Revised version submitted)

Book chapter

- **2010**

    1 **Controller design and analysis for high-performance Scanning Tunneling Microscope** (Ahmad I., Voda A., Besançon G.), *In Micro, Nanosystems and Systems on Chips: Modeling, Control, and Estimation, International Wiley-ISTE publications*, 2010.

International conference proceedings

- **2010**

    4 **Robust H$_\infty$ control of a scanning tunneling microscope under parametric uncertainties** (Ahmad I., Voda A., Besançon G.), *In IFAC American Control Conference, Baltimore, Maryland, USA*, 2010.

- **2010**

    3 **Commande robuste H$_\infty$ d'un microscope à effet tunnel en présence d'incertitudes paramétriques** (Ahmad I., Blanvillain S., Voda A., Besançon G.), *In Conférence Internationale Francophone d'Automatique, Nancy, France*, 2010.

- **2009**

  2 **H$_\infty$ controller design for high-performance scanning tunneling microscope** (Ahmad I., Voda A., Besançon G.), *In IEEE Conference on Decision and Control, Shanghai, China*, 2009.

- **2008**

  1 **Controller design for a closed-loop scanning tunneling microscope** (Ahmad I., Voda A., Besançon G.), *In IEEE Conference on Automation Science and Engineering, Washington DC, USA*, 2008.

INTRODUCTION

General context

The recent years have witnessed the explosive growth of an emerging scientific field: *nanosciences and nanotechnology*, which is the study of manipulating matter with atomic and molecular scale. This explosive growth started around two and a half decades before when Gerd Binnig and Heinrich Rohrer from IBM laboratory, Zurich got Nobel Prize in physics by their invention of Scanning Tunneling Microscope (STM) with the ability to characterize any conductive matter morphology with atomic scale resolution [Binnig & Rohrer, 1986]. Nanotechnology is very diverse and this has fundamentally changed the research in numerous areas, including physics, biology, chemistry, electronics and materials science. Nanopositioning is an important aspect of research in nanotechnology and it involves precision control and manipulation of devices and materials at a nanometer scale. The quality in terms of precision of the measured signal at nanometer scale is one of the key requirements where the interface (coupling) between physics, electronics, thermal and mechanical sciences play crucial role. One of the ways to achieve this key requirement is the use of some better control techniques. This manuscript is written focusing on control design techniques for this emerging field of science.

Problems statement

Many new problems have emerged working at nanometer scale. For example, the small size and extreme fragility of the micro or nanoscale objects make them difficult to handle. Ultrahigh positioning precision is one of the pivotal requirements in many

applications of nanotechnology. The precision of measured signal at nanometer scale is highly sensitive to the operating conditions which introduce the major difficulty in terms of repeatability. Besides this requirement of high precision, there is also an increasing need of high bandwidth for fast speed operations. To meet the dual goal of high precision at high bandwidth, many novel actuators and sensors have been studied and developed. However, the precision is adversely affected by the sensor noise as well as actuator nonlinearities such as hysteresis, and drifts due to creep phenomenon. Additional external environmental disturbances influence the precision of measured signal as well. Quantum mechanical effects are very important at this nanometer scale. Indeed, micro and nano systems are complex to study and the techniques of automatic control become essential. A precision and accuracy of the measured signal at nanometer scale can not be achieved without a better control scheme. In addition, physical limitations and non-linearities in the control loop are limiting factors to be considered in order to get better performances. The control loop stability and robustness and its tradeoff with desired performances should not be neglected in order to achieve optimal solutions.

Thesis objectives and contribution

The objective of this thesis was to study, propose and experimentally validate modern control laws for high precision nanopositioning using tunneling current, while working at nanometer scale. The controller must indeed be robust and have a capability to reject the external disturbances in order to achieve the desired performances. The main contribution of this thesis is highlighted here:

1. Analysis of a system of tunneling current (quantum mechanical phenomenon which occurs at nanometer scale) measurement with proposition of a corresponding dynamic modeling and formulation of the related control problem with desired measurement performances.

2. Synthesis of modern robust control techniques for the considered system (in the

vertical z-direction) in order to achieve the desired performances in terms of measurement precision, large closed loop bandwidth with robustness and stability.

3. Realtime experimental validation with time and frequency domain comparison between proposed and conventional control techniques for the considered system over an experimental setup (at ambient atmosphere) developed in Gipsa-lab, Grenoble.

4. For the application of scanning (in the horizontal x-direction), proposition of a dynamic modeling of the MIMO plant having horizontal, vertical and cross coupling dynamics and synthesis of a MIMO controller in order to reduce the coupling-caused positioning error for the tunneling current measurement system (in the vertical z-direction).

Manuscript organization

This thesis manuscript is organized as follows:

Chapter 2: This chapter presents very briefly the quantum mechanical phenomenon of tunneling current, its different applications in nanosciences and the associated control techniques. The last part of this chapter highlights the control issues for nanopositioning.

Chapter 3: This chapter is related to the first two points of the thesis contribution as mentioned above. It starts with the motivation of the work and brief description of the considered system of tunneling current measurement. Then, a corresponding system dynamic modeling is proposed and a related control problem with desired measurement performances are formulated. Measurement requirements are translated into control requirements and then modern robust controllers based on pole placement with sensitivity function shaping technique and mixed sensitivity H_∞ controller are proposed. Finally, the performance of the considered system of tunneling current is analyzed with the proposed controllers, and a comparison is performed by simulation results with the more classically used PI controller for this type of systems.

Chapter 4: This chapter is related to the third point of the thesis contribution, in order to experimentally validate the proposed controllers of chapter 3 and to perform a

comparison with the more classical PI controller for the considered system of tunneling current. It starts with all necessary details about the experimental setup developed in Gipsa-lab, Grenoble. Then, system identification is performed and closed loop sensitivity functions are identified experimentally with all control techniques of chapter 3. Time domain experimental results are subsequently presented, and finally, based on all time and frequency domain results, a comparison is performed between all control techniques for the considered system of tunneling current.

Chapter 5: This chapter is related to the last point of the thesis contribution, where scanning related issues in the horizontal x-direction are considered. It starts by highlighting very briefly the coupling-caused positioning error and also the dynamic nonlinearities (hysteresis and creep) of the piezoelectric actuator. Then, corresponding dynamic modeling of the MIMO plant (having horizontal, vertical and cross coupling dynamics) is proposed and some experimental results related to the dynamic nonlinearities of the piezoelectric actuator (in open and in closed-loop) are presented. On this basis, a MIMO controller is designed and the measurement precision of the tunneling current is analyzed (in simulations) in the presence of coupling-caused positioning error in the vertical z-direction of the considered system.

Chapter 6: Finally, the general conclusion and perspectives of this work are presented in this last chapter of the manuscript.

STATE OF THE ART

Nanotechnology is an emerging field of science, where nanopositioning is one of the fundamental requirement. Different control issues in terms of ultrahigh positioning accuracy with large closed-loop bandwidth, robustness, repeatability, presence of noise, physical limitations and non-linearities in the control loop etc., are the great limitations in order to enhance the performances of the nanopositioning systems. The study and development of new actuators and sensors for high performance nanopositioning systems are the recent topics in the research community. Among the phenomena of interest at nanoscale, one can find the tunneling current, which was practically experienced first time in 1980s and has vast applications in the domain of nanotechnology e.g. surface imaging with atomic scale resolution, nanopositioning tunneling sensor and also tunneling accelerometer with high sensitivity. This thesis is focused on the control design issues in a tunneling current measurement system.

The tunneling phenomenon is briefly presented in Section 2.1 and its different applications are highlighted in Section 2.2.

The piezoelectric effect which is also of interest for nanosystems is described in Section 2.3.

The control issues associated with the the problem of nanopositioning in terms of performance compromises, dynamic nonlinearities, modeling errors and coupling effects are presented in Section 2.4.

Finally, Section 2.5 draws some conclusions.

In early 1980s, Gerd Binnig and Heinrich Rohrer first practically experienced the phenomenon of tunneling current when an extremely sharp metallic electrically charged tip is approached at the vicinity of a conductive sample surface (distance between tip apex and sample surface in the range of $0.1 - 1 \times 10^{-9}$ m) [Binnig & Rohrer, 1986]. An important application of this tunneling current with the ability to scan the tip against the sample surface was the invention of Scanning Tunneling Microscope (STM). It was the first member of the family of Scanning Probe Microscopes (SPM) that can characterize the surface morphology with atomic resolution. The manipulation and interrogation at nanometer scale after the invention of STM necessitate the positioning systems with atomic scale resolution, where nanopositioning is needed to scan the probe (tip) over a sample surface. Tunneling current is also now widely used to measure the accelerations down to sub-micro-g [Rockstad et al., 1996], [Liu et al., 1998], [Liu & Kenny, 2001] and to sense sub-micrometer displacements [Bocko, 1990], [Ekinci, 2005], [Blanvillain et al., 2009].

In the next section, a brief introduction of the phenomenon of tunneling current is presented.

2.1 Tunneling Phenomenon

According to classical mechanics, a particle (electron) that does not have enough energy to overcome a potential barrier, can not pass through it. On the contrary, in quantum mechanics [Liboff, 1998], an electron is described by a wave function which can have a non-zero probability of tunneling through a potential barrier, even if its energy is lower than the barrier. When an electron moves through the barrier in this fashion, it is called *tunneling effect*. If the barrier is thin enough then there is always a probability of observing an electron on the other side of the region. *Tunneling current* falls in the category of quantum mechanics. In this section, we will describe very briefly the phenomenon of tunneling current, although the complete details can be found in [Chen, 2008].

Mathematically, in **classical mechanics**, an electron in a potential $V(x)$ is described by:

$$\frac{p^2}{2m} + V(x) = E \tag{2.1.1}$$

where m is the electron mass, E is its energy and p the momentum. In regions where $E > V(x)$, the electron has a non-zero momentum $p = [2m(E - V)]^{1/2}$. On the other hand, if $E < V(x)$, the electron can not penetrate into any region or a potential barrier as mentioned above.

In case of **quantum mechanics**, the electron is described by a wave function $\psi(x)$, which satisfies the Schrödinger equation [Landau & Lifshitz, 1977]:

$$\left(-\frac{\hbar^2}{2m}\frac{\partial^2}{\partial x^2} + V(x)\right)\psi(x) = E\psi(x) \tag{2.1.2}$$

where $\hbar$ is the reduced Planck constant. The potential barrier can be generated by an empty space between two electrodes. For simplification, the potential between the points $x = 0$ and $x = L$ (Region II) can be considered as constant, and also before $x = 0$ (Region I) and after $x = L$ (Region III), the potential barrier is considered zero (see Fig. 2.1). Under such conditions, the potential barrier $V(x)$ does not vary with time, so we can use time independent (one dimensional) Schrödinger equation for all three regions as follows:

$$Region\ I\ :\ \ \frac{\partial^2\psi_I}{\partial x^2} + \frac{2m}{\hbar^2}E\psi_I = 0 \tag{2.1.3}$$

$$Region\ II\ :\ \ \frac{\partial^2\psi_{II}}{\partial x^2} - \frac{2m}{\hbar^2}(V - E)\psi_{II} = 0 \tag{2.1.4}$$

$$Region\ III\ :\ \ \frac{\partial^2\psi_{III}}{\partial x^2} + \frac{2m}{\hbar^2}E\psi_{III} = 0 \tag{2.1.5}$$

The solutions ψ_I, ψ_{II} and ψ_{III} of the equations (Eq. (2.1.3) to Eq. (2.1.5)) are given respectively by:

$$\psi_I\ =\ \ Ae^{ik_1x} + Be^{-ik_1x} \tag{2.1.6}$$
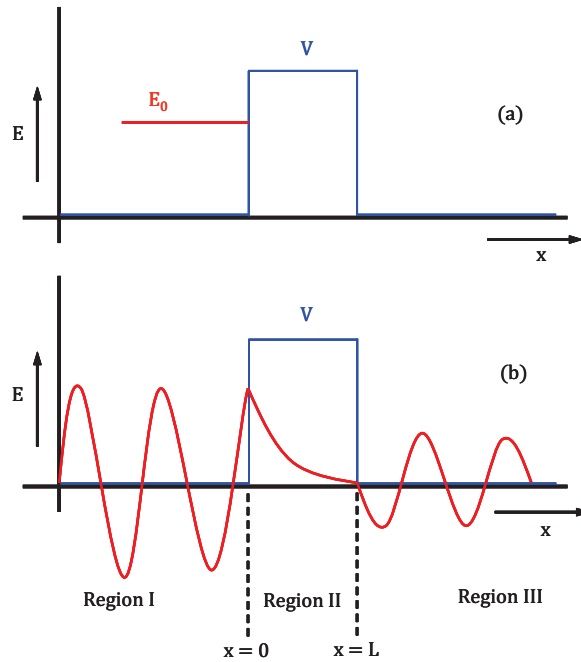
Figure 2.1: (a) Case of classical mechanics: a traveling electron of energy E_0 encountering a potential barrier of height V. In this case, the electron would be unable to pass through the potential barrier and would be reflected. (b) Case of quantum mechanics: the electron interacting with the potential barrier of height V. The electron's wave function acts as a travelling wave before (Region I) and after (Region III) the barrier, but like an exponential under the potential barrier (Region II). In this fashion, the electron has a non-zero probability of tunneling through a potential barrier.

$$\psi_{II} = Ce^{-k_2 x} + De^{k_2 x} \tag{2.1.7}$$

$$\psi_{III} = Fe^{ik_1 x} \tag{2.1.8}$$

where, $k_1 = \sqrt{2mE}/\hbar$ is wave number outside the barrier (Region I and Region III) and $k_2 = \sqrt{2m(V-E)}/\hbar$ the wave number within the barrier (Region II). The coefficient A is the amplitude of the incoming wave function (Region I), B is the amplitude of the reflected portion of the wave function (Region I), and F is the part of the wave function that is transmitted through the barrier (Region III). We can see the oscillatory behavior of ψ_I and ψ_{III} in Eq. (2.1.6) and Eq. (2.1.8) outside the barrier and exponential behavior of ψ_{II} in Eq. (2.1.7) within the barrier, which means that the electron's wave function acts as a traveling wave before and after the barrier, but like an exponential under the potential barrier as shown in Fig. 2.1. These solutions will help to define the coefficient of transmission ($T = |F/A|^2$) which is the ratio of number of electrons that reach the barrier

to those that emerge from the barrier. In the similar way, the coefficient of reflection can be defined with $R = |B/A|^2$. The transmission coefficient (T) and the reflection coefficient (R) obey the relation $T + R = 1$. When the proper boundary conditions are applied, it can be shown that the transmittance varies exponentially with the width of the potential barrier. So a small increase in the width of the potential barrier leads to a large decrease in the transmittance through the barrier.

The intensity of current is directly proportional to the probability of electrons passing through the barrier, that is $|\psi_{II}|^2$. The term $De^{k_2 x}$ of Eq. (2.1.7) indicates the probability of electron passing through the potential barrier. The term $Ce^{-k_2 x}$ of Eq. (2.1.7) indicates the bidirectional motion of electron in Region II, but it can be neglected for very thin potential barriers. Now, having Schrödinger equation (Eq. (2.1.4)) and its possible solution (Eq. (2.1.7)) for Region II, we can write:

$$|\psi_{II}|^2 \propto e^{-2\sqrt{\frac{2m(V-E)}{\hbar^2}}L} \tag{2.1.9}$$

For two conductive electrodes (like Region I and Region III) of same nature with weekly polarized, the quantity $(V - E)$ can be replaced with the work function (ϕ) of the conductive materials. Now, we can deduce the formula of the tunneling current (i_t), where L can be interpreted as the distance between the two electrodes (so we change the notation from L to d):

$$i_t \propto e^{-2\frac{\sqrt{2m}}{\hbar}\sqrt{\phi}d} \tag{2.1.10}$$

where, $2\sqrt{2m}/\hbar = 1.025 \ eV^{1/2}\text{Å}^{-1}$. The exponential characteristics of the tunneling current is first demonstrated in 1928 [Fowler & Nordheim, 1928]. Later, in [Bardeen, 1961], the author formalized the description of the tunneling current using time-based Schrödinger equation which was used for many theoretical studies of tunneling current. Soon after, J. Simmons proposed a formula for tunneling current [Simmons, 1963] based on the difference of potential and the exponential of the distance between the two electrodes separated by vacuum. In continuation of this work, Tersoff and Hamann proposed an expression for the tunneling current [Tersoff & Hamann, 1983] taking into account the geometry of the electrodes used for scanning tunneling microscope. In this manuscript, the exponential behavior of tunneling current proposed in

[Simmons, 1963] is adopted, and this formula is:

$$i_t(t) = g \cdot v_b \cdot e^{-k \cdot d(t)} \tag{2.1.11}$$

where, v_b is a potential difference applied between the two electrodes and d is the distance between them, g is a constant and $k = 2\sqrt{2m}/\hbar = 1.025 \ eV^{1/2}\mathring{A}^{-1}$. In all applications, the tunneling current is generally obtained by approaching a sharp tip to a sample surface. These two are often with a same material in order to obtain a rectangular potential barrier. If the material is not similar, the work function (ϕ) is considered as an average value of the work functions of the two materials.

Finally, in nanopositioning applications, the exponential dependance of tunneling current on the distance (Eq. (2.1.10) and Eq. (2.1.11)) is used. This exponential dependance will be the origin of the main nonlinearity in the control system.

2.2 Applications of the Tunneling Current

2.2.1 Scanning tunneling microscopes

Scanning tunneling microscope (STM) was invented by G. Binnig and H. Rohrer in early 1980s [Binnig et al., 1982] in the IBM laboratories in Zurich and they got nobel prize for this great invention. This device was the first to be able to reconstruct the topography of a sample surface with an atomic scale resolution.

The STM works by scanning a very sharp metal wire tip over a sample surface. A very small voltage is applied between the tip and the sample surface, and then this tip is approached towards the sample surface until the tunneling current appears. In this process, the electrons must tunnel through the vacuum barrier between tunneling tip and sample surface, which represents a potential barrier. The tunnel effect allows an electron to tunnel through this potential barrier even though the electronŠs energy is lower than the barrier height (quantum mechanical phenomenon). The probability of such a process decreases exponentially with the geometrical distance between the tip and the sample surface and with increasing barrier height. The tunneling current appears

when the distance between the tip and sample surface is less than 1×10^{-9} m. After a tunneling current is established, the tip is moved over the surface by a piezoelectric scanning unit (see Fig. 2.2), whose mechanical extension can be controlled by applying appropriate voltages.
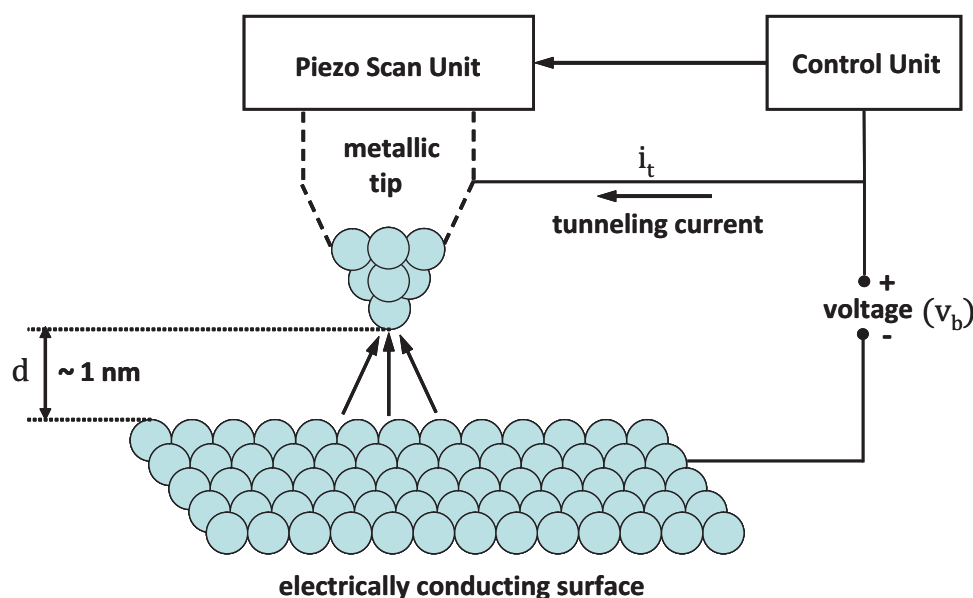
Figure 2.2: Schematic representation of the scanning tunneling microscope.

STM operation modes

The sample topography can be obtained by operating the STM in different modes. There are mainly two modes of operation for STM as shown in Fig. 2.3. The "constant height" mode keeps the position of STM tip constant within the tunneling region while scanning the surface. In this mode, the variation of tunneling current reflects the small atomic corrugation of the surface. However, the tip could be crashed if the surface corrugation is big. To avoid such a problem, generally another approach, called "constant current" mode is mostly used in STM imaging. This mode of operation is safe to use on rough surfaces since the distance between the tip and sample surface is adjusted and the tunneling current is kept constant by a feedback loop of STM.
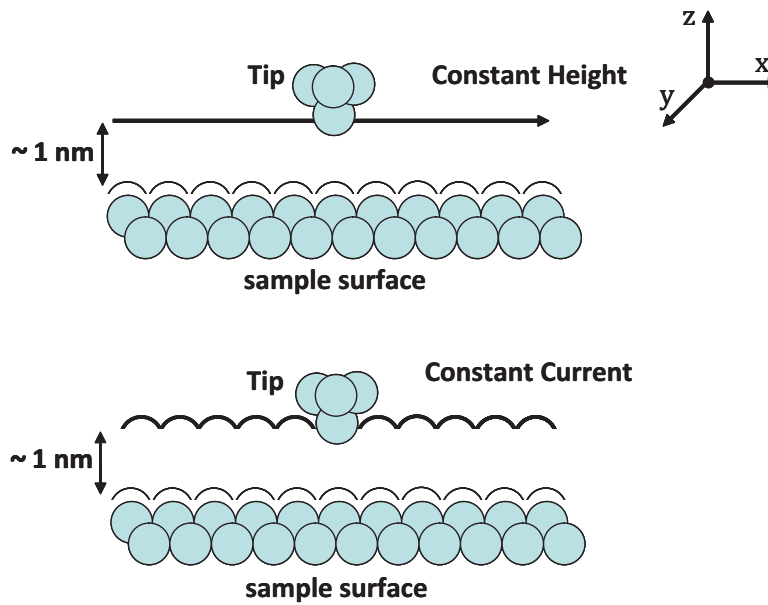
Figure 2.3: "Constant height" and "Constant current" modes of operation.

Vertical control of STM

The vertical feedback loop monitors the tunneling current (i_t) and tries to keep it constant while scanning the sample surface. The current sensor measures the tunneling current which varies because of the distance variation between tip and sample surface while scanning. The control signal regulates the tunneling current by actuating the tip away from or towards the sample surface with the help of piezoelectric actuator. This compensating control signal is directly depends on the variations in the topography and therefore provides a measure of the sample topography. The general feedback loop of STM is presented in Fig. 2.4.

As tunneling current (i_t) is exponentially dependant on the distance (d) between tip and sample surface, a common approach for STM community is to use a logarithmic amplifier after the current sensor in order to deal with exponential nonlinearity in the feedback loop [Oliva et al., 1995], [Anguiano et al., 1996], [Anguiano et al., 1998]. This linearization approach is based on the different approximations that the dynamics of the current sensor, and also the presence of noise between current sensor and the logarithmic amplifier must be neglected. Based on this linearization approach, the linearized output
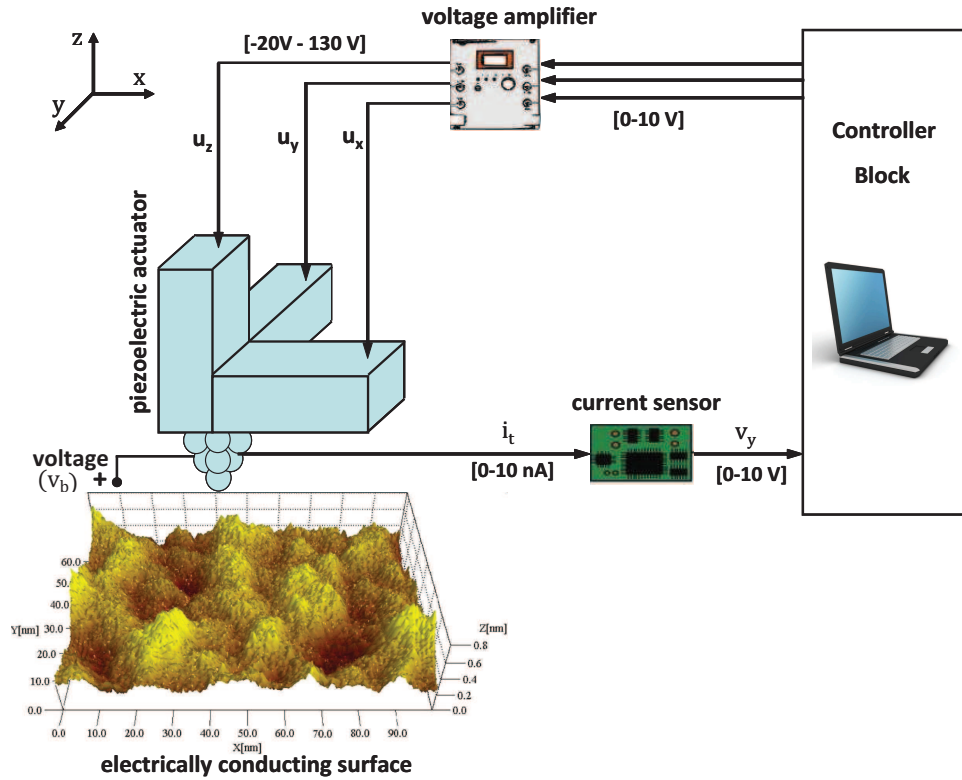
Figure 2.4: Feedback loop for scanning a sample surface (STM).

voltage (v_y) with respect to variations of distance (d) between tip and sample surface is given by:

$$
\begin{aligned}
v_y(t) &= log_{10}(G_{amp} \cdot i_t(t)) \\
&= log_{10}(G_{amp} \cdot g \cdot v_b \cdot e^{-k \cdot d(t)}) \\
&= C_1 - k \cdot log_{10}(e) \cdot d(t)
\end{aligned}
\tag{2.2.1}
$$

where, $C_1 = log_{10}(G_{amp} \cdot g \cdot v_b)$ is a constant term and G_{amp} is the current sensor gain.

From the point of view of controller design for the vertical motion of STM, not much efforts have been done till now. In most commercial equipments of STM, only simple classical proportional-integral (PI) or proportional-integral with derivative (PID) controllers are implemented [Curtis et al., 1997], [Sasaki et al., 1997], [Nakakura et al., 1998], [Bredekamp & Tapson, n.d.], [Bredekamp & Tapson, 1999], where usually the parameters of such controllers are fixed manually by the operator. A feedback loop of STM in vertical z-direction with some stability conditions has been presented in [Oliva et al., 1995], [Anguiano et al., 1996], [Anguiano et al., 1998] and this analysis has been

done with simple classical PI (PID) control technique and with a simplified version of the system model. A step variation in sample surface is studied in [Bonnail, 2001] and a variable structure control (VSC) design methodology in the presence of classical PI control is proposed [Bonnail et al., 2004] in order to avoid the tip collision with the sample surface. Still, there is a need to analyze the vertical system of STM with some modern control techniques in order to get better performances.

Later, the invention of Atomic Force Microscope (AFM) was a new significant step allowing to characterize any sample surface. Because of the related operation challenges, AFMs have also motivated various control studies over the last decade (see for instance [Abramovitch et al., 2007] and references therein). In this context, many efforts have been dedicated to the improvement of scanning performances (horizontal control), while vertical control is mostly concerned with force control, either in contact mode, or in dynamic (oscillatory) mode (see also [Besançon et al., 2007] for a similar operation). Some works have also been dedicated to direct force estimation in such AFMs as in [Besançon et al., 2004], [Besançon et al., 2009]. Because of the atomic resolution, these microscopes have vast applications in different domains of material science [Yamanaka et al., 1999], physics [Tsukada et al., 2000], chemistry [Jandt et al., 2000] and biology [Kassies et al., 2005].

2.2.2 Tunneling accelerometers

The idea of using the tunneling current to measure the accelerations was first presented in [Waltman & Kaiser, 1989]. Because of the high sensitivity of the tunneling current, it is now widely used to measure the accelerations down to sub-micro-g [Kenny et al., 1994], [Rockstad et al., 1996], [Liu et al., 1998], [Liu & Kenny, 2001]. The ability of tunneling accelerometers to detect nano-g magnitude accelerations makes them critical in high precision applications like micro-gravity measurements, acoustic measurements, and seismology.

The operating principle of such accelerometers is based on the position regulation of

a proof mass by the tunneling current. When the mass is subject to an acceleration, the distance between the proof mass and the tunneling tip varies, thereby changing the tunneling current (as tunneling current exponentially depends on the distance). An electrostatic actuator is normally used which is located opposite to the proof mass. A feedback control circuit adjusts the electrostatic re-balance force on the proof mass in order to maintain a constant tunneling current. The external acceleration is measured by recording the feedback deflection voltage.

Control for tunneling accelerometers

For the control of tunneling accelerometers, [Liu et al., 1999] has proposed a controller design via μ synthesis for robust performance with respect to parametric variations of the system model. This approach is successfully implemented by the same researchers [Liu et al., 1998], [Liu & Kenny, 2001] in order to achieve a high resolution of 20 $nano-g/\sqrt{Hz}$ and a 5 Hz-1.5 kHz bandwidth. In [Wang et al., 2002], the author has synthesized a simple control law by using the relation between open loop and closed loop transfer functions for the system of tunneling accelerometer.

Recently, in [Oropeza-Ramos et al., 2008], [Yie et al., n.d.], a complete state space model for the system of tunneling accelerometer has been proposed with a digital integral control design and the effect of different sources of noise (Brownian motion, Nyquist-Johnson and shot noise) are analyzed.

2.3 Piezoelectric Effect

The piezoelectric effect was discovered by Pierre Curie in 1880. The effect is created by squeezing the sides of certain crystals (quartz or barium titanate) and the result is the creation of opposite electrical charges on the sides. The effect can be reversed as well: by applying a voltage across a piezoelectric crystal, it will elongate or compress. These materials are used to scan the tip over the surface in STM and in many other scanning probe techniques. A typical piezoelectric material used in STM is PZT (Lead Zirconium

Titanate). Reference [Katzir, 2006] can be consulted for a detailed understanding of piezoelectric effect.

Piezoelectric scanners are widely used in different scanning-probe microscopes such as in scanning tunneling microscopes (STM), atomic force microscopes (AFM). These piezoelectric scanners are used to move a probe (tip) over a sample surface, both parallel to the sample surface (x and y axes) and perpendicular to the sample surface (z axis). The piezoelectric actuators are now widely used for high positioning accuracy at nanometer and sub-nanometer resolution with high bandwidths [Taylor, 1993], [Ohara & Youcef-Toumi, 1995], [Schitter & Stemmer, 2004]. One of the advantages of using piezoelectric actuators is that under certain experimental conditions their dynamics can be well approximated by linear models [Bhikkaji, Ratnam, Fleming & Moheimani, 2007], leading in general to a second order linear model of the classical form (in the Laplace domain):

$$G_a(s) = \frac{\gamma_0}{\left(\frac{1}{\omega_0^2}\right) s^2 + \left(\frac{1}{Q\omega_0}\right) s + 1} \tag{2.3.1}$$

where γ_0 is sensitivity, ω_0 is the resonance frequency and Q is the quality factor of piezoelectric actuator model.

2.4   Control Issues

2.4.1   Performance compromises

For all nanopositioning applications, the control design has to consider the tradeoffs between precision, bandwidth, robustness and sufficient range of motion. There is always a compromise between these performance parameters [Devasia et al., 2007] as shown in Fig. 2.5.

There is a fundamental tradeoff between the system bandwidth and positioning precision. The positioning precision inversely depends on the bandwidth: systems with larger bandwidth allow noise to affect the precision over a larger frequency range and hence provide poorer positioning precision. Moreover, precision also inversely depends on the
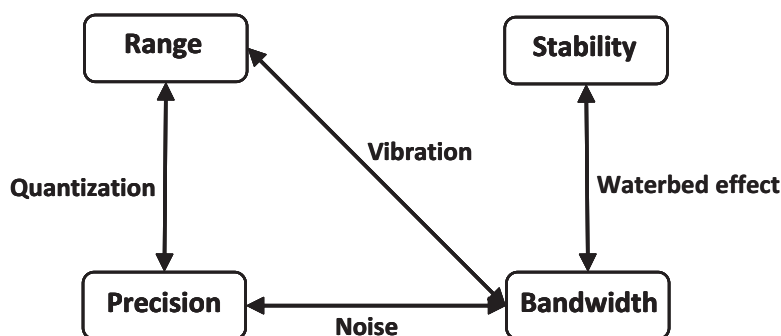
Figure 2.5: Tradeoffs between different parameters.

positioning range because of the nonlinearities and also because of the quantization noise in digital controller implementations. The bandwidth tends to be inversely dependant on the range because the first vibrational resonance of the actuator tends to be higher for a smaller actuator with less range. The vibrations tend to degrade the positioning accuracy as the main frequency content of the input becomes close to the first resonance frequency of the system. Although, vibration-induced error can be reduced by limiting the input frequency content to a level well below the system resonance (low speed operation). Alternatively, to enable higher speed operation, the first resonance frequency of the system can be damped by some control techniques [Ratnam et al., 2005], or it can be increased by optimizing the actuators geometry (to make them stiffer) at the cost of small positioning range. With the proposed control schemes in [Bhikkaji, Ratnam & Moheimani, 2007], [Bhikkaji, Ratnam, Fleming & Moheimani, 2007], the authors were able to achieve a 30 dB damping of the resonant mode without much control efforts. Although, the high speed or large bandwidth and even high precision can also induce robustness and stability issues because of water-bed effect. Because of the nonlinearities, large positioning range can cause instabilities as well.

A lot of studies are currently in progress and much more efforts required working at nanometer scale from control point of view to deal with all such performance compromises. In recent years, a lot of work has been dedicated to the control of piezoelectric actuators for nanopositioning [Salapaka et al., 2002], [Schitter & Stemmer, 2004], [Sebastian & Salapaka, 2005], [Devasia et al., 2007], [Bhikkaji, Ratnam, Fleming & Moheimani, 2007], [Bhikkaji, Ratnam & Moheimani, 2007], [Aphale, Devasia & Mo-

heimani, 2008], [Aphale, Bhikkaji & Moheimani, 2008], but such efforts have not been done till now for the control of piezoelectric actuators for nanopositioning in the presence of tunneling phenomenon (e.g. the vertical control of STM).

2.4.2 Dynamic nonlinearities

Hysteresis: Piezoelectric actuators are widely used in SPM (scanning probe microscopy) [Binnig & Smith, 1986] and many other nano-positioning applications [Gao et al., 2000], [Shim & Gweon, 2001], [Salapaka & Sebastian, 2003]. Such actuators have strong non-linear hysteresis effects which can cause inaccuracy and oscillations in the system response, and could also lead to instability of the closed loop system [Brokate & Sprekels, 1996], [Pare & J.P.How, 1998]. That is why, it is very important to model the hysteresis.
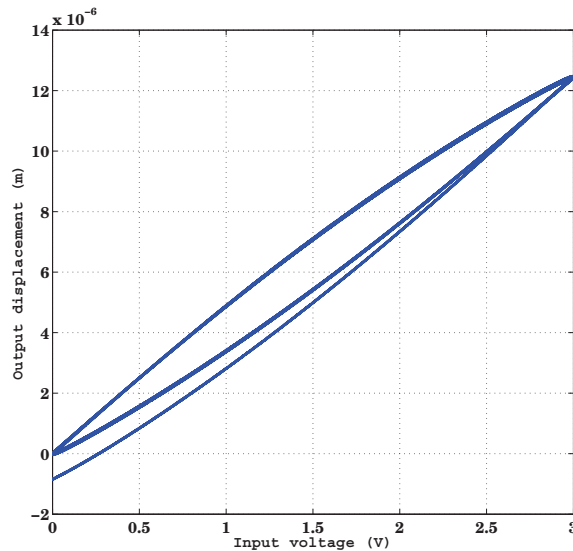
Figure 2.6: Hysteresis loop example for lateral motion of piezoelectric actuator between input voltage of piezoelectric actuator through amplifier and the output displacement sensed by capacitive sensor. This hysteresis loop was observed from experimental platform of Gipsa-lab.

A number of hysteresis models have been developed [Mayergoyz, 2003] in order to facilitate the design of controllers for compensating its effects. Mainly, there are differ-

ential equation based and operator based hysteresis models. Differential equation-based hysteresis models [Visintin, 1994] include Duhem model [Hodgdon, 1988a], [Hodgdon, 1988b], Bouc-Wen model [Sain et al., 1997], Jiles-Atherton model [Jiles & Thoelke, 1989], [Salvini & Fulginei, 2002] etc. Operator based hysteresis models [Macki et al., 1993] include Preisach model [Mayergoyz & Friedman, 1988], Krasnosel'skii-Pokrovskii model [Krasnoskl'skii, 1983], and Prandtl-Ishlinskii model [Brokate & Sprekels, 1996] etc.. The most commonly used operator based hysteresis models are Preisach model and Prandtl-Ishlinskii model. In operator based hysteresis models, the elementary operator is a rate-independent backlash operator. It is commonly used in the modeling of backlash between gears with one degree of freedom. A backlash operator is defined by:

$$\begin{aligned} y(t) &= H_r[x, y_0](t) \\ &= max\{x(t) - r, min\{x(t) + r, y(t - T)\}\} \end{aligned} \qquad (2.4.1)$$

where x is the control input, y is the actuator response, r is the control input threshold value or the magnitude of the backlash, and T is the sampling period. A detailed discussion about hysteresis operator can be found in [Brokate & Sprekels, 1996].

The hysteresis phenomenon in piezoelectric actuators strongly depend on either the maximum value of input voltage being applied, or the frequency of the input signal, or both. Therefore, a dynamic or rate dependent hysteresis modeling is required. Many works related to rate-dependent hysteresis modeling can be found in the literature [Hu & Mrad, 2002], [Janaideh et al., 2008], [Janaideh et al., 2009] and references therein.

Based on the above formulated hysteresis models, two control approaches are commonly adopted in the literature to compensate hysteresis effects. The first approach is to design a controller which directly incorporates the actuator nonlinearities, and the second approach, which is very commonly used, is to construct the inverse of the hysteresis model and apply it as a feedforward compensator as shown in Fig. 5.2. For the first approach, many adaptive control approaches have been recently proposed for hysteresis compensation [Su et al., 2005], [Wang & Su, 2006], [Lin et al., 2006], [Chen et al., 2008], [Liaw et al., 2008]. A lot of research has already been done on the construction of inverse (rate-independent and rate-dependent) hysteresis models and to use them as a feedfor-

ward compensator. Some latest work in this direction is cited here [Song et al., 2005], [Ang et al., 2007], [Al Janaideh et al., 2009], [Iyer & Tan, 2009].
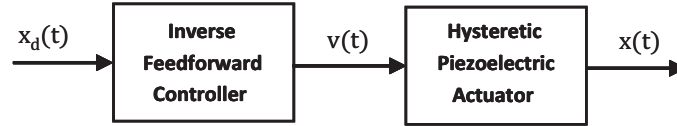
Figure 2.7: Piezoelectric actuator linearization with feedforward inverse hysteresis controller. The input of the feedforward controller $x_d(t)$ is the desired displacement and output $v(t)$ is the voltage to apply to the piezoelectric actuator after amplification.

Recently, it has been shown that the nonlinear hysteresis effects can also be compensated by actuating the piezoelectric actuators using charge amplifiers (rather than voltage amplifiers) [Bhikkaji, Ratnam, Fleming & Moheimani, 2007]. However, in spite of its benefits, the charge actuation has not been generally accepted due to the practical problems of voltage drift, poor low frequency response and also commercially unavailability of the charge sources.

However, the nonlinear hysteresis phenomenon can be neglected for very small displacements (in nanometers) of piezoelectric actuator (e.g. in case of vertical displacement of STM tip where objective is to keep the tunneling current constant, and this tunneling phenomenon occurs when the distance between the tip and sample surface is less than a nanometer) [Oliva et al., 1995], [Bonnail et al., 2000]. In this thesis, hysteresis is neglected in the vertical positioning but it is observed in practice in the lateral positioning.

Creep: Creep can be defined as the drift of the displacement of piezoelectric actuator for a constant applied electric field (see Fig. 2.8). Creep phenomenon has been investigated less frequently compared with hysteresis. Two creep models have been proposed in the literature. The first static nonlinear model [Jung et al., 2000], based on a logarithmic behavior of the creep effect over time, is given by the following equation:

$$x(t) = x_0 \left\{ 1 + \gamma log \left(\frac{t}{t_0} \right) \right\} \tag{2.4.2}$$
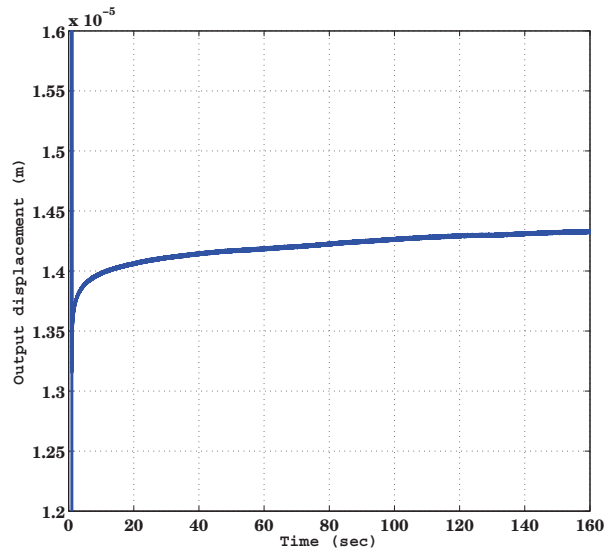
Figure 2.8: Creep phenomenon of piezoelectric actuator observed from experimental platform of Gipsa-lab with a constant input voltage.

where, $x(t)$ is piezoelectric actuator's displacement for any fixed input voltage, t_0 represents the time at which creep effect is apparent, x_0 is the value of actuator displacement at time t_0, and γ is the creep rate. This nonlinear model is difficult to use because of the strong dependance of the creep rate (γ) on the choice of the time parameter t_0. Additionally, this model becomes unbounded for any fixed t_0 as time t becomes large, i.e., $t \to \infty$ or even when $t \to 0$. In order to solve this modeling difficulty, [Croft et al., 2001] has proposed a dynamic linear creep model as a series connection of springs and dampers, i.e.:

$$\frac{X(s)}{V(s)} = \frac{1}{k_0} + \sum_{i=1}^{N} \frac{1}{c_i s + k_i} \tag{2.4.3}$$

where $X(s)$ is the measured response in the lateral direction (in the Laplace domain) and $V(s)$ is the input voltage affecting the lateral movements. k_0 models the elastic behavior at low frequencies, k_i is the spring constant and c_i is the damping constant. It has been shown in [Croft et al., 2001] that the model order N between 3 and 5 can model the creep effect with sufficient accuracy. This low frequency model can be appended to the linear model that describes the vibrational dynamics of the actuator at high frequencies (Eq. (2.3.1)) and thus a controller can be designed for this augmented model to compensate

for creep as well as other vibration effects associated with the actuator.

However, the creep phenomenon has been neglected in this thesis and can be included in future work (perspectives) since it has been observed in experimental results (see Chapter 4 and Chapter 5).

2.4.3 Modeling errors

The system performance should be robust in the presence of modeling errors due to parameter variations and unmodeled dynamics.

Even when the physical parameters of the system are known, they can change over relatively long time intervals because of aging effects (which can occur over short periods of time at nanoscale). Moreover, the parameters are very sensitive to variations in the temperature. Therefore, it is challenging to develop *a priori* accurate models, and experimental modeling and system identification are very important in that respect, but it is also crucial that the control be robust against such possible parameters error. In addition, when designing the controller, the high frequency modes are often neglected to obtain a simplified model. However, these high frequency modes can affect the stability of the closed loop system as well as impose limitations on the achievable performance of the closed loop system [Balas, 1978].

A control system must thus be robust to the differences between the actual system and the model of the system which was used to design the controller. This means beyond *nominal stability* and *nominal performance*, *robust stability* and *robust performance* conditions must also be verified for any considered system.

2.4.4 Coupling effects

Recently, many authors have addressed the cross-coupling problem that arises during high-speed nano-precision positioning using piezoelectric scanners. As mentioned before, these piezoelectric scanners are used to move a probe (tip) over a sample surface, both

parallel to the sample surface (x and y axes) and perpendicular to the sample surface (z axis). The scanning movement of the probe is in a raster (back and forth) pattern. To achieve this specific movement of the probe, a slowly increasing ramp signal is applied to the y-electrode of a piezoelectric scanner while the x-electrode is driven by a fast triangular waveform. All three x, y and z actuation are done by a single piezoelectric tube actuator [Binnig & Smith, 1986]. Normally, the lateral movement of the probe (x and y axes) is controlled by feed-forward compensator in open loop (because of the absence of position sensors in lateral direction) and the vertical movement of the probe (z-axis) is controlled by the feedback compensator.

A complete plant model $P(\omega)$ of such scanning systems can be represented by multi-input multi-output (MIMO) form [Pao et al., 2007], [Butterworth et al., 2009]:

$$P(\omega) = \begin{pmatrix} P_{xx}(\omega) & P_{xy}(\omega) & P_{xz}(\omega) \\ P_{yx}(\omega) & P_{yy}(\omega) & P_{yz}(\omega) \\ P_{zx}(\omega) & P_{zy}(\omega) & P_{zz}(\omega) \end{pmatrix} \tag{2.4.4}$$

where $P_{xx}(\omega)$ represents the transfer function from the x-axis control input to the x-position, $P_{xy}(\omega)$ represents the transfer function from the y-axis control input to the x-position, $P_{xz}(\omega)$ represents the transfer function from the z-axis control input to the x-position, and so forth. Although $P(\omega)$ is a full matrix because of the coupling effects, $P_{xy}(\omega)$, $P_{yx}(\omega)$, $P_{zy}(\omega)$ and $P_{yz}(\omega)$ are generally relatively small compared with the other entries [Song et al., 2005], [Sebastian & Salapaka, 2005], [Butterworth et al., 2009]. The cross-coupling between the x and z-directions, however, can be significant and the scanning movement of the probe (tip) in the lateral x-direction can cause positioning error in the perpendicular z-direction [Song et al., 2005]. This error will become more significant when the sample surface is scanned at high speed or scan frequency becomes close to the piezo scannerŠs vibrational resonance frequency. This is an important limitation in order to perform fast scan speed which is highly required in different nano-fabrication and biological processes [El Feninat et al., 2001].

Few approaches have been used until now in the literature to reduce the dynamics coupling-caused errors, particularly in SPM (scanning probe microscopy) applications

where high positioning precision with fast scan speed is required. [Tien et al., 2004], [Song et al., 2005] have proposed iterative, inversion-based, feedforward control to compensate the dynamics coupling error (from x-axis to z-axis as shown in Fig. 2.9) in piezoelectric scanners during high-speed nano-positioning operations. In this work, the model of the x-to-z coupling dynamics $P_{zx}(\omega)$ and the model of the z-axis dynamics $P_{zz}(\omega)$ are found experimentally (recently, [Maess et al., 2008] tried to find fully coupled piezoelectric scanner dynamics model by finite element (FE) analysis using the commercially available software package ANSYS). According to the authors, the proposed iterative control technique can significantly reduce the dynamics coupling-caused error. For example, at the 13th iteration step of the proposed iterative control technique, the RMS error due to coupling was reduced by 81% (from 10.32 nm to 1.96 nm) and the maximum error was reduced by 86% (from 50.49 nm to 7.23 nm). Later, [Wu et al., 2009],
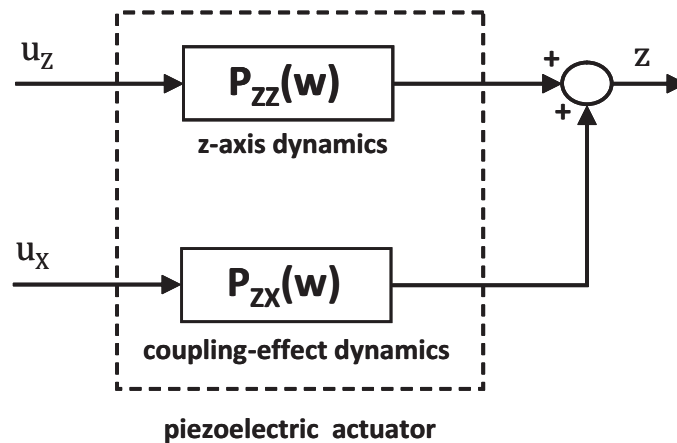
Figure 2.9: The general approach to deal with cross-coupling effect, where vertical deflection z is affected by the z-axis input u_Z and also the x-axis input u_X through coupling-effect dynamics.

[Shi et al., 2009] extended the inversion-based iterative control (IIC) algorithm to further reduce the dynamic coupling caused error and also to achieve better noise attenuation by avoiding potential input saturation during practical implementations. In their work, three external disturbances are considered: unknown sample surface variations, measurement noise and also the disturbance input caused by the x-to-z cross-coupling effect.

[Mahmood & Moheimani, 2009] has highlighted the need of more detailed research

in order to minimize the cross-coupling to the vertical axis of the scanner to achieve higher resolution images at faster scans. [Pao et al., 2007], [Butterworth et al., 2009] have mentioned that the cross-coupling terms have not been explored extensively in the SPM control literature yet and pointed to analyze MIMO controllers for the full plant model (Eq. (2.4.4)) to determine the achievable performance gains.

2.5 Conclusions

In this chapter, the tunneling current phenomenon has been briefly presented and its two main applications (tunneling microscopes and tunneling accelerometers) have been highlighted. Some control related work considered by research community about these applications have been presented. From all this bibliographical work, it has been observed that no much effort has been done till now for the tunneling current measurement system in the the presence of piezoelectric actuator (like vertical control of STM), which requires very precise nanopositioning.

The control issues associated with the problem of nanopositioning have also been presented, including (performance compromises in terms of precision, bandwidth, robustness and range; dynamic nonlinearities; modeling error and coupling effects). Taking into account these issues, the present thesis focuses on the analysis of a specific system of tunneling current with modern robust control techniques and then its validation over an experimental platform developed in Gipsa-lab by control group.

CONTROL PROBLEM AND ROBUST DESIGN

This chapter is devoted to the control system design for very high performance measurement of tunneling current, where ultrahigh positioning accuracy together with high bandwidth are the big challenges. A common approach for such applications is to use conventional proportional integral (PI) control design methodology. In this chapter, modern robust control techniques are analyzed in order to obtain better performances in terms of precision, bandwidth, robustness and disturbance rejection. These control techniques are:

- *Pole placement combined with sensitivity functions shaping*

- *Mixed sensitivity H_∞ control*

The motivation for this work focusing on control for tunneling current measurement systems is presented in Section 3.1.

Section 3.2 very briefly presents a system of tunneling current measurement and a corresponding dynamic modeling is proposed in Section 3.3.

The control problem is formulated with desired measurement performances in Section 3.4 and also the measurement requirements are translated into control requirements.

Section 3.5 and Section 3.6 present the proposed control techniques applied to considered system of tunneling current measurement, also with simulation and comparison results with conventionally used classical PI controller.

Finally, Section 3.7 draws some conclusions.

3.1   Motivation

The phenomenon of *tunneling current* with its applications, is briefly explained in Chapter 2. The control scheme of all tunneling applications is mainly composed of a sensor for the tunneling current measurement and also a regulation feedback loop, having a piezoelectric actuator attached with the tip to move it precisely in appropriate direction.

Tunneling current is the only measurement in vertical z-direction of STM. During scanning, when the separation between the sample surface and the tip decreases or increases due to variations in the sample topography, the control signal regulates the tunneling current by actuating the tip away from or towards the sample surface. This compensating control signal depends on variations in the topography and therefore provides a measure of the sample topography. The quality of the surface image strongly depends on the precision of tunneling current measurement. Since the distance between tip apex and sample surface must be less than 1×10^{-9} m to get the tunneling effect, ultrahigh positioning accuracy together with high bandwidth are here major challenges. As tunneling current is of order of nano-amperes, the presence of different sources of noise [Bordoni & Karim, 1994] (thermal noise, shot noise, $1/f$ noise, quantization noise, etc.) and sample surface variations highly influence the precision of this measurement signal. In addition, non-linearities and physical limitations in the control loop are also limiting factors to be considered in order to get better performances.

As mentioned in the last chapter, not much efforts have been done till now for the vertical control of STM. The most commercial equipments of STM [Curtis et al., 1997], [Sasaki et al., 1997], [Nakakura et al., 1998], [Bredekamp & Tapson, n.d.], [Bredekamp & Tapson, 1999] and also the analysis presented for vertical control of STM in [Oliva et al., 1995], [Anguiano et al., 1996], [Anguiano et al., 1998], are based on classical PI (PID) controllers. Without proper analysis, the imaging process can not be optimum and the image of the surface does not correspond necessarily to the reality [Anguiano et al., 1998]. The quality of the image strongly depends on the precision of tunneling current measurement.

This chapter is devoted to the modern control system design for precise measurement of tunneling current, in the presence of piezoelectric actuator and a sensor for the tunneling current measurement. Desired high performance requirements are transformed into control requirement, which are expressed by means of constraints on the shape of closed-loop sensitivity functions. Then, first a robust control design methodology developed since several years in our laboratory [Landau & Karimi, 1998] based on combined pole placement with sensitivity function shaping and then mixed sensitivity H$_\infty$ control techniques [Skogestad & Postlethwaite, 1996] are proposed and then analyzed for the considered system of tunneling current in order to obtain better performances in terms of precision, robustness and disturbance rejection.

For all numerical values in this chapter, we refer to the characteristics of an experimental platform developed in Gipsa-lab, and fully presented in Chapter 4.

3.2 System Description

The complete closed-loop control scheme which will be here considered is presented in Fig. 3.1. The working principle of the considered system is based on the measurement and control of the tunneling current (i_t) produced between the sharp metallic tip and a biased (v_b) sample surface, when the distance (d) between them is less than 1×10^{-9} m. This tunneling current (i_t) depends exponentially on the distance (d) between tip and sample surface with following non-linear relation as mentioned earlier:

$$i_t(t) = g \cdot v_b \cdot e^{-k \cdot d(t)} \qquad (3.2.1)$$

where g and $k = 1.025\sqrt{\phi}$ (ϕ represents the work function of tip and sample surface) are constants. Controlling this tunnel current (i_t) by keeping the distance (d) constant in the presence of external disturbances (noise (n), sample surface variations (z_S) etc.) is the main objective of the considered feedback control system just like an STM in vertical z-direction.

The first step is to bring the tip close to the sample surface (without any contact or collision between them) until the tunneling current (i_t) is obtained. The complete
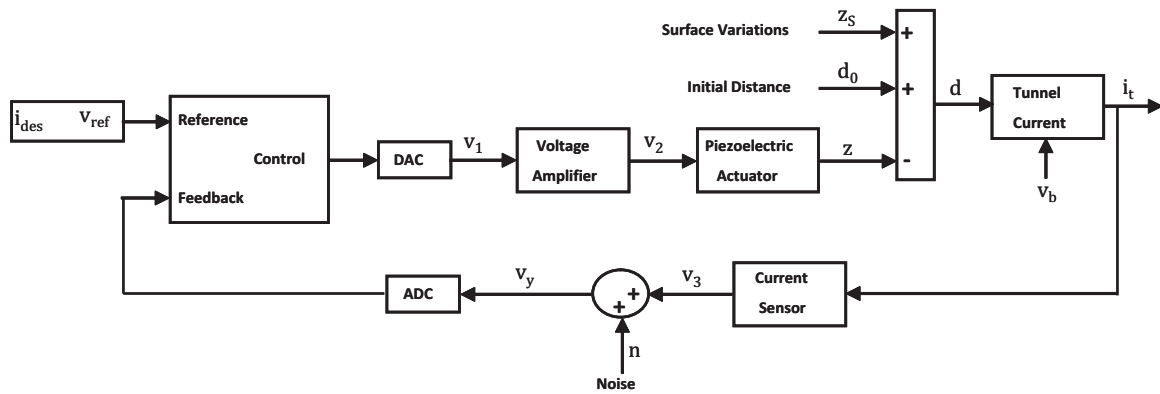
Figure 3.1: Complete simulation model with block diagram representation.

procedure for tip approach mechanism is the part of next chapter. A feedback loop constantly monitors the tunneling current (i_t). The tunneling current sensor is a current to voltage convertor (CVC) with high gain which converts the small tunneling current into a voltage (v_3). This voltage is subject to measurement noise (n) resulting into the available voltage for feedback (v_y). On the other hand, a piezoelectric actuator is attached with the tip to move it in appropriate direction according to the applied voltage (v_2) in order to keep the distance (d) or in other words the tunneling current (i_t) constant at its desired value (i_{des}). The nonlinear hysteresis phenomenon is expected to be negligible here for the piezoelectric actuator since the displacement is very small, less than a nanomemter for the vertical movement (z-direction) [Bonnail et al., 2000], [Oliva et al., 1995]. A voltage amplifier is used before piezoelectric actuator at the output of controller. Knowing the gain of piezoelectric actuator, its position effect (z) defines the distance $(d(t) = d_0 + z_S(t) - z(t))$ between tip and sample surface, where d_0 is the initial distance between tip and sample surface when tunneling current (i_t) appears and z_S the sample surface variations, considered here as an external unknown disturbance. One assumption is taken here which is commonly used in the literature [Chen, 2008] that the tunneling current (i_t) appears from a distance (d) between tip and sample surface equal to one nanometer. Based on this assumption, it can be written:

$$
\begin{aligned}
i_t(t) &= g \cdot v_b \cdot e^{-k \cdot d(t)} \quad if \ \ 0 < d(t) \le 1 \ nm \\
i_t(t) &= 0 \quad if \ \ d(t) > 1 \ nm
\end{aligned}
\tag{3.2.2}
$$

3.3   System Modeling

The purpose of this section is to model the considered system of tunneling current. The open loop system is shown in Fig. 3.2 where the overall system consists of:

- the voltage amplifier;

- the vertical z-piezoelectric actuator;

- the physical law which gives the relationship between tunneling current and the distance between tip and sample surface;

- the current sensor (CVC).
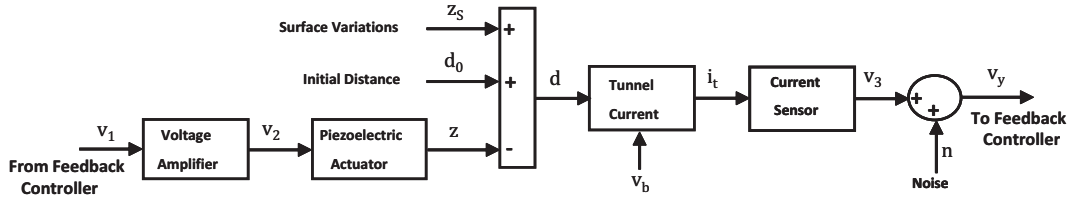
Figure 3.2: Open loop system with block diagram representation.

3.3.1   Global nonlinear system model

Each subsystem (as shown in Fig. 3.2) is modeled separately in order to obtain the overall global nonlinear system model.

The **voltage amplifier** used before piezoelectric actuator, has been modeled by a linear first order dynamics:

$$
\begin{aligned}
\dot{x}_1(t) &= -\omega_v \cdot x_1(t) + v_1(t) \\
v_2(t) &= G_v \omega_v \cdot x_1(t)
\end{aligned}
\tag{3.3.1}
$$

where v_1 and v_2 are input and output of the voltage amplifier respectively, ω_v is the bandwidth and G_v the gain of the voltage amplifier.

The ***piezoelectric actuator*** attached to the tip to move it in vertical z-direction, has been modeled by a linear second order dynamics. The displacement of this piezoelectric actuator in vertical z-direction is less than one nanomemter (in order to remain within tunneling current region) so the hysteresis of the actuator can be neglected [Bonnail et al., 2000], [Oliva et al., 1995] and the dynamics can be well approximated by linear model [Bhikkaji, Ratnam, Fleming & Moheimani, 2007]. The considered second order dynamics is:

$$
\begin{aligned}
\dot{x}_2(t) &= -2\zeta\omega_a \cdot x_2(t) - \omega_a^2 \cdot x_3(t) + v_2(t) \\
\dot{x}_3(t) &= x_2(t) \\
z(t) &= G_a\omega_a^2 \cdot x_3(t)
\end{aligned}
\tag{3.3.2}
$$

where v_2 and z are input and output of the piezoelectric actuator respectively, ζ is the damping, ω_a the bandwidth and G_a the gain of the piezoelectric actuator.

The ***physical law*** between tunneling current (i_t) and distance (d) has been modeled by an expression as given in equation (3.2.2). This physical law introduces the exponential static nonlinearity in the model of the system.

The ***current sensor*** (CVC) to measure and convert the small tunneling current (i_t) into a voltage, has been modeled by a linear first order dynamics:

$$
\begin{aligned}
\dot{x}_4(t) &= -\omega_c \cdot x_4(t) + i_t(t) \\
v_3(t) &= G_c\omega_c \cdot x_4(t)
\end{aligned}
\tag{3.3.3}
$$

where i_t and v_3 are input and output of the current sensor (CVC) respectively, ω_c is the bandwidth and G_c the gain of the current sensor (CVC).

To summarize, the overall global nonlinear system (order 4) is given by:

$$
\begin{cases}
\dot{x}_1(t) &= -\omega_v \cdot x_1(t) + v_1(t) \\
\dot{x}_2(t) &= G_v\omega_v \cdot x_1(t) - 2\zeta\omega_a \cdot x_2(t) - \omega_a^2 \cdot x_3(t) \\
\dot{x}_3(t) &= x_2(t) \\
\dot{x}_4(t) &= -\omega_c \cdot x_4(t) + gv_b \cdot e^{-k(d_0 + z_S(t) - G_a\omega_a^2 \cdot x_3(t))} \\
v_y(t) &= G_c\omega_c \cdot x_4(t) + n(t)
\end{cases}
\tag{3.3.4}
$$

For the purpose of a linear control design, this global nonlinear model Eq. (3.3.4) will be here transformed into an appropriate linear system.

3.3.2   Linearization

To deal with exponential static nonlinearity given by the physical law between tunneling current (i_t) and distance (d) between tip and sample surface (Fig. 3.3), two different approaches for linearization are discussed here.
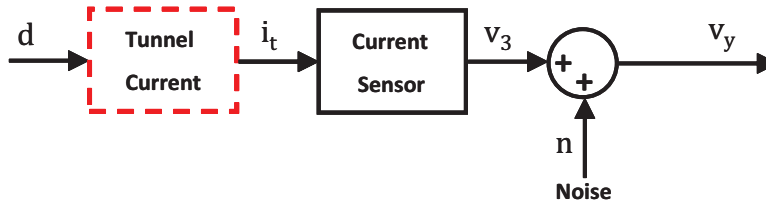
Figure 3.3: Block diagram representation of tunneling current and current sensor (dashed block indicates the nonlinear element).

Electronic linearization

A common approach for linearization by physicists in this specific situation is to use a logarithmic amplifier after current sensor (CVC) in order to deal with static exponential nonlinearity [Oliva et al., 1995], [Anguiano et al., 1996], [Anguiano et al., 1998]. This linearization approach is based on the following two assumptions:

- Neglecting dynamics of the current sensor (CVC), considered as constant;

- Neglecting presence of noise (n) between exponential and logarithmic nonlinearity.

This linearization approach is represented in Fig. 3.4 resulting into the available voltage for feedback (v_y) is:

$$\begin{aligned} v_y(t) &= log_{10}(v_3(t)) \\ &= log_{10}(G_c \cdot i_t(t)) \\ &= log_{10}(G_c \cdot g \cdot v_b \cdot e^{-k \cdot d(t)}) \\ &= log_{10}(G_c \cdot g \cdot v_b) - k \cdot log_{10}(e) \cdot d(t) \end{aligned} \quad (3.3.5)$$

The output voltage (v_y) is linear with respect to the distance (d) between tip and sample surface. This approach has the advantage of working on a wide range of tunneling current (i_t).
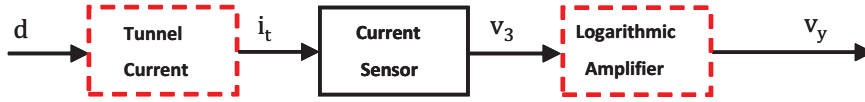
Figure 3.4: Physicists linearization approach with logarithmic amplifier.

Approximate linearization around an operating point

An alternative approach, which will be considered here, is to approximate the nonlinear dynamics around an operating point by a first order Taylor expansion. This allows to account for the current sensor dynamics (CVC) as well as the presence of noise (n) and the model will be valid as long as current variations remain small enough. In this approach, the linearized equation corresponding to the nonlinear equation (3.2.1) is given by:

$$d(t) = \left(-\frac{1}{k} log(\frac{i_{eq}}{g \cdot v_b}) \right) + \left(-\frac{1}{k \cdot i_{eq}} \right) \times (i_t(t) - i_{eq}) \tag{3.3.6}$$

where i_{eq} is the operating tunneling current. (Notice that a similar analysis could be done with the logarithmic amplifier taking into account CVC dynamics and the presence of noise).

3.3.3 Linear control design model

After linearization, the overall global linear system (order 4) between v_1 and v_y is modeled as:

$$
\begin{cases}
\dot{x}_1(t) & = -\omega_v \cdot x_1(t) + v_1(t) \\
\dot{x}_2(t) & = G_v\omega_v \cdot x_1(t) - 2\zeta\omega_a \cdot x_2(t) - \omega_a^2 \cdot x_3(t) \\
\dot{x}_3(t) & = x_2(t) \\
\dot{x}_4(t) & = -c_1 G_a \omega_a^2 \cdot x_3(t) - \omega_c \cdot x_4(t) + c_1 \cdot z_S(t) + i_{eq} \\
v_y(t) & = G_c\omega_c \cdot x_4(t) + n(t)
\end{cases}
\tag{3.3.7}
$$

where, $c_1 = -k \cdot i_{eq}$ is a constant.

A linear control design model is required for the linear controller synthesis. For this purpose, the complete simulation model (Fig. 3.1) is transformed into an appropriate feedback control design model (Fig. 3.5) with linear time invariant transfer functions,
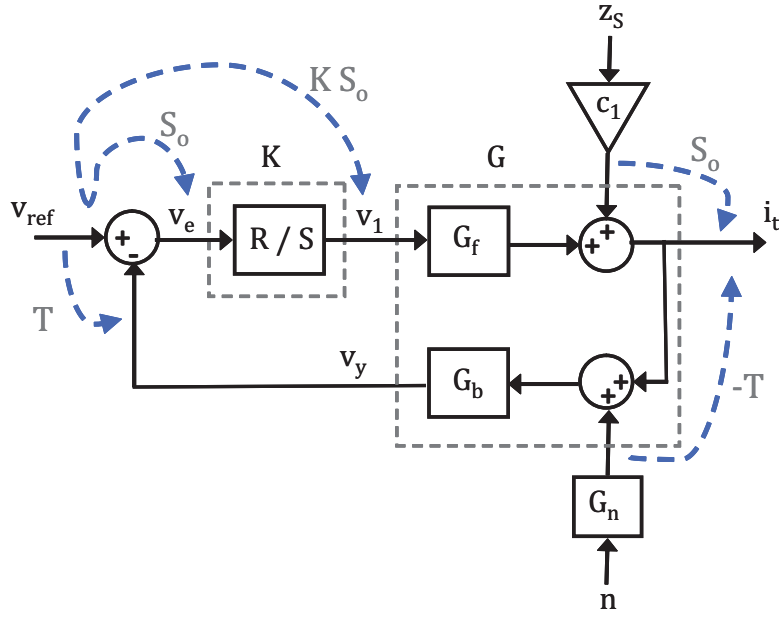
Figure 3.5: Control design model $\mathbf{G}$ and feedback loop.

where $\mathbf{K}$ represents the controller, $\mathbf{G_f}$ represents the 3rd order feedforward linear dynamics with voltage amplifier, vertical z-piezoelectric actuator and the physical law between tunneling current (i_t) and distance (d), and $\mathbf{G_b}$ represents the 1st order feedback linear dynamics of current sensor (CVC). In Fig. 3.5, G_n is the noise transfer which is the inverse of feedback linear dynamics (G_b). The continuous time transfer function of the system is $\mathbf{G}(s) = \mathbf{G_f}(s).\mathbf{G_b}(s)$ and the open-loop transfer function of the overall system in the presence of controller is $\mathbf{H_{OL}}(s) = \mathbf{G}(s).\mathbf{K}(s)$. The controlled output is tunneling current (i_t) and the external inputs are: the reference voltage (v_{ref}) representing the desired tunneling current (i_{des}), the unknown sample surface variations (z_S) and the noise (n). There are different sources of noise (n) in the considered system of tunneling current which are elaborated in coming section and has taken into account during simulations aiming at representing a real system as much as possible.

3.3.4 Noise considerations

For the system of tunneling current, one of the external disturbances considered here is the noise (n). It is important to list, characterize and then quantify the different types of noises effecting the tunneling current (i_t) and the performance in terms of precision of

the whole system at the nanoscale. Each noise is quantified by the theoretical description of its power spectral density so that it can be integrated in the simulation.

Thermal noise

The considered system works at ambient temperature. The tunneling current (i_t) fluctuates because of the thermal noise, generated by the thermal agitation of the electrons crossing the potential barrier between the electrodes (tip and sample surface). The concept of thermal noise has been first experimentally demonstrated by Johnson [Johnson, 1928] and mathematically calculated by Nyquist [Nyquist, 1928]. Thermal noise is approximately a white noise and its power spectral density (S_{th}) is given by:

$$S_{th} = \frac{4k_B T}{R_t} \quad [A^2/Hz] \tag{3.3.8}$$

where, k_B is Boltzmann's constant in joules per kelvin, T is the absolute temperature in kelvins and R_t is the tunneling resistance in Ohms, which is the resistance across the two electrodes (tip and sample surface). For a typical resistance of 10^8 Ω of the tunneling current, the power spectral density of this thermal noise at $20°C$ is approximately $S_{th} = 1.6 \times 10^{-28}$ A^2/Hz. This fluctuation in tunneling current (i_t) can be observed in the measured signal at the output of the considered system, indicated as (n) in Fig. 3.2.

1/f noise

This noise is common in most electronic devices, its power spectral density ($S(f)$) is inversely proportional to the frequency (f): $S(f) \propto 1/f^\alpha$, with α generally between 0.8 and 1.4. The first spectral density measurement of a $1/f$ noise was published by Johnson [Johnson, 1925], although the origin of this noise is still unclear. In the case of tunneling current (i_t), different ideas about the origin and the influences of this $1/f$ noise are discussed in [Lagoute, 2003], [Sugita et al., 1996]. This noise is dominant at low frequencies. Beyond a certain frequency, it becomes negligible compared to the thermal noise. The noise intensity at a fixed tunneling current increases with increasing bias voltage between tip and sample surface. [Hooge, 1969] has demonstrated a relationship

for the spectral density of the fluctuations of the current measurements in homogeneous metallic samples with average current of I_o.

$$S(f) = \frac{cI_o{}^2}{f^\alpha} \quad [A^2/Hz] \tag{3.3.9}$$

where c is a constant term. Depending on the nature of the tip and the sample surface and also the environmental conditions, the average power spectral density $S(f)$ of this $1/f$ noise is around 10^{-24} A^2/Hz. This noise is also at the output of the considered system, indicated as (n) in Fig. 3.2.

Shot noise

Shot noise can also be one of the reasons of random fluctuations of the tunneling current, as the current being carried by discrete charges (electrons) between the electrodes (tip and sample surface), whose number per unit time fluctuates. Shot noise is often only a problem with small currents of few nano amperes and its theoretical concept was first described by Schottky [Schottky, 1926]. Shot noise has a Poisson distribution and has white noise properties (flat power spectral density). The power spectral density (S_{sh}) of this noise for an average tunneling current (I_t) is given by:

$$S_{sh} = 2eI_t \quad [A^2/Hz] \tag{3.3.10}$$

where, e is the electron charge in Coulombs. For an average tunneling current of 1 nA, the power spectral density of this shot noise is approximately $S_{sh} = 3.2 \times 10^{-28}$ A^2/Hz, which is also considered at the output of the considered system, indicated as (n) in Fig. 3.2.

Environmental vibrations

Environmental vibrations can not be neglected while working at nanometer scale. There can be different sources of such vibrations which induce the distortion into the measurement. The vibrations induced by the building structure have a very low resonance frequency, typically between 10 Hz and 30 Hz with an amplitude of several nanometers. The human activity in the working place proximity is the origin of the mechanical

vibrations. These mechanical vibrations are significant only at low frequencies and the use of anti-vibration table for experimental setup can be one possible solution to minimize these vibrations. The acoustic waves in the environment (because of running air conditioning, computer fans, moving and speaking people) induce distortion too, which can be minimized by using proper acoustic shielding.

The effect of all these noises mentioned above are included in the simulation for the validation of the proposed controllers.

3.3.5 Uncertainty model

Usually, a control system is considered to be robust if it is insensitive to differences between the actual system and the model which has been used to design the controller. These differences are referred to as *model uncertainties.*

To account for model uncertainty, it can be assumed that the dynamic behavior of the plant is described not by a single linear time invariant model $G(s)$, but by a set Π of possible linear time invariant models $G_\Delta(s) \in \Pi$, denoted as "uncertainty set". From the nominal plant model $G_0(s)$, the set Π of possible linear time invariant models $G_\Delta(s)$ can be built by varying the model parameters inside a given range of values. For the considered system of tunneling current, we have considered the variations in the following parameters of the system model:

- the gain of the piezoelectric actuator (G_a), being the most sensitive element of the closed-loop;

- the bandwidth of the voltage amplifier (ω_v) which is of the order of desired closed-loop bandwidth. All the other elements in the loop have very high bandwidths;

- the constant term (k) of physical tunneling current phenomenon.

The nominal values together with their percentage variations are shown in Table 3.1.

The parametric uncertainty is usually represented by complex perturbations. The

Table 3.1: System parameters together with their values and percentage variations

Parameter description	Value	% variation
Sensitivity of piezoelectric actuator (G_a)	1.2 ± 0.12 [nm]	10 %
Bandwidth of voltage amplifier (ω_v)	4000 ± 400 [Hz]	10 %
Constant term for tunneling phenomenon (k)	2.29 ± 0.229 [1/Å]	10 %
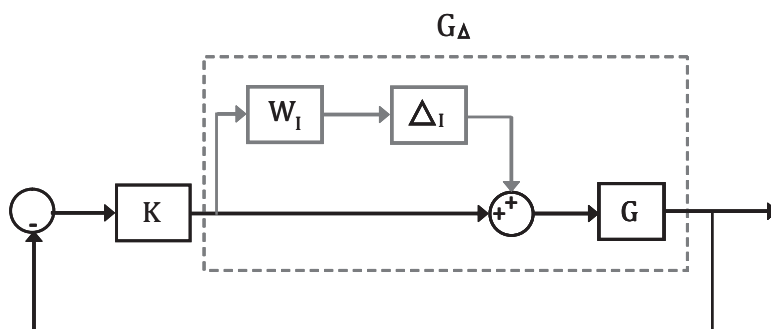
Figure 3.6: Feedback system with multiplicative uncertainty.
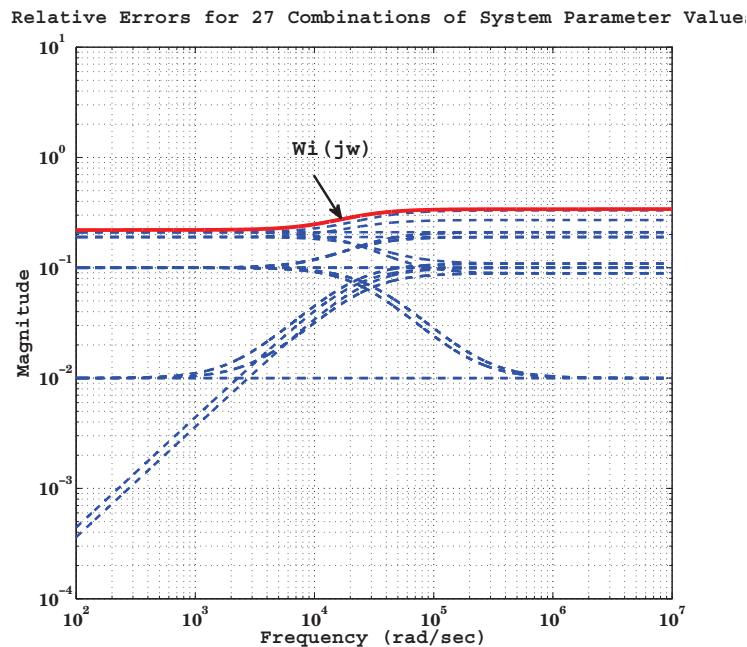
Figure 3.7: Relative plant errors $l_I(j\omega)$ (dashed lines) and rational weight $W_I(j\omega)$ (solid line) for 27 possible combinations of the system parameters.

uncertainty regions around a nominal plant $G_0(s)$ can be generated by these additive or multiplicative complex norm bounded perturbations (additive or multiplicative uncertainty) [Skogestad & Postlethwaite, 1996]. We have chosen a multiplicative uncertainty model for the considered system of tunneling current as generally the numerical value of multiplicative weights is more informative in order to attain the conditions for robust stability and robust performance (see coming section). The multiplicative uncertainty model $G_\Delta(s)$ can be described by the following equation (Fig. 3.6):

$$G_\Delta(s) = G_0(s)(1 + W_I(s)\Delta_I(s)) \tag{3.3.11}$$

where $|\Delta_I(j\omega)| \leq 1, \forall\omega$. Here, $\Delta_I(s)$ is any stable transfer function which at each frequency is less than one in magnitude, representing the normalized complex perturbations and $W_I(s)$ is the uncertainty weight. In case of multiplicative uncertainty model, the relative error function can be computed as:

$$l_I(\omega) = \max_{G_\Delta \in \Pi} \left| \frac{G_\Delta(j\omega) - G_0(j\omega)}{G_0(j\omega)} \right| \tag{3.3.12}$$

and the rational weight $W_I(j\omega)$ is chosen as follows:

$$| W_I(j\omega) | \geq l_I(\omega), \quad \forall\omega \tag{3.3.13}$$

Relative errors $l_I(j\omega)$ together with the rational weight $W_I(j\omega)$ are plotted in Fig. 3.7. The uncertainty weight $W_I(s)$ is chosen as a transfer function that satisfies condition (3.3.13):

$$W_I(s) = \frac{(1/\omega_B)s + A}{(1/(\omega_B M))s + 1} \tag{3.3.14}$$

where, $\omega_B = 6 \times 10^4 \ rad/sec$, $A = 0.22$ and $M = 0.34$.

3.4   Control Problem Formulation with Desired Performances

In this section, all desired performances for the considered system of tunneling current are translated into control requirements. These control requirements are expressed in terms of constraints on the closed-loop sensitivity functions which will be used for controller

synthesis and for performance analysis of the considered closed-loop system of tunneling current.

Closed loop sensitivity functions

The closed-loop system mostly operates under the influence of different types of disturbances and it is very important to analyze the effect of them on the input and output of the system. The effect of these disturbances can be obtained by analyzing the so-called *closed loop sensitivity functions*. These sensitivity functions play an important role in the performance and robustness analysis of the closed-loop system.

For the considered closed-loop system of tunneling current (Fig. 3.5), two types of external disturbances are considered: sample surface variations (z_S) and noise (n). The other input signal of closed-loop system is the reference voltage (v_{ref}) which represents the desired tunneling current (i_{des}). The influence of all these three external inputs (v_{ref}, z_S, n) over the control signal (v_1) and the controlled output (i_t) can be expressed by following relations:

$$\mathbf{V_1}(s) = \frac{1}{1 + G(s)K(s)}[K(s)\mathbf{V_{ref}}(s) - c_1 G_b(s)K(s)\mathbf{Z_S}(s) - K(s)\mathbf{N}(s)] \qquad (3.4.1)$$

$$\mathbf{I_t}(s) = \frac{1}{1 + G(s)K(s)}[K(s)G_f(s)\mathbf{V_{ref}}(s) + c_1\mathbf{Z_S}(s) - G_f(s)K(s)\mathbf{N}(s)] \qquad (3.4.2)$$

where, $G(s) = G_f(s)G_b(s)$ and $c_1 = -k \cdot i_{eq}$ is a constant.

These relations will help to define the control problem and the desired performances in terms of constraints over the closed loop sensitivity functions. The closed loop sensitivity functions are generally defined as:

$$\mathbf{S_o}(s) = \frac{1}{1 + G(s)K(s)}; \quad Output\ sensitivity\ function \qquad (3.4.3)$$

$$\mathbf{KS_o}(s) = \frac{K(s)}{1 + G(s)K(s)}; \quad Input\ sensitivity\ function \qquad (3.4.4)$$

$$\mathbf{T}(s) = \frac{G(s)K(s)}{1 + G(s)K(s)}; \quad Complementary\ sensitivity\ function \qquad (3.4.5)$$

From equations Eq. (3.4.3) and Eq. (3.4.5), it is obvious that:

$$S_o(s) + T(s) = 1 \qquad (3.4.6)$$

Before the controller synthesis, first it is needed to define the control problem and also the desired performances for the considered system of tunneling current.

3.4.1 Control problem formulation

For the feedback control system of Fig. 3.5, the control problem can be formulated as a disturbance rejection problem: variations in the sample surface (z_S) as well as measurement noise (n) are indeed considered as external disturbances, where the first one can be considered as a slowly varying disturbance and the latter one can be considered as a fastly varying disturbance. These disturbances must be rejected by moving the tip in appropriate direction with the help of piezoelectric actuator so that the tunneling current (i_t) should always remain constant at its desired value. In addition, as usual in control design, the control variable itself must not be too much affected by noises, and this is even more important for STM applications (since the control is also used for imaging purposes). So, the associated sensitivity functions must be shaped in order to obtain the best rejection of these disturbances.

The control objectives for the considered system of tunneling current are:

- Good robustness and stability margins;

- High measurement (or equivalently current control) accuracy;

- Noise attenuation at system input (STM application).

- Large closed-loop bandwidth;

All those control objectives will be tackled altogether by the proposed design approaches which are described in coming sections.

3.4.2 Desired performance constraints

All desired performance requirements can be expressed by means of constraints on the shape of closed-loop sensitivity functions [Landau & Zito, 2006]. All these constraints are discussed here.

Robustness and stability constraints

The stability of the closed-loop system requires that all the sensitivity functions be asymptotically stable. The *modulus margin* and *delay margin* are generally considered as robustness margins.

Modulus margin: ΔM is defined as the radius of the circle centered in $(-1, j0)$ and tangent to the Nyquist plot of $H_{OL}(j\omega)$. From the definition of the vector connecting the critical point $(-1, j0)$ with the Nyquist plot of $H_{OL}(j\omega)$:

$$\Delta M = |1 + H_{OL}(j\omega)|_{min} = (\|S_o\|_\infty)^{-1} \qquad (3.4.7)$$

In other words, the reduction (or minimization) of $\|S_o\|_\infty$ will imply the increase (or maximization) of the modulus margin ΔM. Typical values for good modulus margin are $\Delta M \geq 0.5$ ($-6\ dB$). A good modulus margin guarantees satisfactory values for the stability margins e.g. $\Delta M \geq 0.5$ implies a gain margin $\Delta G \geq 2$ ($6\ dB$) and a phase margin $\Delta\phi > 29\,°$.

Delay margin: $\Delta\tau$ is defined as the maximum admissible increase of the delay of the open-loop system without making the closed-loop system unstable.

$$\Delta\tau = \frac{\Delta\phi}{\omega_{cr}} \qquad (3.4.8)$$

where $\Delta\phi$ is the phase margin and ω_{cr} is the crossover frequency where the Nyquist plot of $H_{OL}(j\omega)$ crosses the unit circle centered at origin. The typical value for the delay margin is $\Delta\tau \geq T_S$ where T_S is the sampling time.

For sufficient stability margins, the maximum of output sensitivity function ($\mathbf{S_o}$) should be less than $6\ dB$ which will ensure good robustness margin as well. It can be

denoted as **Constraint 1** for the synthesis of the controller.

$$\|\mathbf{S_o}\|_\infty \leq 6 \; dB, \quad \forall \omega \tag{3.4.9}$$

In the same way, the maximum of complementary sensitivity function (**T**) should be less than 3.5 dB, expressed as **Constraint 2** for the shape of closed-loop sensitivity function.

$$\|\mathbf{T}\|_\infty \leq 3.5 \; dB, \quad \forall \omega \tag{3.4.10}$$

To avoid instability due to saturation effects in the electronic part, the maximum of input sensitivity function (KS_o) should be less than 20 dB which is expressed as **Constraint 3** for the closed-loop sensitivity function.

$$\|\mathbf{KS_o}\|_\infty \leq 20 \; dB, \quad \forall \omega \tag{3.4.11}$$

Robust stability and robust performance constraints

In addition to nominal stability and performance, the objectives of a robust control system include:

Robust Stability (RS): The system is stable for all perturbed plants around the nominal model up to the worst-case model uncertainty.

Robust Performance (RP): The system satisfies the nominal stability (NS) and the nominal performance (NP) conditions. It also guarantees that performance specifications are meet for all perturbed plants up to the worst-case model uncertainty.

In the presence of multiplicative uncertainty (Section 3.3.5), the condition for Robust Stability (RS) according to Nyquist stability condition is given by [Skogestad & Postlethwaite, 1996]:

$$
\begin{aligned}
RS \quad &\Longleftrightarrow \quad |W_I H_{OL}| \; < \; |1 + H_{OL}|, \quad \forall \omega \\
&\Longleftrightarrow \quad \left|\frac{W_I H_{OL}}{1 + H_{OL}}\right| \; < \; 1, \quad \forall \omega \\
&\Longleftrightarrow \quad |W_I T| \; < \; 1, \quad \forall \omega
\end{aligned}
$$

$$\Longleftrightarrow \quad \|W_I T\|_\infty \quad < \quad 1$$

where W_I is the uncertainty weighting function. Thus, the requirement of robust stability (RS) for the case with multiplicative uncertainty gives an upper bound on the complementary sensitivity function (T). This upper bound is expressed as **Constraint 4** for the closed loop sensitivity function:

$$RS \quad \Longleftrightarrow \quad |\mathbf{T}| \quad < \quad \frac{1}{|W_I|}, \quad \forall\omega \tag{3.4.12}$$

Before giving the condition for Robust Performance (RP), the condition for Nominal Performance (NP) is:

$$|W_P S_o| \quad < \quad 1, \quad \forall\omega \tag{3.4.13}$$

where W_P is the designed performance weighting filter and $1/|W_P(s)|$ will impose the upper bound on the magnitude of output sensitivity function (S_o). The performance weighting filter is chosen as:

$$W_P(s) = \frac{(1/M_s)\, s + \omega_s}{s + \omega_s \cdot \epsilon_s} \tag{3.4.14}$$

The details about all performance weighting filters are discussed later in Section 3.6. Now, for Robust Performance (RP), we require the performance condition to be satisfied for all possible plants, that is, including the worst case uncertainty. The condition for Robust Performance (RP) is obtained as [Skogestad & Postlethwaite, 1996]:

$$
\begin{aligned}
RP \quad &\Longleftrightarrow \quad |W_P| + |W_I H_{OL}| \quad < \quad |1 + H_{OL}|, \quad \forall\omega \\
&\Longleftrightarrow \quad \left|\frac{W_P}{1 + H_{OL}}\right| + \left|\frac{W_I H_{OL}}{1 + H_{OL}}\right| \quad < \quad 1, \quad \forall\omega \\
&\Longleftrightarrow \quad |W_P S_o| + |W_I T| \quad < \quad 1, \quad \forall\omega
\end{aligned}
$$

So, the RP constraint is expressed as **Constraint 5** for the closed loop sensitivity functions:

$$RP \Longleftrightarrow \max_\omega(|\, \mathbf{W_P S_o}\,| + |\, \mathbf{W_I T}\,|) \quad < \quad 1, \quad \forall\omega \tag{3.4.15}$$

Measurement accuracy constraints

The desired performance requirement is to keep the tunneling current (i_t) constant at desired value in the presence of all external disturbances. For measurement accuracy, a maximum of $\pm 10\%$ variations is allowed in the tunneling current (i_t). This performance criteria will define the maximum allowed error voltage (v_e), or the lower limit (-20 dB) for output sensitivity function (S_o) in the measurement bandwidth (ω_M), where ω_M defines the maximum allowed variations 800 rad/sec (127.32 Hz) of sample surface (z_S) with an amplitude of 0.5 Å. To limit the influence of surface variations (z_S) on the controlled output (i_t) in order to achieve the desired measurement accuracy, the transfer function between sample surface (z_S) and controlled output (i_t) is considered which is given by $c_1 \cdot S_o$ as shown in Fig. 3.5, where c_1 is a known constant. According to the desired accuracy in measurement bandwidth, this constraint (**Constraint 6**) can be formulated as:

$$
\begin{aligned}
|c_1 \cdot S_o|_{dB} &\leq -20 \ dB, \quad 0 \leq \omega \leq \omega_M \\
\Rightarrow |S_o|_{dB} &\leq -27.2 \ dB, \quad 0 \leq \omega \leq \omega_M
\end{aligned}
\tag{3.4.16}
$$

In addition, the transfer function between noise (n) and controlled output (i_t) has to be considered and it is given by $-G_n T$ (see Fig. 3.5), where G_n is a known transfer function. According to the desired performance in terms of measurement accuracy, this constraint (**Constraint 7**) can be written:

$$
\begin{aligned}
|G_n T|_{dB} &< 0 \ dB, \quad \omega > \omega_M \\
\Rightarrow |T| &< \left| \frac{1}{G_n} \right|, \quad \omega > \omega_M
\end{aligned}
\tag{3.4.17}
$$

Surface variations reconstruction constraint

In order to limit the influence of noise (n) on the system input (v_1), the transfer function between them (KS_o) should respect the following relation, expressed as **Constraint 8** for the closed-loop sensitivity function:

$$
|\mathbf{KS_o}|_{dB} < 0 \ dB, \quad \omega > \omega_M
\tag{3.4.18}
$$

Closed-loop bandwidth constraint

The maximum sampling frequency (f_S) chosen for all signals must at least be 6 times the closed loop bandwidth [Landau & Zito, 2006]. An important part of this thesis is the experimental validation of the proposed control schemes for the considered system of tunneling current (details in coming chapter), where the maximum sampling frequency (f_S) chosen for all signals is 30 kHz. A higher sampling frequency was not possible because of the hardware limitations. This sampling frequency imposes the limits on the closed-loop bandwidth which is taken of the order of the voltage amplifier (4 kHz) in order to avoid any aliasing phenomenon. Because of this limitation, a simple linear model is considered for synthesis of the controller, where dynamics of the piezoelectric actuator (bandwidth 120 kHz) is taken as constant gain. The obtained controller is validated in simulation with complete continuous non-linear time invariant model as given in Eq. (3.3.4).

All these desired performances and constraints, listed in Table 3.2, are used in coming sections for controller design and for performance analysis of the closed-loop system.

3.5 Digital Control Design using Pole Placement with Sensitivity Function Shaping Technique

In order to meet with the specifications listed above, a robust digital RS controller is firstly designed by using pole placement combined with the shaping of sensitivity functions. This technique is a polynomial approach which allows to place the poles in order to justify the constraints on the shape of closed-loop sensitivity functions. Details on this controller design methodology can be found in [Landau & Karimi, 1998], [Landau & Zito, 2006]. It is adopted here since it takes into account simultaneously robustness and performance specifications for the closed-loop. Notice that this methodology, aiming at a digital implementation, is based on a discrete-time model of the plant.

Table 3.2: Desired performances and corresponding constraints for the synthesis of controller

Desired performances	Controller design constraints
Stability and robustness	
$\Delta M \geq 0.5$, $\Delta \tau \geq T_S$	$\|S_o\|_\infty \leq 6 \ dB, \quad \forall \omega$
$\Delta G \geq 2$, $\Delta \phi > 29\,°$	$\|T\|_\infty \leq 3.5 \ dB, \quad \forall \omega$
avoid actuator saturations	$\|KS_o\|_\infty \leq 20 \ dB, \quad \forall \omega$
robust stability	$|\mathbf{T}| < \frac{1}{|W_I|}, \quad \forall \omega$
robust performance	$\max_\omega(\mid W_P S_o \mid + \mid W_I T \mid) < 1, \quad \forall \omega$
Measurement accuracy	
$\pm 10\%$ variations of tunneling current	$|S_o| \leq -27.2 \ dB, \quad 0 \leq \omega \leq \omega_M$
noise attenuation at controlled output	$|T| < \left\|\frac{1}{G_n}\right\|, \quad \omega > \omega_M$
Surface variations reconstruction	
noise attenuation at system input	$|KS_o| < 0 \ dB, \quad \omega > \omega_M$
Closed-loop bandwidth	Closed-loop dominant poles $\leq$ 4 kHz

ΔM = Modulus margin, $\Delta \tau$ = Delay margin, ΔG = Gain margin, $\Delta \phi$ = Phase margin, T_S = Sampling time, W_I = Uncertainty weighting function, W_P = Performance weighting filter

3.5.1   Controller structure

With usual notations, the structure of a linear time invariant discrete time model of the plant (**G**) used for digital controller design is described by:

$$G(z^{-1}) = \frac{z^{-d_l} B(z^{-1})}{A(z^{-1})} \tag{3.5.1}$$

where,

d_l = delay (in number of sampling periods)

$B(z^{-1}) = b_0 + b_1 z^{-1} + \ldots + b_{n_B} z^{-n_B}$

$$A(z^{-1}) = 1 + a_1 z^{-1} + \ldots + a_{n_A} z^{-n_A}$$

As the desired closed-loop bandwidth is taken of the order of the voltage amplifier ($4 \ kHz$) (bandwidth constraint), a simple linear model is considered for the controller synthesis, where the voltage amplifier dynamics (bandwidth $4 \ kHz$) and tunnel current sensor (CVC) (bandwidth $13 \ kHz$) are taken into account and the dynamics of the piezoelectric actuator (bandwidth 120 kHz) is taken as constant gain. The coefficients of the model polynomials, used for the controller synthesis are: $b_1 = 83.31$, $b_2 = 25.93$, $a_1 = -0.4984$, $a_2 = 0.0284$.

An RS-type polynomial controller **(K)** is proposed (according to control scheme of Fig. 3.5) with controller polynomials $R(z^{-1})$ and $S(z^{-1})$ as follows:

$$R(z^{-1}) \;\;=\;\; r_0 + r_1 z^{-1} + \ldots + r_{n_R} z^{-n_R} \tag{3.5.2}$$

$$S(z^{-1}) \;\;=\;\; 1 + s_1 z^{-1} + \ldots + s_{n_S} z^{-n_S} \tag{3.5.3}$$

The sensitivity functions shaping is done by appropriate selection of the desired closed loop poles and the introduction of pre-specified filters in the controller. Those filters are introduced in $R(z^{-1})$ and $S(z^{-1})$ as follows:

$$R(z^{-1}) \;\;=\;\; H_R(z^{-1})R'(z^{-1}) \tag{3.5.4}$$

$$S(z^{-1}) \;\;=\;\; H_S(z^{-1})S'(z^{-1}) \tag{3.5.5}$$

where $H_R(z^{-1})$ and $H_S(z^{-1})$ correspond to pre-specified fixed filters and $R'(z^{-1})$ and $S'(z^{-1})$ are "free" filters:

$$R'(z^{-1}) \;\;=\;\; r'_0 + r'_1 z^{-1} + \ldots + r'_{n_{R'}} z^{-n_{R'}} \tag{3.5.6}$$

$$S'(z^{-1}) \;\;=\;\; 1 + s'_1 z^{-1} + \ldots + s'_{n_{S'}} z^{-n_{S'}} \tag{3.5.7}$$

The desired closed loop poles are defined from a polynomial $P(z^{-1})$ of the form:

$$P(z^{-1}) = P_D(z^{-1}) \cdot P_F(z^{-1}) \tag{3.5.8}$$

where, $P_D(z^{-1})$ and $P_F(z^{-1})$ correspond to the dominant and auxiliary closed loop poles respectively. In order to compute the controller polynomials, the following equation known as "Bezout Identity" must be solved, for the unknown filters $R'(z^{-1})$ and $S'(z^{-1})$:

$$P(z^{-1}) = A(z^{-1})S(z^{-1}) + z^{-d_l}B(z^{-1})R(z^{-1}) \tag{3.5.9}$$

with $P(z^{-1})$ as in Eq. (3.5.8), $R(z^{-1})$ and $S(z^{-1})$ as in Eq. (3.5.4) and Eq. (3.5.5) respectively.

The controller polynomials $R(z^{-1})$ and $S(z^{-1})$ (more precisely $R'(z^{-1})$ and $S'(z^{-1})$) are the minimal degree solutions of Eq. (3.5.9). This polynomial equation Eq. (3.5.9) has a unique solution with minimal degree for $n_P = degP(z^{-1}) \leq n_A + n_{H_S} + n_B + n_{H_R} + d_l - 1$; $n_{S'} = degS'(z^{-1}) = n_B + n_{H_R} + d_l - 1$; $n_{R'} = degR'(z^{-1}) = n_A + n_{H_S} - 1$. For the controller implementation, $R(z^{-1})$ and $S(z^{-1})$ will be given by Eq. (3.5.4) and Eq. (3.5.5) respectively.

3.5.2 Controller synthesis

Based on the above mentioned algorithm, the designed controller characteristics are:

Closed-loop dominant poles $\mathbf{P_D}$: These dominant poles are placed at 3 kHz with damping coefficient of 0.9 so that the closed-loop natural frequency remains almost the same as the open loop one.

Closed-loop auxiliary poles $\mathbf{P_F}$: Double high frequency real poles are added at 0.2 in order to improve the controller robustness.

Controller Fixed Part $\mathbf{H_S}$: An integrator is used for H_S fixed part of the controller in order to achieve zero steady-state error.

Controller Fixed Part $\mathbf{H_S}$: A real zero has been introduced at $0.3f_S$ in order to shape the output sensitivity function.

The obtained controller polynomials after solving Bezout equation (3.5.9) are:

$$\begin{cases} R(z^{-1}) = 3.22 \times 10^{-3} - (2.34 \times 10^{-3})z^{-1} + (0.47 \times 10^{-3})z^{-2} - (0.01 \times 10^{-3})z^{-3} \\ S(z^{-1}) = 1 - (1264 \times 10^{-3})z^{-1} + (253 \times 10^{-3})z^{-2} + (10.85 \times 10^{-3})z^{-3} \end{cases} \tag{3.5.10}$$

The closed-loop performance is discussed here with simulation results after the design of digital classical PI controller for comparison purpose.

Digital classical PI control design

For the sake of comparison, a digital PI controller is designed by a loop shaping technique, using the second order model as in the case of pole placement approach, keeping in mind all the constraints which are mentioned above. The PI controller polynomials are:

$$\begin{cases} R(z^{-1}) = 0.322 \times 10^{-3} + (0.322 \times 10^{-3})z^{-1} \\ S(z^{-1}) = 1 - z^{-1} \end{cases} \tag{3.5.11}$$

The comparison of performance in simulation between the two designed controllers Eq. (3.5.10) and Eq. (3.5.11) is performed in the next sub-section.

3.5.3 Simulation results

For the sake of first validation, the sensitivity functions of the designed controller are plotted in Fig. 3.8. These sensitivity functions are plotted with complete linear time invariant model as given in Eq. 3.3.7 to analyze the performance of considered system of tunneling current. The black dotted lines indicate the maximum limits (constraints) of sensitivity functions which correspond to the desired performances as mentioned earlier. It can be observed that all constraints are fully met.

The controller performance is then validated through time responses with a simulation model (Eq. (3.3.4)), having actual non-linearities (exponential, saturations), measurement noise (n) and physical limitations in closed-loop, aiming at representing the real system as close as possible. The controller validation with such a simulation model is an important step before experimental validation.

Fig. 3.9 shows the simulation result with the classical PI controller and with the proposed RS controller in the presence of surface variations (z_S) (first graph) with a frequency of 300 rad/sec (47.75 Hz) and an amplitude of 0.5 Å. The two horizontal
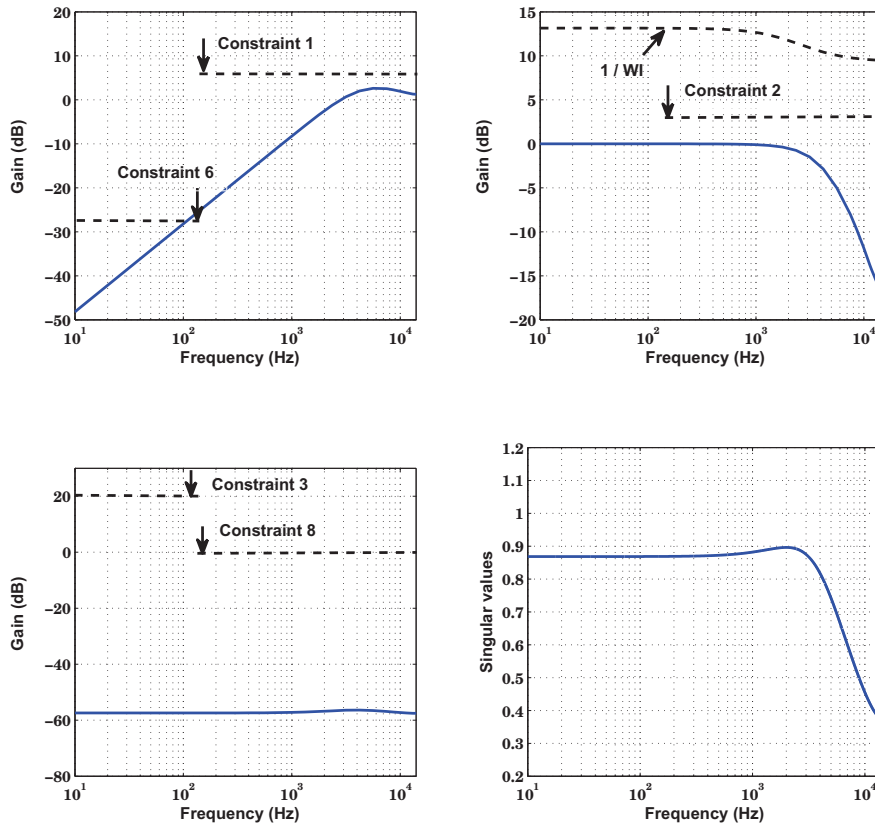
Figure 3.8: (top left) Output sensitivity function ($\mathbf{S_o}$); (top right) Complementary sensitivity function ($\mathbf{T}$); (bottom left) Input sensitivity function ($\mathbf{KS_o}$); (bottom right) System robust performance test; with **controller designed by pole placement with sensitivity functions shaping** and associated constraints

dotted lines in the second and third graphs represent the acceptable bounds of $\pm 10\%$ variations in tunneling current (i_t). The desired tunneling current value was $0.5\ nA$. It can be observed that the tunneling current variation remains within the desired limits with both designed controllers, although less variations can be noticed with the proposed RS controller designed by pole placement with sensitivity function shaping than with conventional PI controller. If a simulation is performed with a slightly higher frequency of $800\ rad/sec$ ($127.32\ Hz$) of surface variations (z_S) with an amplitude of 0.5 Å as presented in Fig. 3.10 (first graph), it can be observed that the variation in tunneling current (i_t) still remains within acceptable bounds with the proposed RS controller (third
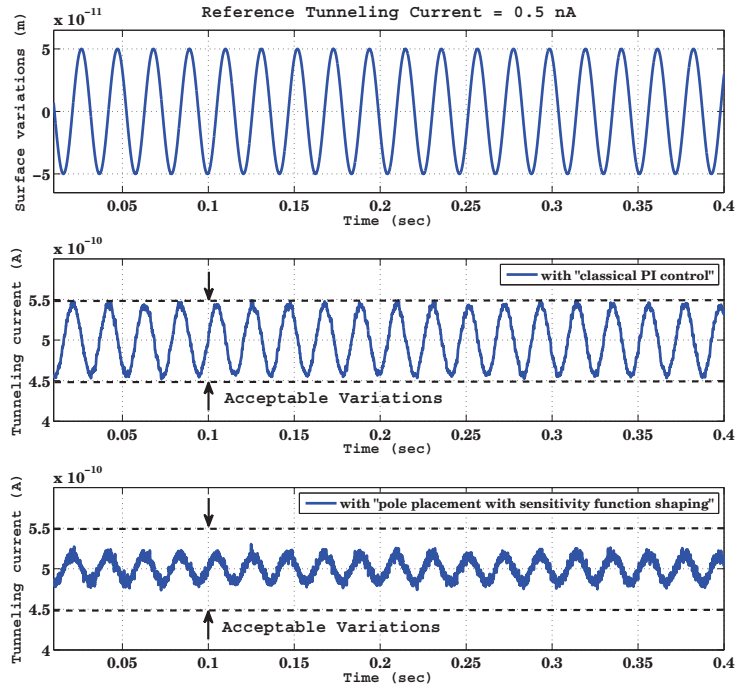
Figure 3.9: Simulation results comparison between **classical PI control** and **controller designed by pole placement with sensitivity functions shaping** in the presence of sinusoidal surface variations (z_S) of frequency of 300 rad/sec (47.75 Hz), an amplitude of 0.5 Å and measurement noise (n) of 10 $mV/\sqrt{Hz}$.

graph) but it becomes unacceptable with classical PI controller (second graph). These results show the possible higher speed STM operation with the proposed RS controller than with the conventional PI controller. All these simulations are performed in the presence of measurement noise (n) of 10 $mV/\sqrt{Hz}$.

Finally, the controllers performances are analyzed with random surface variations (z_S) (first graph in Fig. 3.11). Again, less variations in tunneling current (i_t) can be observed with the proposed RS controller (third graph) as compared to classical PI controller (second graph). The reason can be investigated by comparing the closed loop sensitivity functions (particularly closed loop output sensitivity function ($S_o(z^{-1})$)) as they carry much information about the disturbance rejection. For proper analysis in a real-time environment, these closed loop sensitivity functions are also identified with real-time experimental data in next Chapter.
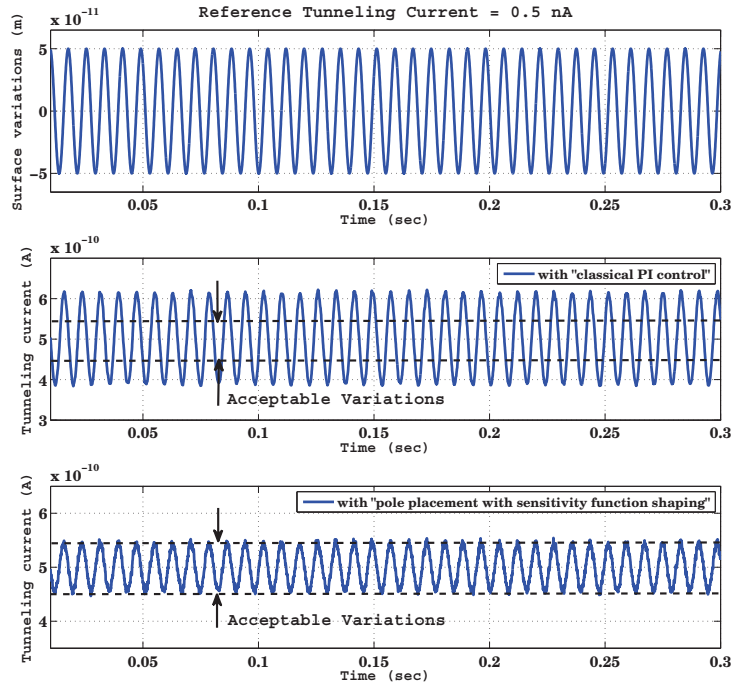
Figure 3.10: Simulation results comparison between **classical PI control** and **controller designed by pole placement with sensitivity functions shaping** in the presence of sinusoidal surface variations (z_S) of frequency of 800 rad/sec (127.32 Hz), an amplitude of 0.5 Å and measurement noise (n) of 10 $mV/\sqrt{Hz}$.

3.6 H_∞ Controller Design

A mixed sensitivity H_∞ control design methodology is adopted in this section in order to give a more complete approach to the robust control problem previously considered. The purpose is to achieve the same desired performances in terms of high measurement precision with large closed-loop bandwidth, good robustness and stability margins in the presence of external disturbances as mentioned in detail in Section 3.4. A brief description about standard H_∞ control design methodology is first recalled here, details can be found in [Skogestad & Postlethwaite, 1996]. This methodology is applied for the considered system of tunneling current and then, the control loop performance is analyzed in simulation in the presence of designed H_∞ controller, which will be validated with experimental results in the next Chapter.
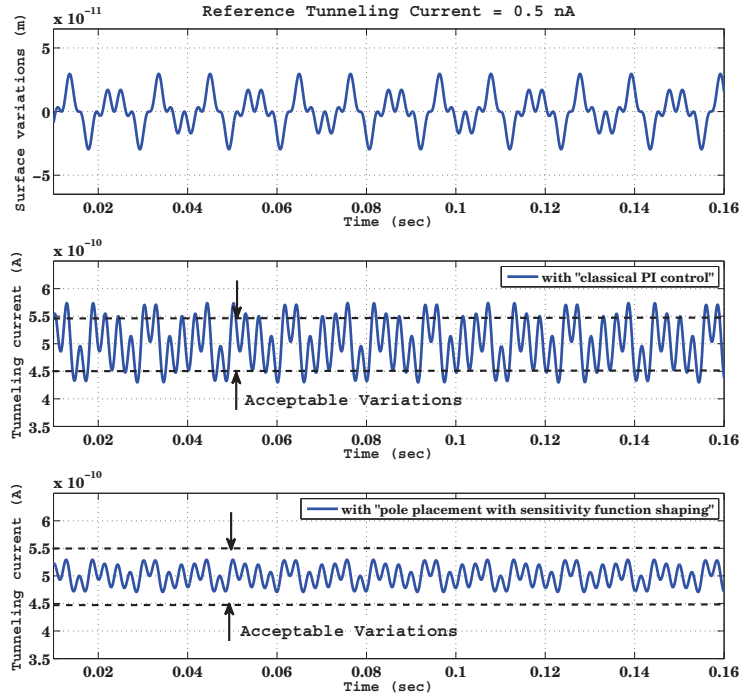
Figure 3.11: Simulation results comparison between **classical PI control** and **controller designed by pole placement with sensitivity functions shaping** in the presence of random surface variations (z_S).

3.6.1   General H$_\infty$ algorithm

The general H$_\infty$ control problem is formulated using the general control configuration (Fig. 3.12) where $\mathbf{P(s)}$ is the generalized plant model, composed by the actual system $G(s)$ and the performance weighting functions, w is the exogenous input vector (such as external disturbances (z_S, n) and reference signal (v_{ref})), u is control input signal (v_1), y is the controlled output vector and e is the error signal (v_e) which need to be minimized in some sense to meet the desired control objectives.

The system of Fig. 3.12 is described by:

$$\begin{pmatrix} y \\ e \end{pmatrix} = P(s) \begin{pmatrix} w \\ u \end{pmatrix} = \begin{pmatrix} P_{11}(s) & P_{12}(s) \\ P_{21}(s) & P_{22}(s) \end{pmatrix} \begin{pmatrix} w \\ u \end{pmatrix} \tag{3.6.1}$$

where $u = \mathbf{K(s)} \cdot e$ and $P_{11}(s)$, $P_{12}(s)$, $P_{21}(s)$ and $P_{22}(s)$ are transfer functions. The
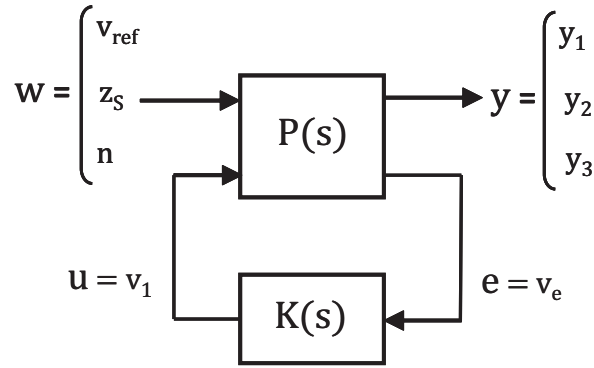
Figure 3.12: Generalized plant with controller.

generalized plant $\mathbf{P(s)}$ for the considered system of tunneling current is given in the next section. The state-space realization of the generalized plant $\mathbf{P}$ is given by:

$$P = \begin{pmatrix} A & B_1 & B_2 \\ C_1 & D_{11} & D_{12} \\ C_2 & D_{21} & D_{22} \end{pmatrix} \qquad (3.6.2)$$

The system closed-loop transfer function from w to y is given by following linear fractional transformation:

$$y = F_l(P, K) \cdot w \qquad (3.6.3)$$

where:

$$F_l(P, K) = P_{11} + P_{12}K(I - P_{22}K)^{-1}P_{21} \qquad (3.6.4)$$

The H$_\infty$ control involve the minimization of the H$_\infty$ norms of $F_l(P, K)$. The following assumptions are typically made in H$_\infty$ problems [Skogestad & Postlethwaite, 1996]:

$(A1)$ (A, B_2, C_2) is stabilizable and detectable.

$(A2)$ D_{12} and D_{21} have full rank.

$(A3)$ $\begin{pmatrix} A - j\omega I & B_2 \\ C_1 & D_{12} \end{pmatrix}$ has full column rank for all ω.

$(A4)$ $\begin{pmatrix} A - j\omega I & B_1 \\ C_2 & D_{21} \end{pmatrix}$ has full row rank for all ω.

$(A5)$ $D_{11} = 0$ and $D_{22} = 0$.

$(A6)$ $D_{12} = \begin{pmatrix} 0 \\ I \end{pmatrix}$ and $D_{21} = \begin{pmatrix} 0 & I \end{pmatrix}$.

Assumption (A1) is required for the existence of a stabilizing controller K, and assumption (A2) is sufficient to ensure the controllers are proper and hence realizable. Assumptions (A3) and (A4) ensure that the optimal controller does not try to cancel poles or zeros on the imaginary axis which would result in closed-loop instability. Assumption (A5) significantly simplifies the H_∞ algorithm formulas. For simplicity, it is also sometimes assumed that D_{12} and D_{21} are given by assumption (A6).

The standard H_∞ optimal control problem is to find all stabilizing controllers K which minimize the following quantity:

$$\|F_l(P, K)\|_\infty = \max_\omega \overline{\sigma}(F_l(P, \ K)(j\omega)) \tag{3.6.5}$$

where $\overline{\sigma}$ represents the maximum singular value. In practice, it is usually not necessary to obtain an optimal controller for the H_∞ problem, and it is simpler to design a sub-optimal one, which is close to the optimal controller, in the sense of the H_∞ norm. Let γ_{min} be the minimum value of $\|F_l(P, K)\|_\infty$ over all stabilizing controllers K. Then the H_∞ sub-optimal control problem consists in finding, given a $\gamma > \gamma_{min}$, all stabilizing controllers K such that:

$$\|F_l(P, K)\|_\infty < \gamma \tag{3.6.6}$$

For the general control configuration of Fig. 3.12 described by Eq. 3.6.4, with assumptions (A1) to (A6) listed above, there exist a stabilizing controller $K(s)$ such that $\|F_l(P, K)\|_\infty < \gamma$ if and only if:

(i) $X_\infty \geq 0$ is a solution to the algebraic Riccati equation:

$$A^T X_\infty + X_\infty A + C_1^T C_1 + X_\infty(\gamma^{-2} B_1 B_1^T - B_2 B_2^T) X_\infty = 0 \tag{3.6.7}$$

such that $Re \ \lambda_i[A + (\gamma^{-2} B_1 B_1^T - B_2 B_2^T) X_\infty] < 0, \forall i$
where λ is the eigen value.

(ii) $Y_\infty \geq 0$ is a solution to the algebraic Riccati equation:

$$A Y_\infty + Y_\infty A^T + B_1 B_1^T + Y_\infty(\gamma^{-2} C_1^T C_1 - C_2^T C_2) Y_\infty = 0 \tag{3.6.8}$$

such that $Re\ \lambda_i[A + Y_\infty(\gamma^{-2}C_1^T C_1 - C_2^T C_2)] < 0, \forall i$

(iii) $\rho(X_\infty Y_\infty) < \gamma^2$

The family of all admissible controllers is given by $K = F_l(K_c, Q)$, where:

$$K_c = \begin{pmatrix} A_\infty & -Z_\infty L_\infty & Z_\infty B_2 \\ F_\infty & 0 & I \\ -C_2 & I & 0 \end{pmatrix} \tag{3.6.9}$$

$$F_\infty = -B_2^T X_\infty, \quad L_\infty = -Y_\infty C_2^T, \quad Z_\infty = (I - \gamma^{-2}Y_\infty X_\infty)^{-1} \tag{3.6.10}$$

$$A_\infty = A + \gamma^{-2}B_1 B_1^T X_\infty + B_2 F_\infty + Z_\infty L_\infty C_2 \tag{3.6.11}$$

and $Q(s)$ is any stable proper transfer function such that $\|Q\|_\infty < \gamma$. For $Q(s) = 0$, we get:

$$K(s) = -Z_\infty L_\infty(sI - A_\infty)^{-1}F_\infty \tag{3.6.12}$$

The controller $K(s)$ has the same number of states as the generalized plant $P(s)$.

An important part of H$_\infty$ control design methodology is the selection of some weights on the controlled outputs which represent the performance specifications in the frequency domain. The generalized plant **P** thus includes the actual system and the considered weights (W_p, W_u and W_t) as shown in Fig. 3.13 and in Fig. 3.14. The H$_\infty$ control problem is then referred to as a mixed-sensitivity problem, W_p, W_u and W_t thus appearing in the Eq. (3.6.4) as weights on the sensitivity functions.

Mixed-sensitivity is the name given to transfer function shaping problems in which closed-loop sensitivity functions are shaped according to the designed weighting functions. The transfer function shaping approach uses H$_\infty$ optimization to shape the singular values of specified closed-loop transfer functions over the frequency. The maximum singular values are easy to shape by forcing them to lie below user defined bounds, thereby ensuring desirable bandwidths and roll-off rates. We have chosen to use the loop shaping approach by mixed-sensitivity H$_\infty$ control for our considered system of tunneling current.
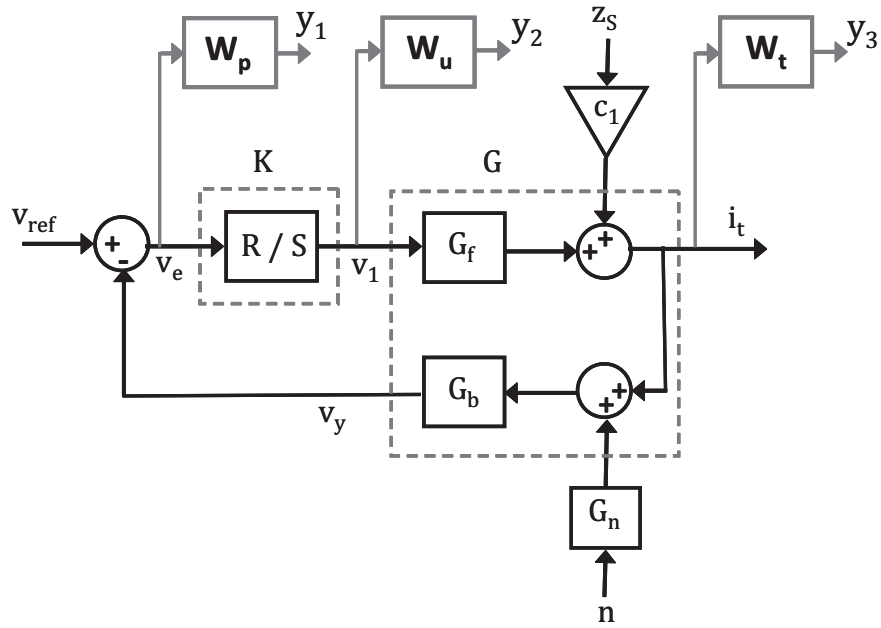
Figure 3.13: Design model with weighting functions for the considered system of tunneling current.

3.6.2   Controller synthesis

The desired performances are imposed on the closed-loop sensitivity functions using appropriate weighting functions and then the mixed-sensitivity H_∞ control design methodology is adopted to fulfill the requirements. The functions W_p, W_u and W_t weight the controlled outputs y_1, y_2 and y_3 respectively (Fig. 3.13) and should be chosen according to the desired performance specifications (Section 3.4).

The generalized plant $\mathbf{P}$ (Fig. 3.14) (*i.e.* the interconnection of the actual system and the weighting functions) for our considered system of tunneling current is given by:

$$
\begin{pmatrix} y_1 \\ y_2 \\ y_3 \\ v_e \end{pmatrix} = \underbrace{\begin{pmatrix} W_p & -c_1 G_b W_p & -W_p & -G_f G_b W_1 \\ 0 & 0 & 0 & W_u \\ 0 & c_1 W_t & 0 & G_f W_t \\ I & -c_1 G_b & I & -G_f G_b \end{pmatrix}}_{P} \begin{pmatrix} v_{ref} \\ z_s \\ n \\ v_1 \end{pmatrix}
$$

where G_f, G_b and c_1 have been defined earlier in section 3.3.3. Thus, the H_∞ control
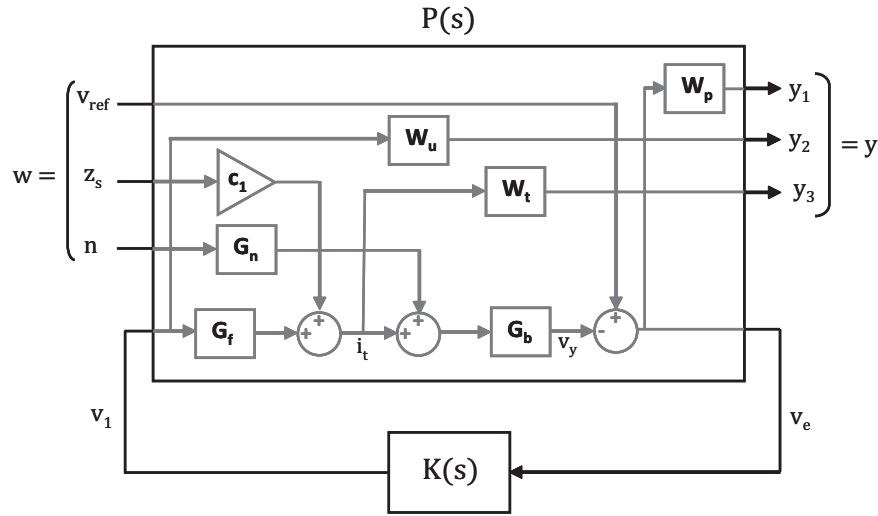
Figure 3.14: Generalized design model for considered system of tunneling current.

problem is to find a stabilizing controller $K(s)$ which minimizes γ such that:

$$\left\| \begin{pmatrix} (W_p)S & (-c_1 G_b W_p)S & (-W_p)S \\ (W_u)KS & (-c_1 G_b W_u)KS & (-W_u)KS \\ (G_b^{-1} W_t)T & (c_1 W_t)S & (-G_b^{-1} W_t)T \end{pmatrix} \right\|_\infty < \gamma \qquad (3.6.13)$$

The obtained controller $K(s)$ has the same number of state variables as P. So, the choice of the weighting functions is an important issue in the H$_\infty$ control problem, keeping in mind the real time implementation of the controller for the purpose of validation. The chosen weighting functions according to the desired performance requirements (Section 3.4 and Table. 3.2) are as follows:

(1) : $\mathbf{W_p}$ is used to impose the desired performances on the closed-loop output sensitivity function S_o in terms of robustness and measurement precision, that is:

$$W_p(s) = \frac{(1/M_s)\, s + \omega_s}{s + \omega_s \cdot \epsilon_s} \qquad (3.6.14)$$

where $M_s = 2$ to have a good robustness and stability margins (*i.e.* $\|S\|_\infty \leq 6$ dB) for all frequency range, $\omega_s = 1.2 \times 10^4 \; rad/sec$ (1.9 kHz) to have a good attenuation of disturbances from low frequency up to ω_s and ϵ_s is chosen a very small value to induce an integral effect and to eliminate the steady-state error in the presence of maximum allowed variations in the sample surface (z_S).

(2) : $\mathbf{W_u}$ is designed to avoid actuator saturations and also to attenuate the noise (n) at system input for the considered system of tunneling current. It is chosen as follows:

$$W_u(s) = \frac{s + (\omega_u/M_u)}{\epsilon_u \cdot s + \omega_u} \tag{3.6.15}$$

where $M_u = 10$ to impose limitation on the maximum value of controller output up to the frequency ω_u which is chosen $\omega_u = 1.88 \times 10^4 \ rad/sec$ (3 kHz) and $\epsilon_u = 0.5$ to limit the effect of noise (n) at high frequencies on system input as mentioned in desired performances.

(3) : $\mathbf{W_t}$ is designed to impose limitations on the complementary sensitivity function (T) in order to achieve good robustness and to attenuate the noise (n) at controller output. It is chosen as:

$$W_t(s) = \frac{s + (\omega_t/M_t)}{\epsilon_t \cdot s + \omega_t} \tag{3.6.16}$$

where $M_t = 1.5$ to have a good robustness margin (*i.e.* $\|T\|_\infty \leq 3.5 \ dB$) for all frequency range, $\omega_t = 1.88 \times 10^4 \ rad/sec$ (3 kHz) to attenuate the noise (n) at high frequencies with $\epsilon_t = 0.5$.

As mentioned for the case of pole placement with sensitivity function shaping control (Section 3.5.1), again a simplified system model is considered for the controller synthesis. As three weighting functions with first order transfer functions are designed so, an H$_\infty$ controller with 4th order transfer function is achieved. After computation, the minimal cost achieved for the considered system of tunneling current was $\gamma = 0.95$, which means that the obtained sensitivity functions match the desired loop shaping. For an actual digital implementation, the controller is discretized using a standard Tustin method and giving the following coefficients for RS polynomials of the controller (with sampling frequency of 30 kHz): $r_0 = 6.33 \times 10^{-3}$, $r_1 = 0.85 \times 10^{-3}$, $r_2 = -3.97 \times 10^{-3}$, $r_3 = 1.38 \times 10^{-3}$, $r_4 = -0.14 \times 10^{-3}$ and $s_1 = -466.1 \times 10^{-3}$, $s_2 = -933.9 \times 10^{-3}$, $s_3 = 451.7 \times 10^{-3}$, $s_4 = -51.6 \times 10^{-3}$.
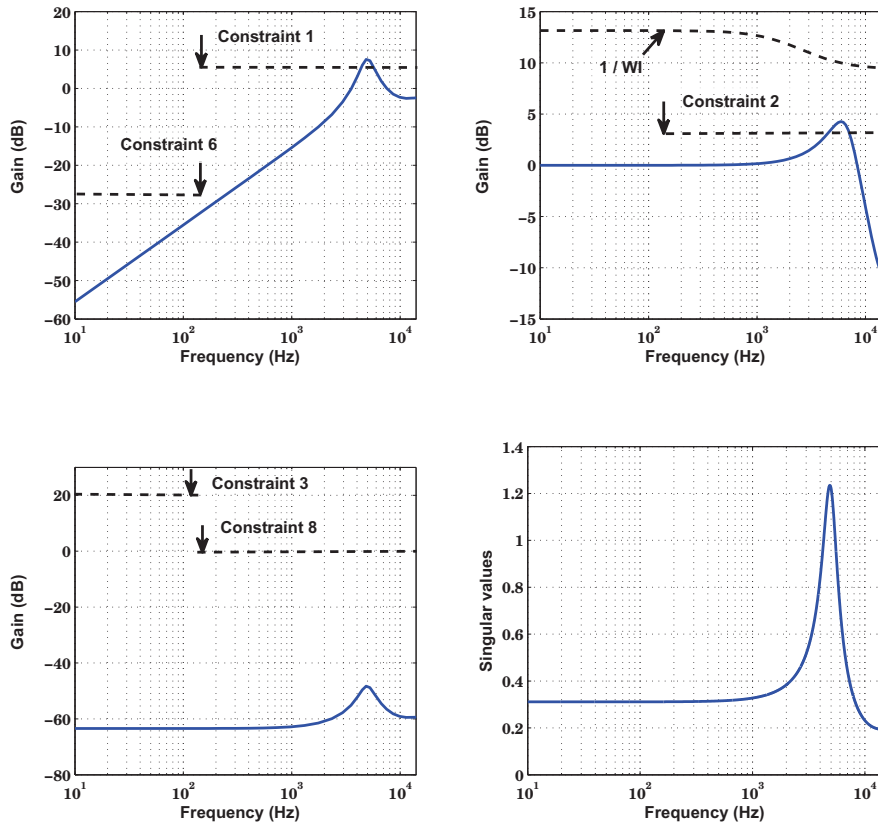
Figure 3.15: (top left) Output sensitivity function ($\mathbf{S_o}$); (top right) Complementary sensitivity function ($\mathbf{T}$); (bottom left) Input sensitivity function ($\mathbf{KS_o}$); (bottom right) System robust performance test; with **mixed sensitivity $\mathbf{H_\infty}$ control** and associated constraints

3.6.3   Simulation results

The obtained sensitivity functions of the designed controller are plotted in Fig. 3.15. Again, these sensitivity functions are plotted with complete linear time invariant model as given in Eq. (3.3.7). It can be observed that all constraints are almost met.

The weighting functions (W_p, W_u and W_t) were designed considering the desired performance requirements (Section 3.4). After the control design, the performance of the considered system of tunneling current is validated with a complete simulation feedback loop (Fig. 3.1), having actual non-linearities and physical limitations in closed-loop. All

these simulations are performed in the presence of noise (n) of $10 \ mV/\sqrt{Hz}$. Again, the performance comparison is performed with conventional PI controller as designed earlier (Eq. (3.5.11)). The desired tunneling current was considered as 0.5 nA.
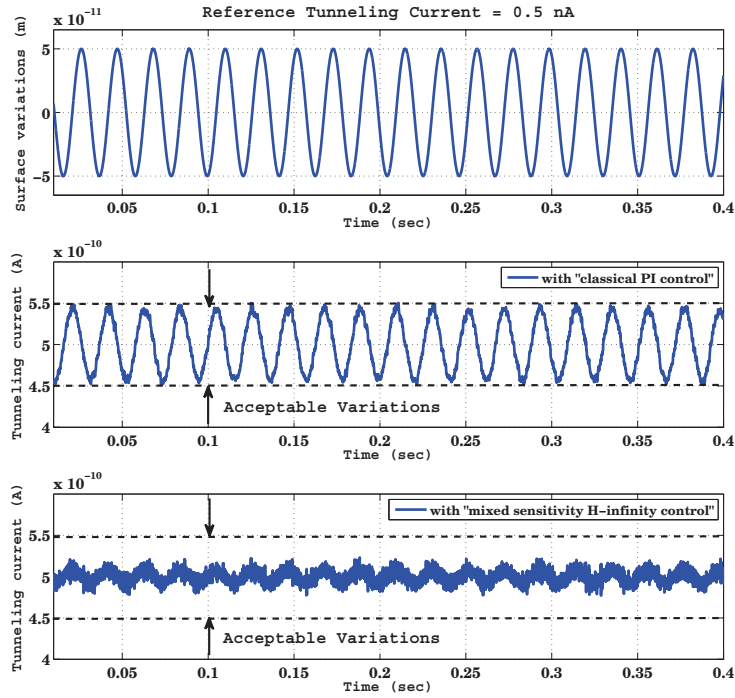
Figure 3.16: Simulation results comparison between **classical PI control** and **mixed sensitivity H$_\infty$ control** in the presence of sinusoidal surface variations (z_S) of frequency of 300 rad/sec (47.75 Hz), an amplitude of 0.5 Å and measurement noise (n) of $10 \ mV/\sqrt{Hz}$.

Fig. 3.16 shows the first simulation result with the designed H$_\infty$ controller and with classical PI controller in presence of surface variations (z_S) with a frequency of 300 rad/sec (47.75 Hz) and an amplitude of 0.5 Å. It can be observed that the tunneling current variation remains within the desired limits with both designed controllers. Less variations can be observed with the proposed controller than with the conventional PI controller. Again, if a simulation is performed with a slightly higher frequency of 800 rad/sec (127.32 Hz) of surface variations (z_S) with an amplitude of 0.5 Å, still less variations can be observed in Fig. 3.17 with the designed H$_\infty$ controller (remains within acceptable bounds) but these variations become unacceptable with conventional

PI controller (exceeded the acceptable bounds).
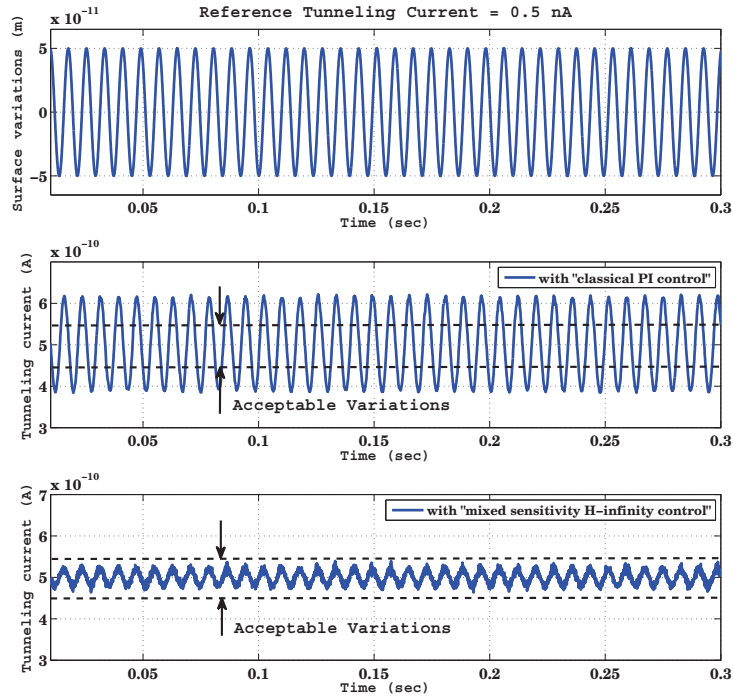
Figure 3.17: Simulation results comparison between **classical PI control** and **mixed sensitivity H$_\infty$ control** in the presence of sinusoidal surface variations (z_S) of frequency of 800 rad/sec (127.32 Hz), an amplitude of 0.5 Å and measurement noise (n) of 10 $mV/\sqrt{Hz}$.

Finally, the performances of controllers are analyzed with random surface variations (z_S) (first graph in Fig. 3.18). As in the case of pole placement, less variations in tunneling current (i_t) can be observed with the proposed H$_\infty$ controller (third graph) as compared to conventional PI controller (second graph).

As mentioned for the former robust control design, closed-loop sensitivity functions are helpful in justifying these results and they will also be identified with real-time experimental data in next Chapter.
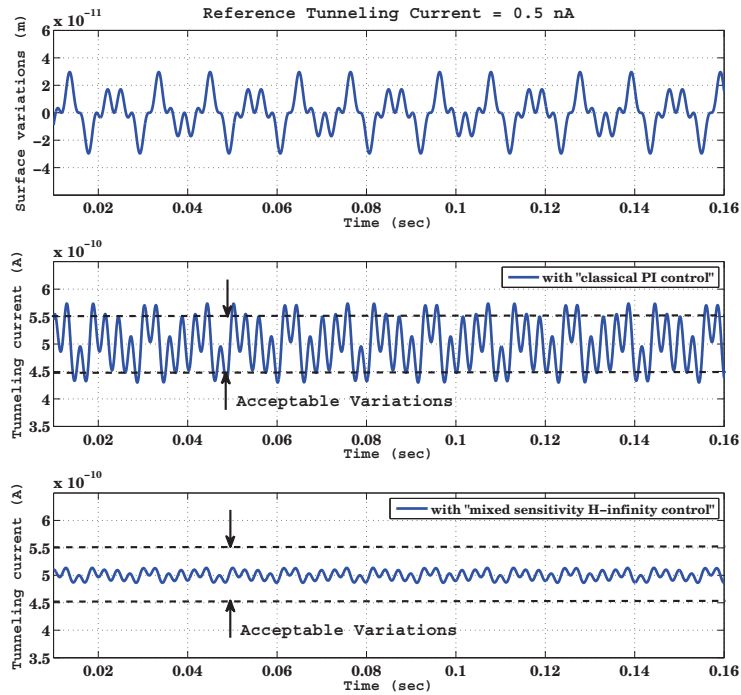
Figure 3.18: Simulation results comparison between **classical PI control** and **mixed sensitivity H$_\infty$ control** in the presence of random surface variations (z_S).

3.7   Conclusion

In this chapter, after highlighting the motivation of this work, a system of tunneling current measurement has been briefly presented, a corresponding dynamic modeling has been proposed and a related control problem with desired measurement performance has been formulated. Then, measurement requirements have been translated into control requirements and modern robust control techniques have been proposed. Firstly RS control designed by combined pole placement with sensitivity function shaping method and then mixed-sensitivity H$_\infty$ have been designed. A common approach for the system of tunneling current is to use classical PI control, so a comparison has been performed with conventional PI control design methodology.

Simulations results have shown better performances in terms of precision and disturbance rejection with the proposed controllers for the system of tunneling current

measurement. Less variations of tunneling current have been observed with the proposed controllers. By comparing the output sensitivity function with both proposed controllers (Fig. 3.8 and Fig. 3.15), a little stronger attenuation of external disturbances for a large band of frequencies has been observed with the proposed H_∞ control, as compared with the proposed controller designed by pole placement with sensitivity function shaping. The results obtained in this Chapter still need to be validated with real time experimental results.

The experimental setup, explained in details in next Chapter, works at ambient temperature so additional external environmental disturbances can be present beyond the disturbances considered for simulations (measurement noise (n) and sample surface variations (z_S)). More than time-domain results, the closed loop sensitivity functions also carry much information about all performance requirements, like measurement precision, bandwidth, robustness and stability, as highlighted in this Chapter. So, it will be interesting to analyze the performance of the system of tunneling current measurement with real time experimental data. The closed loop sensitivity functions, which are identified with real time experimental data in coming Chapter, and also the time domain experimental results will help us to perform a comparison between the two proposed control techniques.

Experimental Analysis and Control Results

An experimental setup has been developed in Gipsa-lab, Grenoble by the control group, in order to analyze the influence of different control techniques on tunneling current measurement. This setup works at ambiant temperature and is based on STM principles, although the purpose is not to take images of the surface. At nanometer scale, working over an experimental platform at ambient atmosphere in the presence of many unknown environmental disturbances was the real challenge. Many problems in terms of handling and repeatability have been encountered.

All necessary details including hardware characteristics, experimental constraints and the procedure proposed in order to bring the tip in the tunneling region (distance between tip and sample surface less than 1×10^{-9} m) without collision is presented in Section 4.1.

System identification is performed in Section 4.2 and also experimental identification of closed loop sensitivity functions with conventional and proposed control techniques is presented in Section 4.3.

Time domain experimental results of tunneling current with conventional and proposed control techniques for comparison are presented in Section 4.4 and Section 4.5 respectively.

Some discussion on achieved results is done in Section 4.6 and finally Section 4.7 draws some conclusions.

4.1 Experimental Platform

In this section, all necessary details of the experimental setup (Fig. 4.1), developed in Gipsa-lab, Grenoble is presented [Blanvillain, 2010]. Experimental constraints and also the strategy in order to bring the tip close enough to the sample surface (distance between tip and sample surface less than 1 nm) to observe the tunneling current are given.

4.1.1 Experimental details
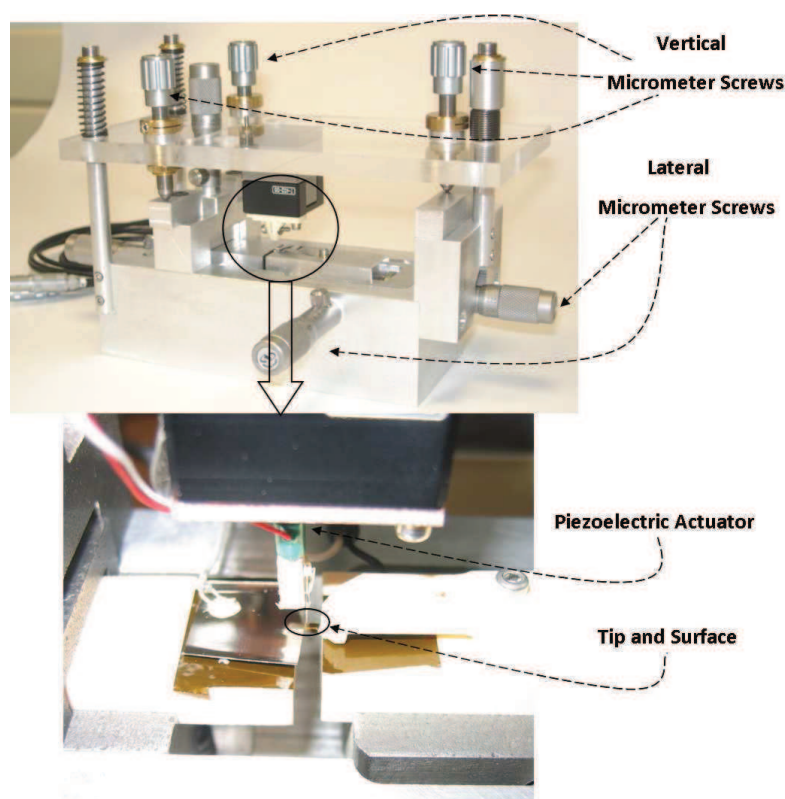
Figure 4.1: Experimental platform developed in Gipsa-lab.

The experimental setup is based on the STM working principle. A very sharp tip (*platinum / iridium*, work function $\Phi = 5.6~eV$) needs to be brought close to sample surface (*gold*, work function $\Phi = 5.4~eV$) until tunneling current is obtained. The tips can be prepared by electrochemical reactions and few relevant work can be found in [Libioulle et al., 1995], [Weinstein et al., 1995], [Sorensen et al., 1999], [Rogers et al., 2000]. The tip is fixed in a holder which is attached with piezoelectric actuator to
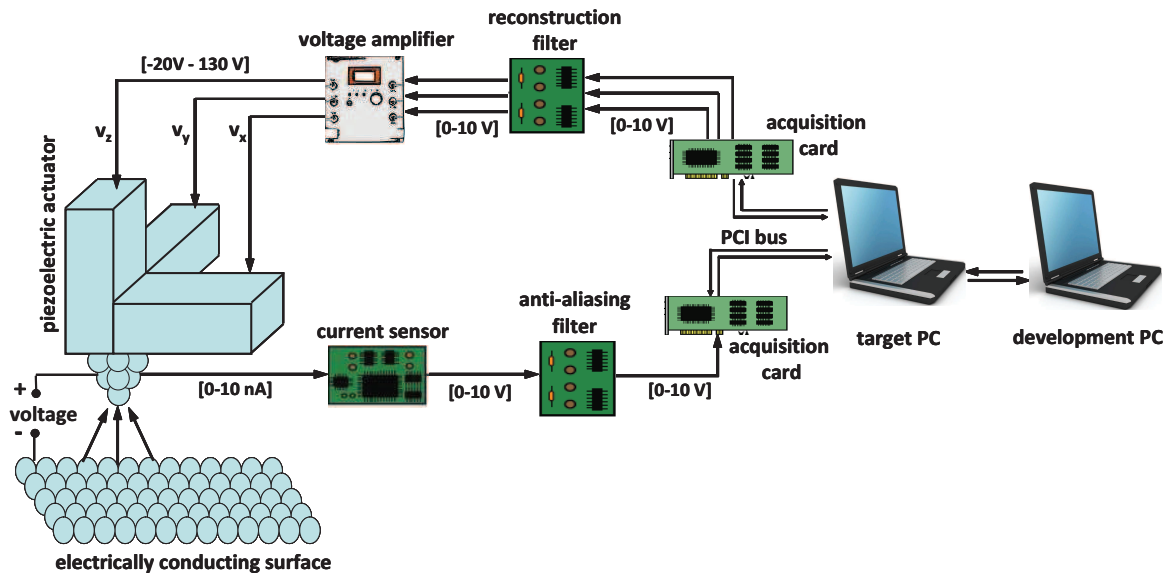
Figure 4.2: Closed loop with all hardware elements of experimental platform.

move the tip in vertical z-direction. The piezoelectric actuator (*Piezomechanics / PSt 150*) has a resonance frequency of 120 kHz, a gain of 1.2 nm/V and an input voltage range from -20 V to 130 V. The output of the controller is between ± 10 V and a voltage amplifier (*Piezojena / ENV 300*) having a gain of 15 V/V and a bandwidth of 4 kHz, provides appropriate signals to the piezoelectric actuator. The change in distance (d) between tip and sample surface modifies the tunneling current (i_t) and a tunneling current sensor (*CVC*) (*home-made*) of bandwidth 13 kHz and of gain 10^9 V/A, gives the signal to the controller. The CVC is fixed close enough to the tip to minimize the measurement noise (n). The sample surface is placed over a small bench which can be moved laterally very precisely in x- and y-directions with the help of two micrometer screws (*Newport / HR-13*) having travel range of 13 mm and sensitivity of 0.5 μm. Three other micrometer screws (*Newport / AJS-0.5*) having the same travel range of 13 mm and sensitivity of 0.6 μm are attached with the piezoelectric actuator platform to move the tip manually in vertical z-direction. These sensitivities of the screws are based on a 1° rotation of the adjustment micrometer screws. These micrometer screws and camera (*μEye / CMOS UI-1550-C*) with telecentric zoom (*VS-Technology / VS-TC-10-65*) help the operator to bring the tip manually close to the sample surface so that the distance between them is in the range of few micro-meters. Further tip approach

mechanism is done with the help of piezoelectric actuator until the tunneling current (i_t) is obtained. Tip approach strategy in order to obtain the tunneling current is described in the next sections. The whole experimental setup is placed over an anti-vibration table (*Microworld*). The control scheme is implemented in a computer (*Development PC*, processor 2.5 GHz, Matlab) connected with another computer (*Target PC*, processor 3.2 GHz, XPCTarget) through Ethernet. The *Target PC* has acquisition card (*PCI DAS 1602/16*, 8 differential inputs, 2 outputs, 16 bits resolution) connected with the experimental setup. The complete feedback loop with all signals and the hardware involved in shown in Fig. 4.2. The numerical values of the most important elements of this system are summarized in Table 4.1. They have been used for the design models considered in Chapter 3. The values of this table have been obtained as follows:

- Identification on the real set-up has been used to obtain $\phi_{Pt/Ir}$ and ϕ_{Au}, based on the exponential behavior of the tunneling current recorded [Blanvillain, 2010].

- Data sheet information has been used for G_v, ω_v and ω_a.

- Home-made current sensor (CVC) allows to have G_c and ω_c.

- Finally, G_a has been adjusted to give a global gain equal to the one identified on the real-time experiment (see Fig. 4.5 in section 4.2).

Notice that some uncertainty remains in the value of the current sensor gain G_c (which could be 20 or 30 times smaller than expected), this information being available only at the end of this manuscript writing. In future work, this value has to be thoroughly identified, as it can have a large impact on the simulation of disturbances effect on the output.

4.1.2 Experimental constraints

Before presenting the approach for obtaining the tunneling current, it is necessary to clarify the constraints imposed by the experimental platform.

Table 4.1: Characteristics of devices used for the considered system of tunneling current

Material	Characteristics
Work function of tip	$\phi_{Pt/Ir} = 5.6$ eV
Work function of sample surface	$\phi_{Au} = 5.4$ eV
Gain of voltage amplifier	$G_v = 15$ V/V
Bandwidth of voltage amplifier	$\omega_v \approx 4$ kHz
Gain of piezoelectric actuator	$G_a \approx 1.2$ nm/V
Bandwidth of piezoelectric actuator	$\omega_a = 120$ kHz
Gain of current sensor	$G_c = 10^9$ V/A
Bandwidth of current sensor	$\omega_c \approx 13$ kHz

- The measurement range of the current sensor output (CVC) is between 0 V to 10 V, which corresponds to a range of motion of the tip under few angstroms. To keep the tip within such small measurement range by working in open loop is really difficult and thus, working in closed loop is really essential.

- The major difficulty is the repeatability of good operating and environmental conditions to obtain the tunneling current. Since the platform works at ambient temperature, the composition of tunneling current is more complex and many external environmental disturbances can be present beyond the disturbances considered for simulations. The controller must be indeed robust and have a capability to reject the external disturbances in order to achieve the desired performances.

- The tunneling current is a quantum mechanical phenomenon, and its understanding, exploitation and implementation require knowledge in the areas related to physics. The complete analysis of the results and understanding by working in a

department of controls was a real challenge.

- By bringing a very clean sharp tip close to a clean sample surface, one might expect a very low level of noise in measured signal. But, suddenly a situation quite complex might occur where measured signal is full of noise and it is very difficult to find the explanation of this observed noise. The only way is to change the tip or/and sample surface. We have performed our experiments on different samples and different tips.

- At atomic scale, the materials move slowly with temperature variations. These movements can be the source of contact (collision) between the elements (like tip and sample surface) during inactive periods. To avoid this contact, the platform allows with the help of micro meter screws to remove these elements from each other a few millimeters. The elements can be placed in the desired configuration (distance less than one nanometer) to perform a test. Since it is impossible to put the elements in exactly identical conditions to the tests performed previously with nanometer resolution, the experimental conditions are different in different tests.

4.1.3   Tip approach for obtaining tunneling current

Because of the current sensor (CVC) output voltage saturation (0 to 10 V), the measurement range of tunneling current is between few hundreds of picometers. The tip must reach this measurement range with a resolution of the order of picometers. This type of approach in real-time can be very slow. A strategy of approach-withdrawal has been proposed in order to achieve the tunneling current [Blanvillain, 2010].

This strategy is in two steps:

1. Manual approach
2. Fine approach.

Manual approach starts by bringing the tip, initially far from the sample surface, close to sample surface with the help of vertical micrometer screws and camera with telecentric zoom. One has to be very careful in order to avoid any contact between tip and
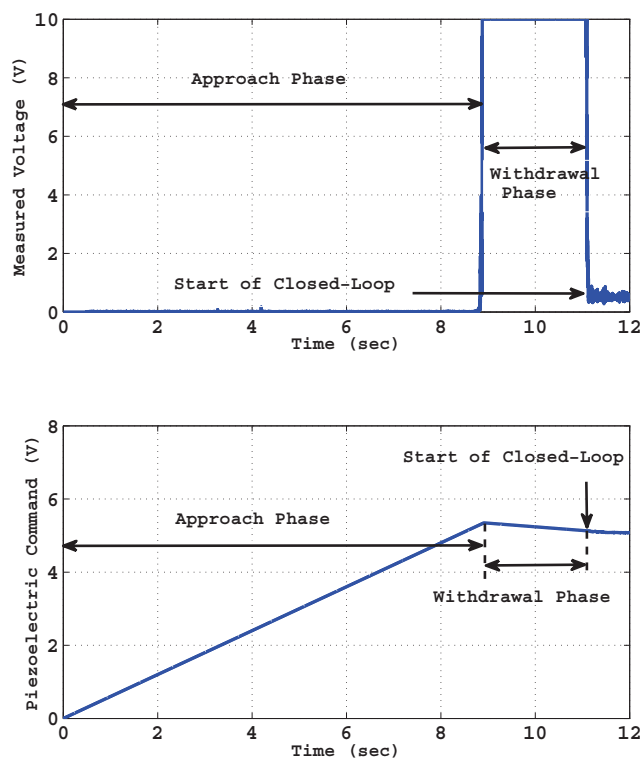
Figure 4.3: Strategy of tip approach for obtaining tunneling current.

sample surface. Once the tip is close enough to sample surface, the fine approach will start. According to this fine approach, the tip first approaches rapidly towards the sample surface with the help of piezoelectric actuator until the tunneling current saturates (approach phase). Tunneling current saturation implies that the tip has exceeded the measurement range and is now very close to the sample surface. Now, the input of piezoelectric actuator is changed and the tip is moved very slowly away from the sample surface (withdrawal-phase) until the tip arrives within the measurement range. The control loop is closed as soon as the tip arrives at the desired reference value of tunneling current. Fig. 4.3 shows the complete strategy of this fine approach for obtaining the tunneling current.

4.2   System Identification

In this section, the open loop system (plant) between the output of the controller (v_1) and the measured voltage (v_y) is identified by the techniques of identification in closed loop. The objective of the identification in closed loop is to find the best plant model which minimizes the prediction error between the measured output of the true closed loop system and the predicted closed loop output. Here, we give a brief recall the closed loop identification principle and then apply it it to our considered system in order to identify the plant model. All details with algorithms about identification in closed loop can be found in [Landau & Zito, 2006].

Identification in closed-loop:
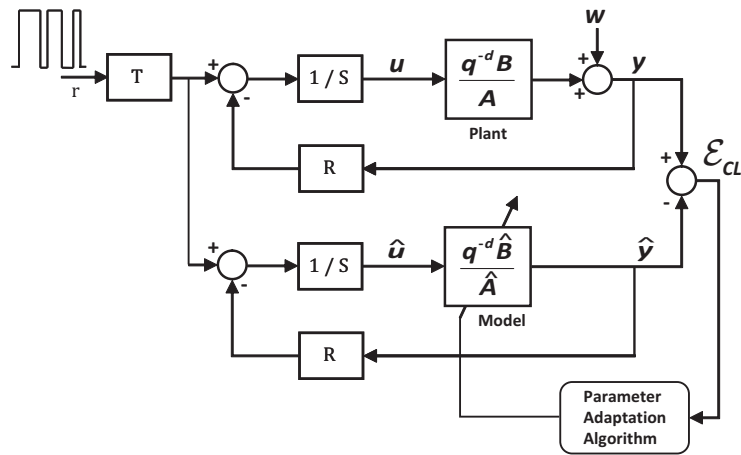
Figure 4.4: Closed loop output error identification method.

The general principle of closed loop identification can be seen in Fig. 4.4, where the upper part represents the real closed loop system and the lower part represents an adjustable predictor of the closed loop. The external excitation signal is superposed to the reference signal.

The first order discrete time plant model is described by:

$$y(t+1) = -a_1 y(t) + b_1(t)u(t) = \theta^T \phi(t) \tag{4.2.1}$$

where $\theta^T = [a_1, b_1]$ is unknown parameter vector and $\phi^T(t) = [-y(t), u(t)]$ measurement

vector. The control signal $u(t)$ delivered by the controller is given by:

$$u(t) = \frac{T(q^{-1})}{S(q^{-1})}r(t) - \frac{R(q^{-1})}{S(q^{-1})}y(t) \qquad (4.2.2)$$

where $r(t)$ is the input excitation signal and $R(q^{-1})$, $S(q^{-1})$ and $T(q^{-1})$ are controller parameters. The adjustable closed loop predictor uses a controller identical to the one used in the real time system and its output is described by:

$$\hat{y}^\circ(t+1) = -\hat{a}_1(t)\hat{y}(t) + \hat{b}_1(t)\hat{u}(t) = \hat{\theta}^T(t)\hat{\phi}(t) \qquad (4.2.3)$$

where $\hat{y}^\circ(t+1)$ is the predicted output at the instant t based on the knowledge of the parameters estimated at time t. $\hat{\theta}^T(t) = [\hat{a}_1(t), \hat{b}_1(t)]$ is the vector of estimated parameters at time t and $\hat{y}^\circ(t+1)$ is called the *a priori* prediction. *A priori* prediction error is given by:

$$\varepsilon^\circ_{CL}(t+1) = y(t+1) - \hat{y}^\circ(t+1) \qquad (4.2.4)$$

To evaluate the quality of the new estimated parameter vector $\hat{\theta}(t+1)$, which will be provided by the parameter adaptation algorithm, it is useful to define the *a posteriori* output of the adjustable predictor, which corresponds to re-computing Eq. (4.2.3) with the new values of the parameters estimated at $t+1$. The *a posteriori* predictor output is defined by:

$$\hat{y}(t+1) = -\hat{a}_1(t+1)y(t) + \hat{b}_1(t+1)\hat{u}(t) = \hat{\theta}^T(t+1)\hat{\phi}(t) \qquad (4.2.5)$$

and also an *a posteriori* prediction error is:

$$\varepsilon_{CL}(t+1) = y(t+1) - \hat{y}(t+1) \qquad (4.2.6)$$

A recursive parametric adaptation algorithm with memory is desired. The structure of such an algorithm is:

$$\hat{\theta}(t+1) = \hat{\theta}(t) + f\left(\hat{\theta}(t), \hat{\phi}(t), \varepsilon^\circ_{CL}(t+1)\right) \qquad (4.2.7)$$

where the correction term f must only depend upon the information available at instant $t+1$. This correction term should allow to minimize at each step the *a priori* prediction error with respect to the criterion:

$$\min_{\hat{\theta}(t)} J(t+1) = [\varepsilon^\circ_{CL}(t+1)]^2 \qquad (4.2.8)$$

One can use the gradient parameter adaptation algorithm to minimize the above criterion, however such parametric adaptation algorithm based on *a priori* prediction error can introduce possible instabilities [Landau & Zito, 2006]. In order to avoid the possible instabilities, one can use the same gradient approach but with a different criterion based on minimization of the *a posteriori* prediction error at each step according to:

$$\min_{\hat{\theta}(t+1)} J(t+1) = [\varepsilon_{CL}(t+1)]^2 \tag{4.2.9}$$

By using the gradient algorithm, at each step $\varepsilon^2(t+1)$ is minimized but such minimization at each step does not necessarily lead to the minimization of $\sum_{i=1}^{t} \varepsilon^2(i)$ on a t-steps time horizon. Therefore, we have chosen the least square recursive algorithm which minimizes the criterion:

$$\min_{\hat{\theta}(t)} J(t) = \sum_{i=1}^{t} \left[y(i) - \hat{\theta}^T(t)\hat{\phi}(t-1) \right]^2 = \frac{1}{t} \sum_{i=1}^{t} \varepsilon_{CL}^2 \left(i, \hat{\theta}(t) \right) \tag{4.2.10}$$

The objective is therefore the minimization of the sum of the squares of the prediction errors. Thus, the objective of the identification in closed loop is to minimize the prediction error between the measured output of the real system and the predicted closed loop output by finding the best plant model close to real system.

Application:

The external excitation signal must have a rich frequency spectrum in order to cover the bandwidth of the plant to be identified. Thus, a PRBS (Pseudo-Random Binary Sequences) which is a sequence of rectangular pulses that approximates a discrete time white noise and has a spectral content rich in frequencies, can be superposed to the reference signal. In order to correctly identify the steady state gain of the plant dynamic model, the duration of, at least, one of the pulses must be greater than the rise time of the plant. The characteristics of PRBS signal are chosen as: ampliture = ±0.1 V, number of registers = 10, sampling frequency = 30 kHz and frequency divider = 2. The identification method CLOE (Closed Loop Output Error) is used to identify the best model of the system (plant).

The theoretical gain of the open loop system (plant) which includes voltage amplifier, piezoelectric actuator, the physical tunneling current phenomenon and the current sensor

(CVC), is 309 V/V and the identified gain of the open loop system is 316 V/V. The identified bandwidth of the open loop system is also very similar to the theoretical one ($\approx$ 4 kHz). Fig. 4.5 shows the Bode plot of the identified model, the complete linearized simulation model (Eq. (3.3.7)) and the design model (used for the synthesis of the controller) of the open loop system (plant). The difference between identified model and design model will be handled by the robustness of the designed controller.
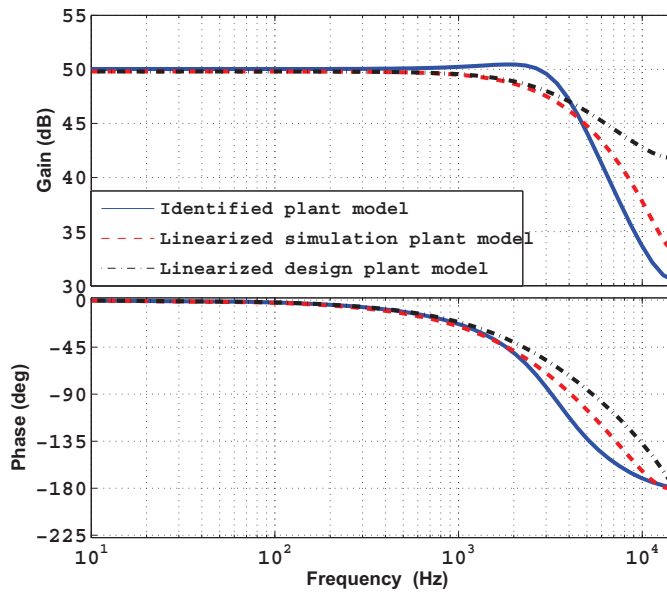
Figure 4.5: Bode diagram of tunneling current measurement system plant ($\mathbf{G}$) model.

4.3 Sensitivity Functions Identification

In this section, the experimental results with comparison between conventional PI and proposed control techniques are presented for the considered system of tunneling current. This comparison is performed with the experimentally identified closed loop sensitivity functions. The capability of the control system to reject all external disturbances can be analyzed through closed loop sensitivity functions. All the desired performances are already expressed in the previous chapter by means of constraints on the shape of the closed loop sensitivity functions (section 3.4) which helped us for the controllers synthesis.

It will be seen that those identified sensitivity functions maybe slightly different from those obtained with the simulation model in Chapter 3. This can be due to the differences between experiment and simulation conditions.

For the purpose of experimental identification of the closed loop sensitivity functions, the external excitation signal PRBS (Pseudo-Random Binary Sequences) is superposed to the reference, with the same characteristics as before: amplitude $= \pm 0.1$ V, number of registers $= 10$, sampling frequency $= 30$ kHz and frequency divider $= 2$. Based on the experimental data in the presence of the proposed control techniques (controller designed by pole placement with sensitivity function shaping and by mixed sensitivity H_∞ control) and classical PI controller, the following closed loop sensitivity functions are identified. Open loop identification method ELS (Extended Least Squares, details in [Landau & Zito, 2006]) has been used:

- output sensitivity functions ($\mathbf{S_o}$) based on experimental data of reference voltage (v_{ref}) and error voltage (v_e);

- complementary sensitivity functions ($\mathbf{T}$) based on experimental data of reference voltage (v_{ref}) and measured output voltage (v_y);

- input sensitivity functions ($\mathbf{KS_o}$) based on experimental data of reference voltage (v_{ref}) and system input voltage (v_1).

Output sensitivity function

Fig. 4.6 shows the closed loop output sensitivity function ($S_o(z^{-1})$) with different controllers. This sensitivity function shows the relationship between the disturbance of surface variations (z_S) and the tunneling current (i_t) as mentioned in the desired performance constraints (section 3.4) and also it shows the influence of noise (n) on the measured signal (v_y). According to the desired performance constraints, ($S_o(z^{-1})$) must be $|S_o| \leq -27.2 \ dB, 0 \leq \omega \leq \omega_M$ in order to achieve desired measurement accuracy of tunneling current and also $\|S_o\|_\infty \leq 6 \ dB, \forall \omega$ in order to achieve good robustness (see Table 3.2). A much stronger attenuation at low frequencies can be observed with

the proposed control techniques than with conventional PI controller, which was evident with the simulation results as well, where less variations were observed with proposed control techniques than with conventional PI control technique in the presence of surface variations (see Sections 3.5.3 and 3.6.3). For the comparison between the two proposed control techniques, a much stronger attenuation for large band of frequencies can be noticed with the proposed mixed sensitivity H_∞ control than with the controller designed by pole placement with sensitivity function shaping. This result in a better attenuation of external environmental disturbance, in order to achieve less fluctuations in the tunneling current (i_t). From the robustness point of view, the desired constraint is almost fulfilled with all the controllers.
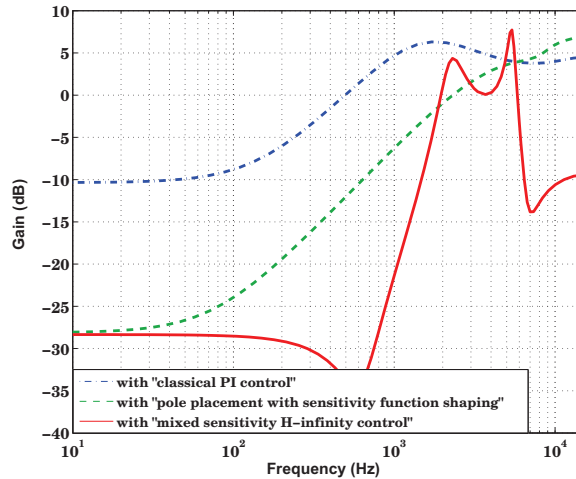
Figure 4.6: Experimentally identified closed loop output sensitivity functions ($\mathbf{S_o}$).

Complementary sensitivity function

Fig. 4.7 shows the closed loop complementary sensitivity function ($T(z^{-1})$) with different controllers, corresponding to the relationship between the measurement noise (n) and the tunneling current (i_t) as mentioned in Section 3.4. Measurement noise (n) is considered as a high frequency disturbance and according to the constraint of desired measurement accuracy of tunneling current, ($T(z^{-1})$) must be $|T| < \left|\frac{1}{G_n}\right|, \omega > \omega_M$ and also $\|T\|_\infty \leq 3.5\ dB, \forall \omega$ in order to achieve good robustness. It can be observed that all controllers

attenuate well measurement noise (n), while the proposed mixed sensitivity H$_\infty$ control even provides a larger closed loop bandwidth, compared to the conventional PI control and the pole placement controller.
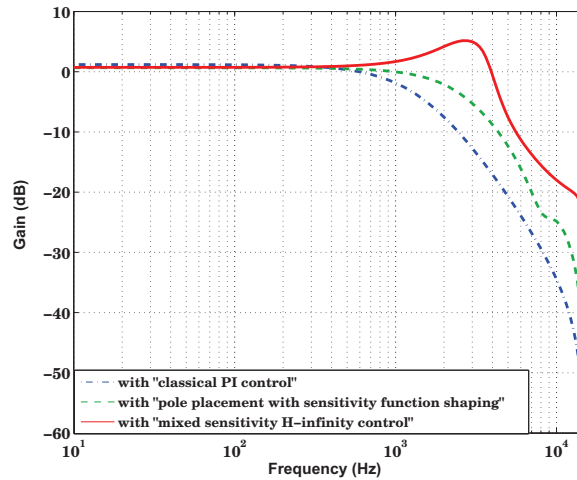
Figure 4.7: Experimentally identified closed loop complementary sensitivity functions (**T**).

Input sensitivity function

Fig. 4.8 shows the closed loop input sensitivity function ($KS_o(z^{-1})$) with all controllers. As mentioned in previous chapter, the constraints to avoid actuator saturations $\|KS_o\|_\infty \leq 20\ dB, \forall \omega$ and to limit the noise (n) influence on the system input (v_1) $|KS_o| < 0\ dB, \omega > \omega_M$ are fully met with classical PI controller and the proposed controllers.

Based on above experimentally identified closed loop sensitivity function, we can remark that stronger attenuation of external disturbances for a large band of frequencies is achieved with the prosed H$_\infty$ control, even it provides a larger closed loop bandwidth as compared to the other control techniques. Now, these results need to be verified with the time domain experimental results which are presented in the next section.
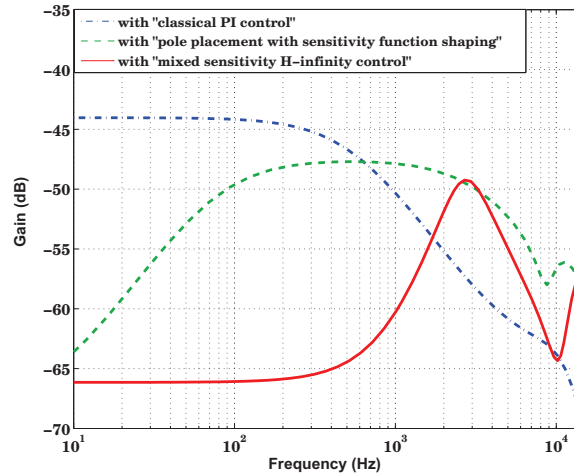
Figure 4.8: Experimentally identified closed loop input sensitivity functions ($\mathbf{KS_o}$).

4.4 Tunneling Current with Conventional PI Control Technique

In this section, the time domain experimental results with conventional PI control technique are presented for the considered system of tunneling current. After arriving in the tunneling region (distance (d) between tip apex and sample surface less than $1 \times 10^{-9}\ m$) with the strategy proposed earlier, different desired values of tunneling current (i_t) are given and the resulting variations in the measured tunneling current with conventional PI control technique are examined.

4.4.1 Steady state current control

Fig. 4.9 shows the measured tunneling current (i_t) with conventional PI control. Different desired values of tunneling current ($0.25\ nA$, $0.5\ nA$, $0.75\ nA$) are given for the control system and the measured tunneling currents are examined. The standard deviations of measured tunneling currents are $24.3\ pA$, $36.1\ pA$ and $50.1\ pA$ corresponding to the desired values of tunneling current $0.25\ nA$, $0.5\ nA$, $0.75\ nA$ respectively. This result will help us for the comparison between proposed control techniques and the conventional control technique.
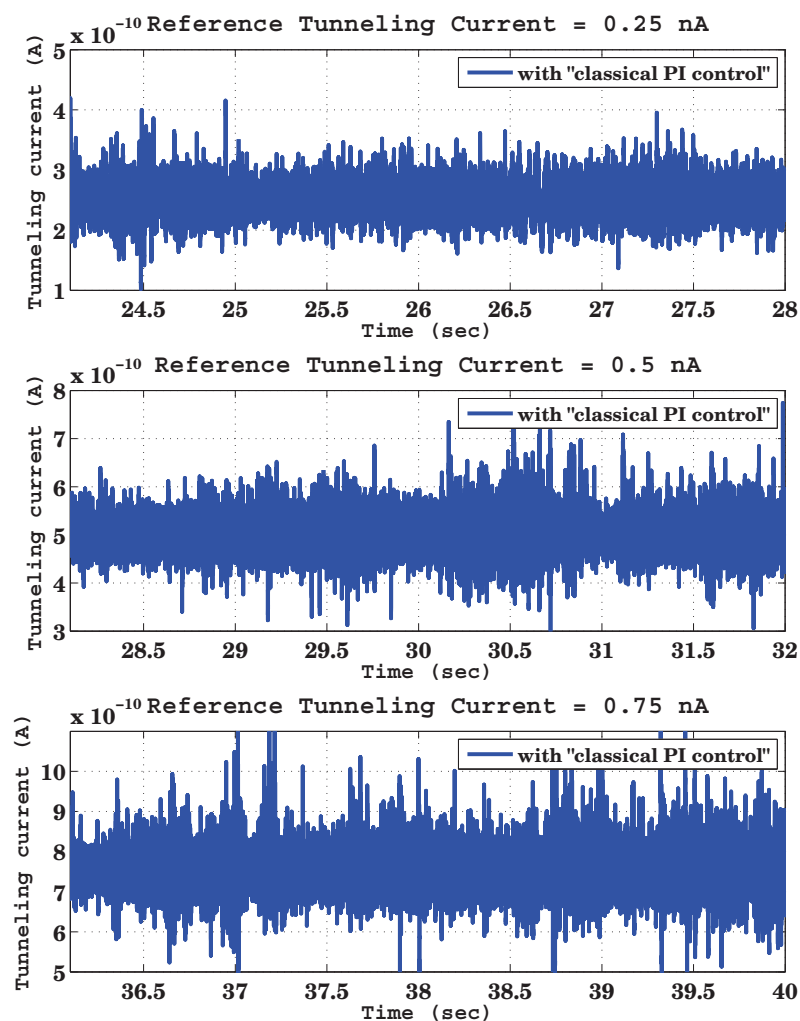
Figure 4.9: Experimental result with **classical PI control** with reference tunneling current of 0.25 nA, 0.5 nA and 0.75 nA.

4.4.2 Current reference tracking

Tunneling current (i_t) behavior was also observed with step variations of desired tunneling current. Again, after arriving in the tunneling region, a series of step variations of desired tunneling current is considered. Fig. 4.10 shows the measured tunneling current (i_t) variations with conventional PI controller together with the corresponding piezo control signal. Again, this result will be used for comparison between conventional and proposed control techniques.
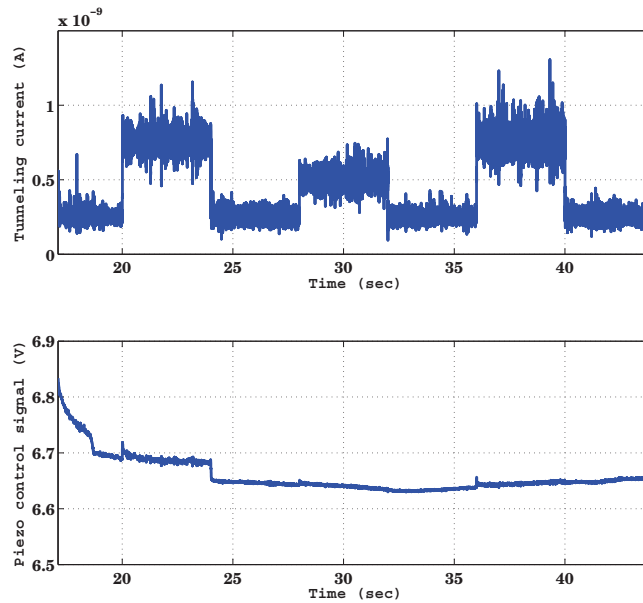
Figure 4.10: Experimental result with **classical PI control** having step variations of desired tunneling current.

4.5 Tunneling Current with Modern Control Techniques

In this section, the time domain experimental results with comparison between conventional and proposed control techniques are presented for the considered system of tunneling current. Here, we will observe the resulting variations in the measured tunneling current with the proposed controller designed by pole placement with sensitivity function shaping and by mixed sensitivity H_∞ control. Also the comparison with conventional PI control results as presented in previous section, is here illustrated.

4.5.1 Steady state current control

Reference tunneling current of $0.25 \ nA$

Fig. 4.11 shows the measured tunneling current (i_t) with the proposed control techniques (controller designed by pole placement with sensitivity function shaping and mixed sen-

sitivity H_∞ control) and with conventional PI controller. The desired tunneling current value was $0.25\ nA$. It can be observed that tunneling current (i_t) variations are indeed
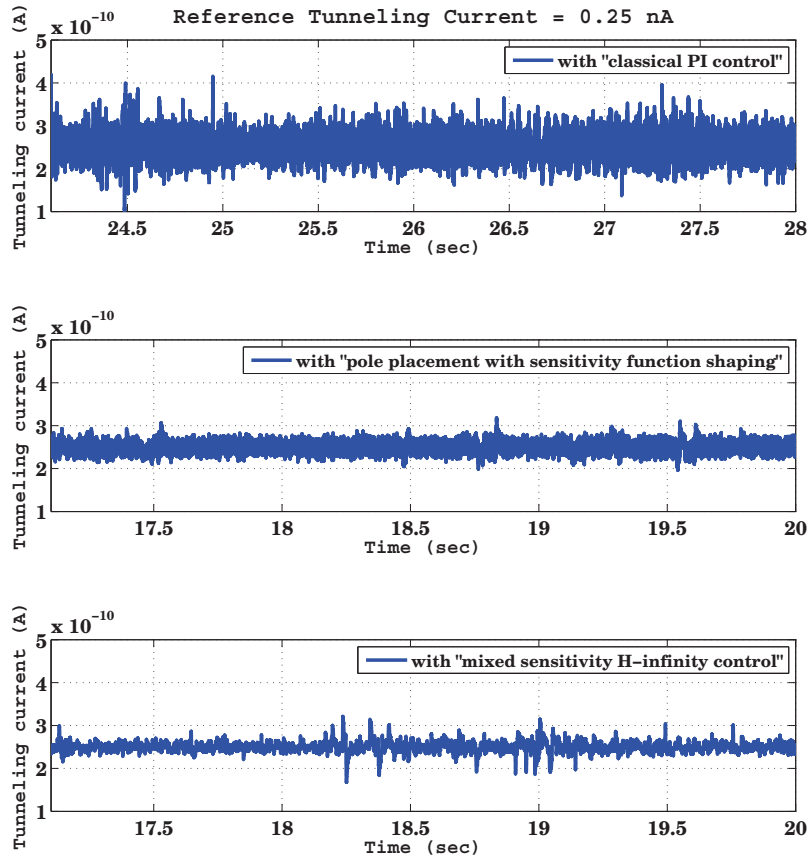
Figure 4.11: Comparison of experimental results with reference tunneling current of $0.25\ nA$.

lower with the proposed control techniques than with the conventional PI controller. The standard deviation of measured tunneling current is $10.8\ pA$ with the proposed controller designed by pole placement with sensitivity function shaping and $12.7\ pA$ with the mixed sensitivity H_∞ control (the standard deviation with PI controller was $24.3\ pA$). The tunneling current variations with proposed control techniques remain within more or less $\pm 10\%$ variations of desired value which is in good accordance wit simulation results.
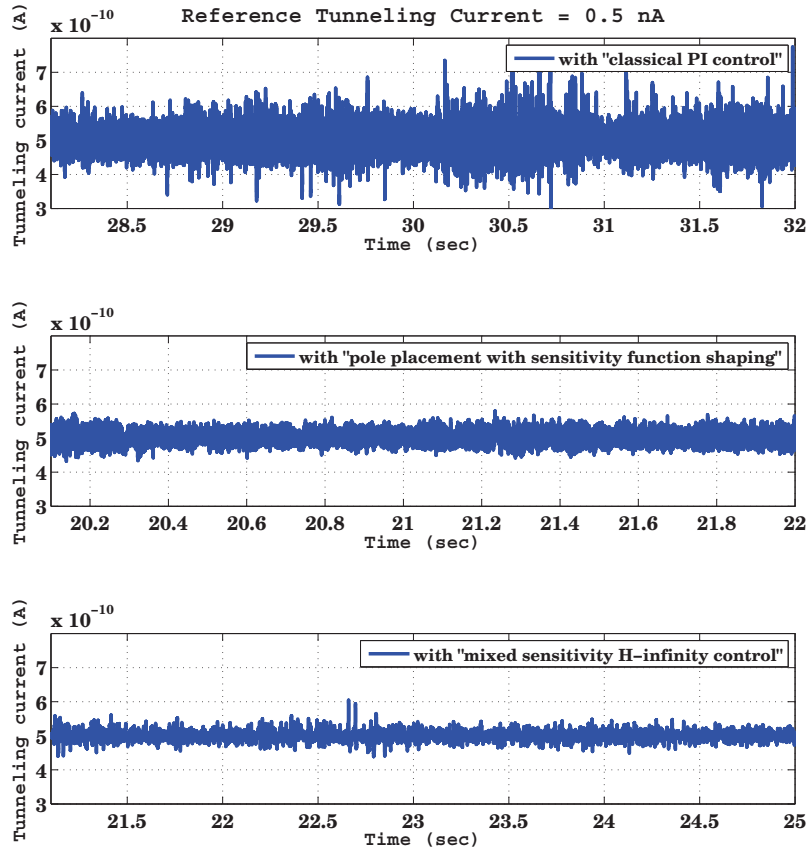
Figure 4.12: Comparison of experimental results with reference tunneling current of 0.5 nA.

Reference tunneling current of 0.5 nA

Next, the tunneling current (i_t) variations are examined with a slightly larger desired value which requires to move the tip precisely closer to the sample surface. Fig. 4.12 shows the behavior of tunneling current (i_t) with the proposed and with conventional PI controller when the desired value of tunneling current was 0.5 nA. It can be observed again that the tunneling current (i_t) variations are lower with proposed controllers then with conventional PI controller. The standard deviation of measured tunneling current is 16.7 pA with the proposed controller designed by pole placement with sensitivity function shaping and 14.8 pA with the mixed sensitivity H_∞ control (the standard deviation with

PI controller was 36.1 pA). It can also be observed that with all controllers, the tunneling current (i_t) variations are a little larger than in the previous case. This can be explained by stronger mechanical noise.
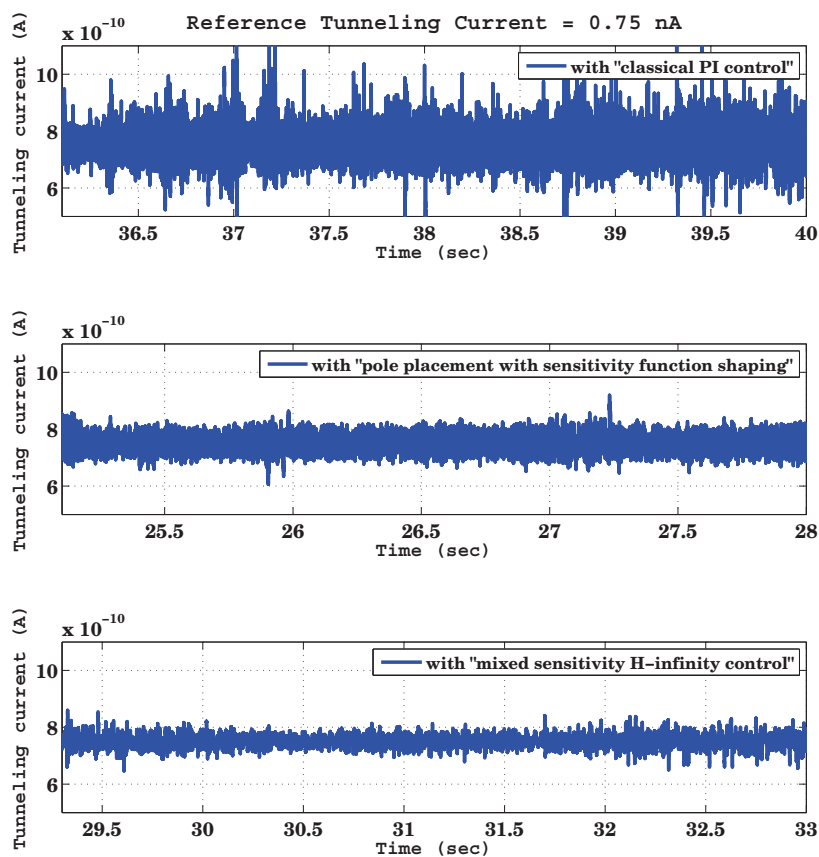
Figure 4.13: Comparison of experimental results with reference tunneling current of 0.75 nA.

Reference tunneling current of 0.75 nA

Again, the tunneling current (i_t) variations are examined with a more larger desired value of tunneling current (0.75 nA). Fig. 4.13 shows the behavior of tunneling current (i_t) with all the controllers. It can be observed again that the tunneling current (i_t) variations are lower with proposed controllers then with conventional PI controller. The standard deviation of measured tunneling current is 25.9 pA with the proposed controller

designed by pole placement with sensitivity function shaping and 22.1 pA with the mixed sensitivity H_∞ control (the standard deviation with PI controller was 50.1 pA).

As shown in these results, the tunneling current variations are indeed lower with the proposed control techniques than with the conventional PI control technique, which is in good accordance with simulation results and also with the identified closed loop sensitivity functions.

4.5.2 Current reference tracking

Tunneling current (i_t) behavior was observed in the presence of proposed controllers with step variations of desired tunneling current. Fig. 4.14 and Fig. 4.15 show the tunneling current (i_t) variations with proposed controller designed by pole placement and with mixed sensitivity H_∞ control respectively. It can be noticed very clearly that at each step of desired tunneling current, the tunneling current (i_t) variations with proposed controllers is lower than the ones with the conventional PI controller. The step variations of tunneling current (i_t) with conventional PI controller was already shown in Fig. 4.10.

4.6 Discussion

In the previous section, we have observed the variations in the measured tunneling current with different control techniques and also we have experimentally identified the closed loop sensitivity functions which give us much information about desired performances in terms of disturbance rejection, robustness and closed loop bandwidth. In this section, we will further analyse the above achieved results which will help us finally to present a conclusion in the end of this Chapter.

Firstly, the power spectral densities of the measured tunneling current (i_t) are analyzed (Fig. 4.16 to Fig. 4.18) with proposed and conventional PI controllers at different desired values of tunneling current. The much stronger attenuation of disturbances with
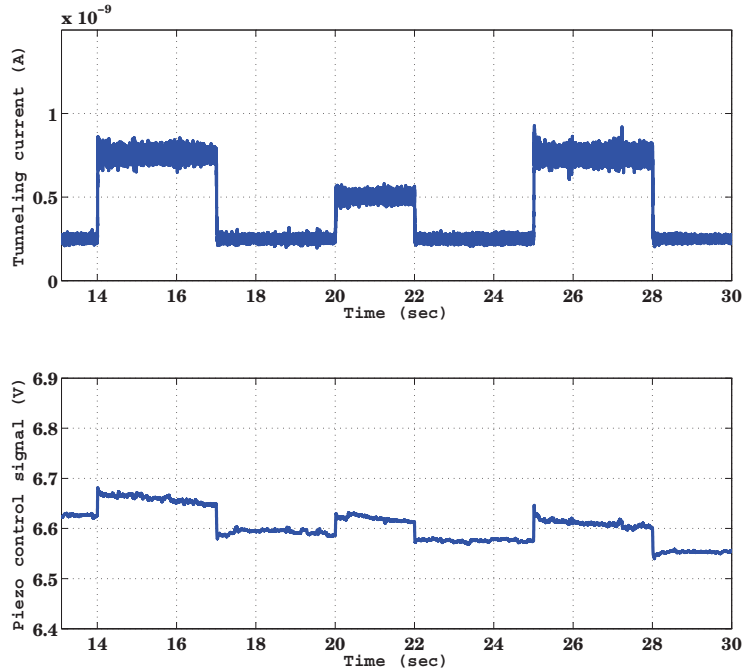
Figure 4.14: Experimental result with **controller designed by pole placement with sensitivity function shaping** having step variations of desired tunneling current

the both proposed controllers than with conventional PI controller is indeed confirmed at all frequencies, particularly at low frequencies.

The power spectral densities of the measured tunneling current (i_t) with both proposed controllers can also be compared from Fig. 4.16 to Fig. 4.18. At all desired values of tunneling current (0.25 nA, 0.5 nA, 0.75 nA), a slightly stronger attenuation of disturbances at higher frequencies can be observed with the mixed sensitivity H$_\infty$ control than with controller designed by pole placement with sensitivity function shaping e.g. around -5 dB more attenuation is achieved at high frequencies with the mixed mixed sensitivity H$_\infty$ control than with pole placement with sensitivity function shaping control. Although, at lower frequencies, there is no much difference between the level of attenuation of disturbances. It can also be noticed that some peaks appeared at certain frequencies with all the controllers, e.g. at 5 kHz a small peak is observed with mixed sensitivity H$_\infty$ control at all desired values of tunneling current. This peak can also be noticed in the output sensitivity function ($S_o(z^{-1})$) with H$_\infty$ control (Fig. 4.6) as
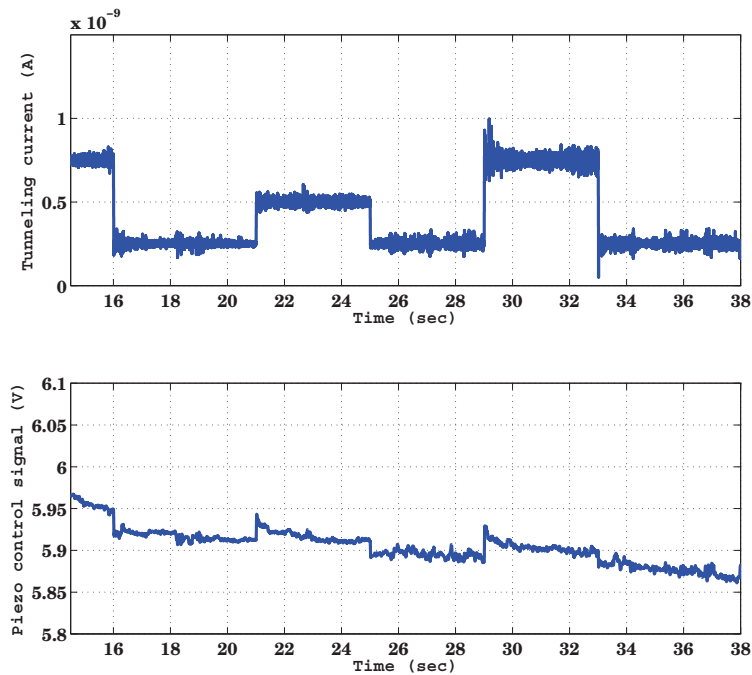
Figure 4.15: Experimental result with **mixed sensitivity H$_\infty$ control** having step variations of desired tunneling current.

well. Similarly, a peak is noticed with all the controllers at very low frequency, around 350 Hz. The origin of this peak seems to be experimental as it's amplitude varies in different tests, but the exact reason is not yet determined.

The standard deviations of the measured tunneling current with different control techniques are compared in Table. 4.2. These standard deviations of tunneling current show much improvement with the proposed control techniques than with conventional PI control technique. It can be noticed that much better measurement precision is achieved with the proposed H$_\infty$ control than with the controller designed by pole placement with sensitivity function shaping.

Finally, the robust stability and robust performance conditions (section 3.4) in the presence of the proposed controllers are verified with experimentally identified closed loop sensitivity functions. Fig. 4.19 and Fig. 4.20 show the robust stability and robust performance tests respectively. It can be noticed that the condition for robust stability has been verified with both proposed controllers, *i.e.* the closed-loop system remains
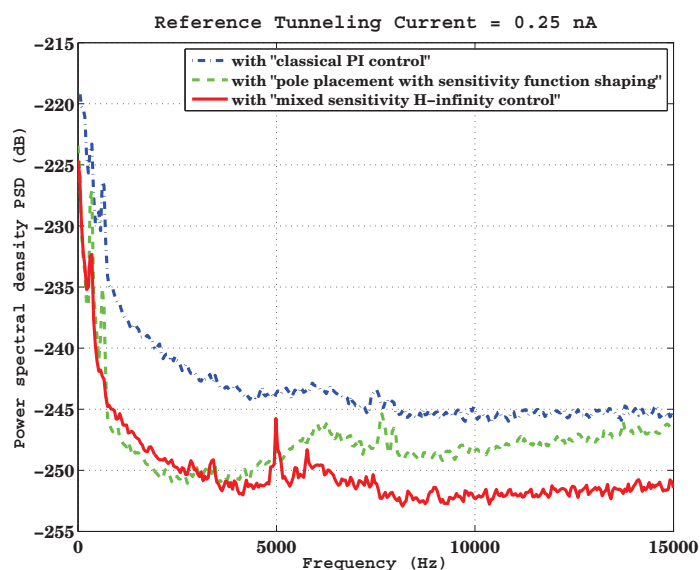
Figure 4.16: Comparison of power spectral densities with reference tunneling current of 0.25 nA.
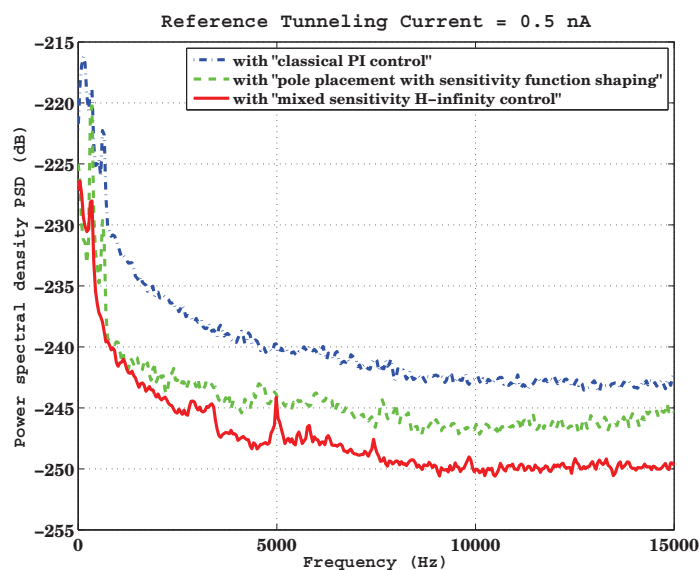
Figure 4.17: Comparison of power spectral densities with reference tunneling current of 0.5 nA.

stable for all perturbed plants around the nominal model up to the chosen worst-case model uncertainty (uncertainty model with parametric variations is already discussed in section 3.3.5). Although, the condition for robust performance has not been fully satisfied with the proposed H_∞ control, precisely at higher frequencies between 2 kHz
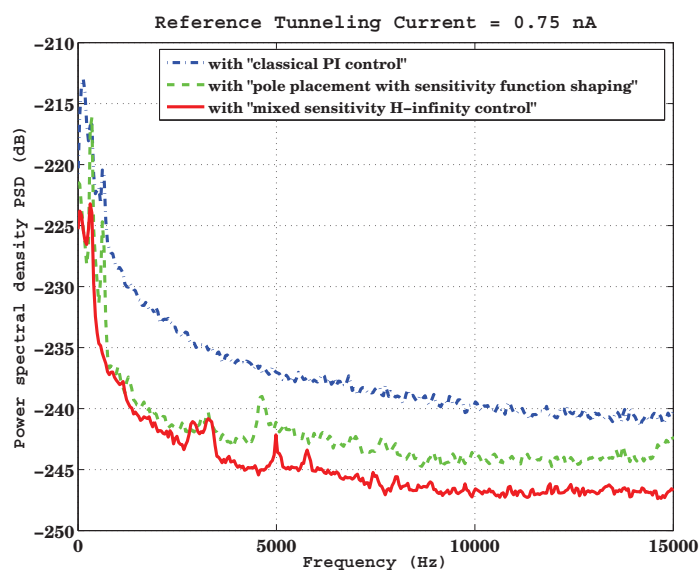
Figure 4.18: Comparison of power spectral densities with reference tunneling current of 0.75 nA.

Table 4.2: Comparison of standard deviations of tunneling current with different control techniques

Reference current	PI control	Sensitivity functions shaping	H_∞ control
0.25 nA	24.3 pA	10.8 pA	12.7 pA
0.5 nA	36.1 pA	16.7 pA	14.8 pA
0.75 nA	50.1 pA	25.9 pA	22.1 pA

and 3 kHz. The reason is the high positive gain (peaks) of output sensitivity function and also the complementary sensitivity function within this frequency range (see Fig. 4.6 and Fig. 4.7) with mixed sensitivity H_∞ control.

4.7 Conclusion

In this chapter, an experimental setup developed in Gipsa-lab, Grenoble by control group in order to analyze the influence of different control techniques on tunneling current
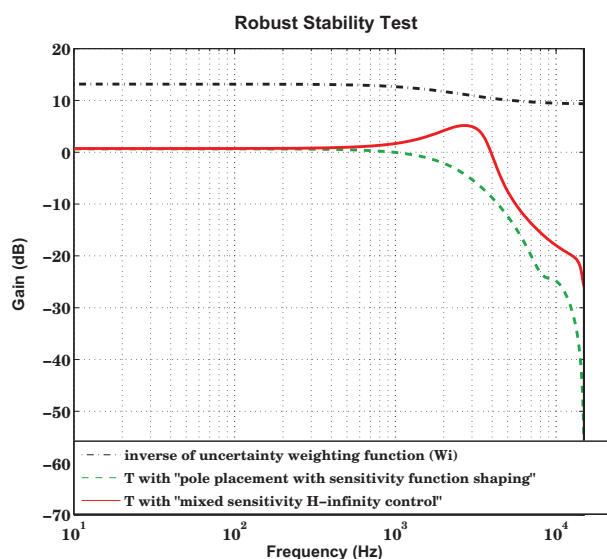
Figure 4.19: Comparison of robust stability test: $|\mathbf{T}| < \frac{1}{|W_I|}, \forall \omega$
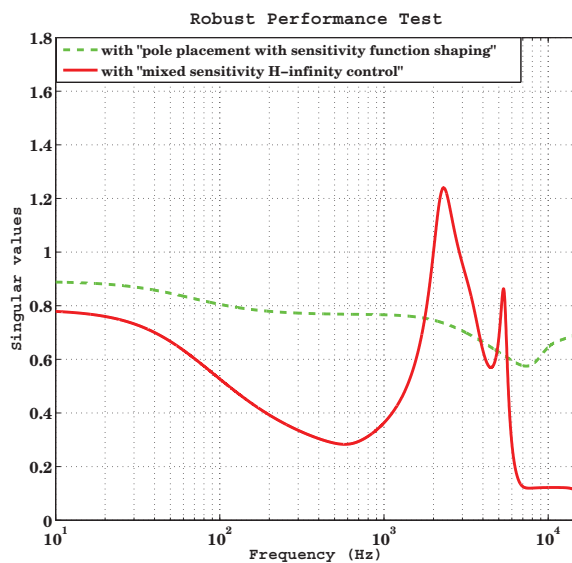
Figure 4.20: Comparison of robust performance test: $\max_\omega(\mid W_P S_o \mid + \mid W_I T \mid) < 1, \forall \omega$

measurement has been presented. Hardware details, experimental constraints and the strategy in order to achieve the tunneling current have been briefly presented.

In the second section, system identification has been performed and the identified model of the system has been found very similar to the theoretical one, in terms of overall gain and the bandwidth of the open loop system (plant).

In the third section, the closed loop sensitivity functions have been identified experimentally with conventional PI control and the proposed control techniques (Chapter 3) for performance analysis of the tunneling current measurement system. Stronger attenuation of external disturbances for a large band of frequencies has been observed with the proposed H_∞ control, even it provides a larger closed loop bandwidth, as compared with the proposed controller designed by pole placement with sensitivity function shaping and the conventional PI control.

In the fourth section, time domain experimental results have been presented for tunneling current measurement system for a comparison between different control techniques. It has been observed that the tunneling current variations are indeed lower with the proposed control techniques, particularly with mixed sensitivity H_∞ control, than with conventional PI control technique.

Finally, a comparison between proposed and conventional control techniques have been performed with power spectral densities and the standard deviations of the measured tunneling current, which are indeed in good accordance with the frequency and time domain results discussed earlier.

TOWARDS MIMO ANALYSIS AND CONTROL

This chapter is devoted to the analysis of the tunneling current measurement system while scanning the surface in the horizontal x-direction. Scanning for long range and large duration induces the problem of dynamic nonlinearities (hysteresis and creep respectively) of piezoelectric actuator. Cross-coupling problem of piezoelectric actuator is also an important issue for nanopositioning. Measurement precision of the tunneling current can be adversely affected by the coupling-caused positioning error in the vertical z-direction, while scanning the surface. In this chapter, a MIMO controller is analyzed in simulation in order to obtain the better performances for the considered system of tunneling current, in the presence of coupling-caused positioning error.

The problem of coupling-caused positioning error with some recent research work from control point of view is presented in Section 5.1.

A dynamic modeling of the overall MIMO system having horizontal, vertical and cross coupling dynamics is performed in Section 5.2.

The problem of dynamic nonlinearities of piezoelectric actuator is highlighted and analyzed (in open-loop and also in closed-loop) in Section 5.3, while scanning for long range in horizontal x-direction over the experimental platform of Gipsa-lab.

In the first part of the Section 5.4, the measurement precision of the considered system of tunneling current in vertical z-direction is analyzed in simulations while scanning in the horizontal x-direction, in the presence of coupling dynamics. In the second part, LQR control for overall MIMO system is analyzed for the considered system.

Finally, Section 5.5 draws some conclusions.

5.1 Introduction

The cross-coupling problem that arises during high-speed nano-precision positioning using piezoelectric scanners is highlighted in Chapter 2. This problem can adversely influence the high measurement precision of the tunneling current in vertical z-direction. Coupling-caused positioning errors in the vertical z-direction can arise due to the scanning movement in the x and y directions. However, as pointed out in different recent research articles [Song et al., 2005], [Sebastian & Salapaka, 2005], [Butterworth et al., 2009], the effect of scanning movement in the horizontal x-direction on the vertical z-direction is more significant because the scan frequency in the x-direction is higher than the scan frequency in the y-direction (all three x, y and z directions can be seen in Fig. 2.3). Coupling-caused positioning error becomes more significant while scanning at high speed for long range. Long range scanning for some large duration in horizontal x-direction also induces the problem of dynamic nonlinearities (hysteresis and creep) of piezoelectric actuator.

Some research work from control point of view in order to reduce the coupling-caused positioning errors is already mentioned in Chapter 2, *e.g.* [Tien et al., 2004], [Song et al., 2005], [Wu et al., 2009], [Shi et al., 2009]. However, some recent papers [Pao et al., 2007], [Mahmood & Moheimani, 2009], [Butterworth et al., 2009] have pointed out the interest to analyze MIMO controllers in order to analyze the performances of the overall positioning system (the x-y-z directions positioning). In this chapter, a MIMO controller is analyzed for tunneling current measurement system, in the presence of coupling dynamics (proposed from the experimental results presented in [Tien et al., 2004]).

5.2 System Modeling

The purpose of this section is to model the considered MIMO system. The complete open loop system which will be here considered is presented in Fig. 5.1, where the horizontal
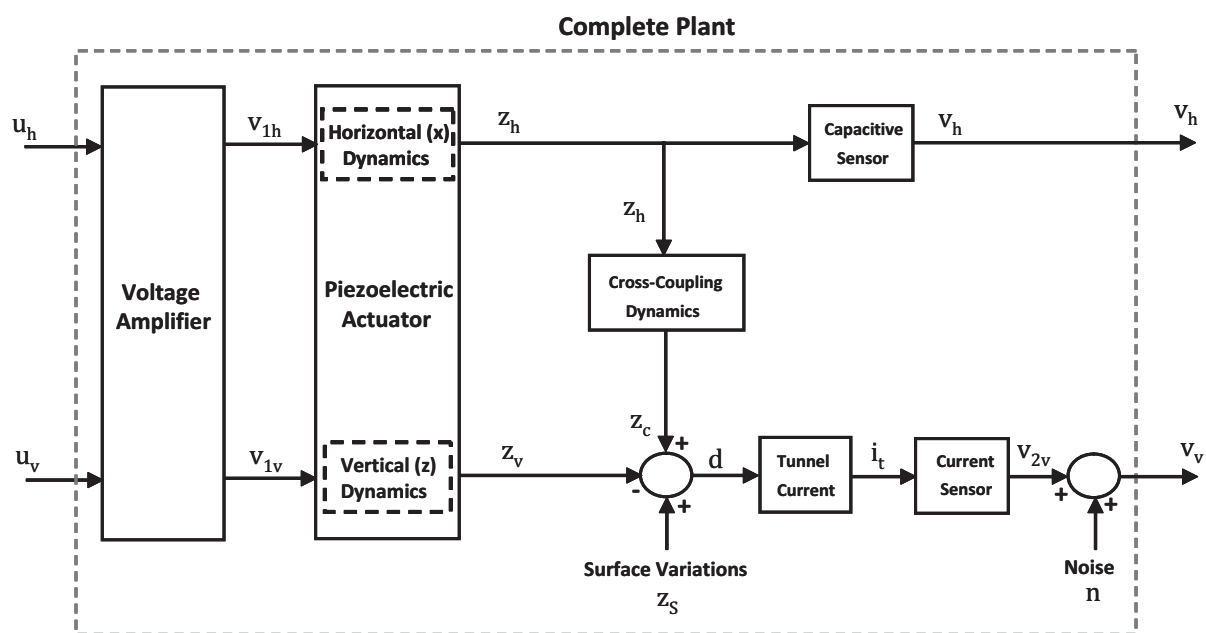
Complete Plant

Figure 5.1: Complete MIMO plant having horizontal, vertical and cross-coupling dynamics

system consists of:

- the voltage amplifier;

- the horizontal x-piezoelectric actuator;

- the capacitive sensor

and the vertical system consists of:

- the voltage amplifier;

- the vertical z-piezoelectric actuator;

- the physical law which gives the relationship between tunneling current and the distance between tip and sample surface;

- the current sensor (CVC).

Here, in order to obtain a complete MIMO plant model, a simple linear model of horizontal and vertical systems with coupling dynamics are considered.

5.2.1 Horizontal dynamics

For horizontal positioning system, the dynamics of the piezoelectric actuator (bandwidth 630 Hz) is considered as a second order system, while the dynamics of voltage amplifier (bandwidth 4 kHz) and of the capacitive sensor (bandwidth 8.5 kHz) are considered as constant gains (closed-loop dominant poles are placed at 200 Hz). So, the output of the voltage amplifier (v_{1h}) is:

$$v_{1h}(t) = G_v \cdot u_h(t) \tag{5.2.1}$$

where G_v is the gain and u_h is the input voltage of the voltage amplifier.

The dynamics of the piezoelectric actuator for horizontal x-direction has been modeled as:

$$\begin{cases} \dot{x}_1(t) &=& -2\zeta_{ah}\omega_{ah} \cdot x_1(t) - \omega_{ah}^2 \cdot x_2(t) + v_{1h}(t) \\ \dot{x}_2(t) &=& x_1(t) \\ z_h(t) &=& G_{ah}\omega_{ah}^2 \cdot x_2(t) \end{cases} \tag{5.2.2}$$

where v_{1h} and z_h are input voltage and output displacement of the piezoelectric actuator respectively, ζ_{ah} is the damping, ω_{ah} the bandwidth and G_{ah} the gain of the piezoelectric actuator.

The output voltage (v_h) of the capacitive sensor is:

$$v_h(t) = G_c \cdot z_h(t) \tag{5.2.3}$$

where G_c is the gain and z_h is the input of the capacitive sensor.

So, the overall dynamics of the horizontal system is:

$$\begin{cases} \dot{x}_1(t) &=& -2\zeta_{ah}\omega_{ah} \cdot x_1(t) - \omega_{ah}^2 \cdot x_2(t) + G_v \cdot u_h(t) \\ \dot{x}_2(t) &=& x_1(t) \\ v_h(t) &=& G_c G_{ah}\omega_{ah}^2 \cdot x_2(t) \end{cases} \tag{5.2.4}$$

5.2.2 Cross-coupling dynamics

First of all, the displacement of the piezoelectric actuator z_h in horizontal direction is retrieved by using the gain of the capacitive sensor. As the bandwidth of the capacitive

sensor (8.5 kHz) is very large compared to the bandwidth of the piezoelectric actuator (630 Hz) in horizontal direction, we can assume that: $\hat{z}_h = z_h$. Then, the retrieved displacement of the piezoelectric actuator $\hat{z}_h$ in horizontal direction is:

$$\hat{z}_h(t) = (1/G_c) \cdot v_h(t) \tag{5.2.5}$$

where G_c is the gain of the capacitive sensor.

As mentioned in the previous sections, the scanning movement of the tip in the horizontal x-direction induces a positioning error in the vertical z-direction and this coupling-caused positioning error becomes more significant with high scan speed and also with large scanning range. A high pass filter is then proposed to model this crosscoupling effect and the gain of the filter dynamics will define the maximum positioning error (3% of the scanning displacement in horizontal x-direction at high scan speed of 100 Hz, taken from [Tien et al., 2004]), which will act as a disturbance for the vertical system. The cross-coupling dynamics can thus be modeled as:

$$\begin{cases} \dot{x}_3(t) &= -\omega_{fc} \cdot x_3(t) + \hat{z}_h(t) \\ z_c(t) &= -G_{fc}\omega_{fc} \cdot x_3(t) + G_{fc} \cdot \hat{z}_h(t) \end{cases} \tag{5.2.6}$$

where z_c is the output (positioning error) of the coupling dynamics, ω_{fc} is the bandwidth (scan speed for maximum positioning error) and G_{fc} the gain (maximum positioning error).

The overall cross-coupling dynamics between the output voltage of the capacitive sensor (v_h) and the positioning error (z_e) is:

$$\begin{cases} \dot{x}_3(t) &= -\omega_{fc} \cdot x_3(t) + (1/G_c) \cdot v_h(t) \\ z_c(t) &= -G_{fc}\omega_{fc} \cdot x_3(t) + (G_{fc}/G_c) \cdot v_h(t) \end{cases} \tag{5.2.7}$$

5.2.3 Vertical dynamics

The modeling of the vertical system (nonlinear model) and then linearization of the static exponential nonlinearity (as tunneling current depends exponentially on the distance between tip and sample surface) in order to achieve the linearized model, is already discussed in Chapter 3. A simple linear model (dynamics of the voltage amplifier) of

uncoupled vertical system was considered in Chapter 3 for the purpose of synthesis of the controller which was later validated in Chapter 4 with identification results performed with experimental data.

For the vertical positioning system, the voltage amplifier has been modeled as:

$$\begin{cases} \dot{x}_4(t) &= -\omega_{vv} \cdot x_4(t) + u_v(t) \\ v_{1v}(t) &= G_v \omega_{vv} \cdot x_4(t) \end{cases} \tag{5.2.8}$$

where u_v and v_{1v} are input and output voltages of the voltage amplifier respectively, ω_{vv} is the bandwidth and G_v the gain of the voltage amplifier.

The output displacement (z_v) of the piezoelectric actuator is:

$$z_v(t) = G_{av} \cdot v_{1v}(t)$$

where G_{av} is the gain and v_{1v} the input voltage of the piezoelectric actuator. As v_{1v} is the output voltage of the voltage amplifier, the output displacement (z_v) of the piezoelectric actuator can be expressed as:

$$z_v(t) = G_{av} G_v \omega_{vv} \cdot x_4(t) \tag{5.2.9}$$

Now, the vertical distance (d) between tip and sample surface has been obtained as (see Fig. 5.1):

$$d(t) = z_s(t) + z_c(t) - z_v(t) \tag{5.2.10}$$

where z_s is the unknown surface variations and z_c the positioning error because of the coupling dynamics. Both will act as disturbances for the vertical system. From Eq. (5.2.7) and Eq. (5.2.9), this vertical distance (d) can be expressed as:

$$d(t) = z_s(t) - G_{fc}\omega_{fc} \cdot x_3(t) + (G_{fc}/G_c) \cdot v_h(t) - G_{av}G_v\omega_{vv} \cdot x_4(t) \tag{5.2.11}$$

The linearization of tunneling current i_t with respect to the distance (d) between tip and sample surface is discussed in Chapter 3 (Eq. (3.3.6)), so the linearized tunneling current is expressed as:

$$i_t(t) = ki_{eq} \cdot d(t) \tag{5.2.12}$$

where k is a constant term and i_{eq} the tunneling current at operating point.

The output voltage v_{2v} of current sensor (CVC) is taken as:

$$v_{2v}(t) = G_{cv} \cdot i_t(t)$$

where G_{cv} is the gain of the current sensor. This output voltage (v_{2v}) can be expressed as:

$$v_{2v}(t) = G_{cv}ki_{eq} \cdot d(t) \tag{5.2.13}$$

The measured output voltage of the vertical system is expressed as:

$$v_v(t) = v_{2v} + n(t)$$

where n is the measurement noise. From Eq. (5.2.13), the overall vertical output voltage (v_v) is represented as:

$$v_v(t) = G_{cv}ki_{eq} \cdot d(t) + n(t) \tag{5.2.14}$$

where the vertical distance (d) is given by Eq. (5.2.11).

So, the overall dynamics of the vertical system is:

$$\begin{cases} \dot{x}_4(t) &= -\omega_{vv} \cdot x_4(t) + u_v(t) \\ v_v(t) &= G_{cv}ki_{eq} \cdot (z_s(t) - G_{fc}\omega_{fc} \cdot x_3(t) \\ &\quad + (G_{fc}/G_c) \cdot v_h(t) - G_{av}G_v\omega_{vv} \cdot x_4(t)) + n(t) \end{cases} \tag{5.2.15}$$

5.2.4   Global MIMO plant model

The complete MIMO plant model having two input voltages (u_h and u_v) and two output voltages (v_h and v_v) is:

$$\begin{cases} \dot{x}_1(t) &= -2\zeta_{ah}\omega_{ah} \cdot x_1(t) - \omega_{ah}^2 \cdot x_2(t) + G_v \cdot u_h(t) \\ \dot{x}_2(t) &= x_1(t) \\ \dot{x}_3(t) &= -\omega_{fc} \cdot x_3(t) + (1/G_c) \cdot v_h(t) \\ \dot{x}_4(t) &= -\omega_{vv} \cdot x_4(t) + u_v(t) \\ v_h(t) &= G_c G_{ah}\omega_{ah}^2 \cdot x_2(t) \\ v_v(t) &= G_{cv}ki_{eq} \cdot (z_s(t) - G_{fc}\omega_{fc} \cdot x_3(t) + (G_{fc}/G_c) \cdot v_h(t) - G_{av}G_v\omega_{vv} \cdot x_4(t)) + n(t) \end{cases} \tag{5.2.16}$$

5.3 Dynamic Nonlinearities for Horizontal Movement of Piezoelectric Actuator

5.3.1 Hysteresis

The piezoelectric actuator is driven by a fast triangular waveform in order to scan the sample surface in a raster (back and forth) pattern. The amplitude and frequency of this waveform defines the scanning range and speed respectively. Scanning for long range introduces the phenomenon of *hysteresis*, which has been observed for the horizontal motion of piezoelectric actuator in x-direction over the experimental platform of Gipsa-lab.

Fig. 5.2 and Fig. 5.3 shows the hysteresis phenomenon dependance over the amplitude of the input voltage (scanning range) of piezoelectric actuator. It can be observed that at small amplitude of input voltage (0.1 V) with horizontal displacement of piezoelectric actuator of around 300 nm, the hysteresis phenomenon is almost negligible. This result justifies our approximation of neglecting the hysteresis phenomenon for the vertical movement (in z-direction for tunneling current measurement) since the vertical displacement was very small (less than 1 nm). Fig. 5.4 shows the hysteresis phenomenon at different frequencies of input voltage for the horizontal movement of piezoelectric actuator. It can be observed that the hysteresis loop remains almost similar at all frequencies of input signal. Finally, an open loop reference tracking for the horizontal movement of the piezoelectric actuator and the corresponding hysteresis loop are presented in Fig. 5.5.

A number of hysteresis models and a lot of research has already been done to compensate the hysteresis phenomenon. Some corresponding details have already been highlighted very briefly in Chapter 2. In next sections, we will just rely again on a direct RS-type design.
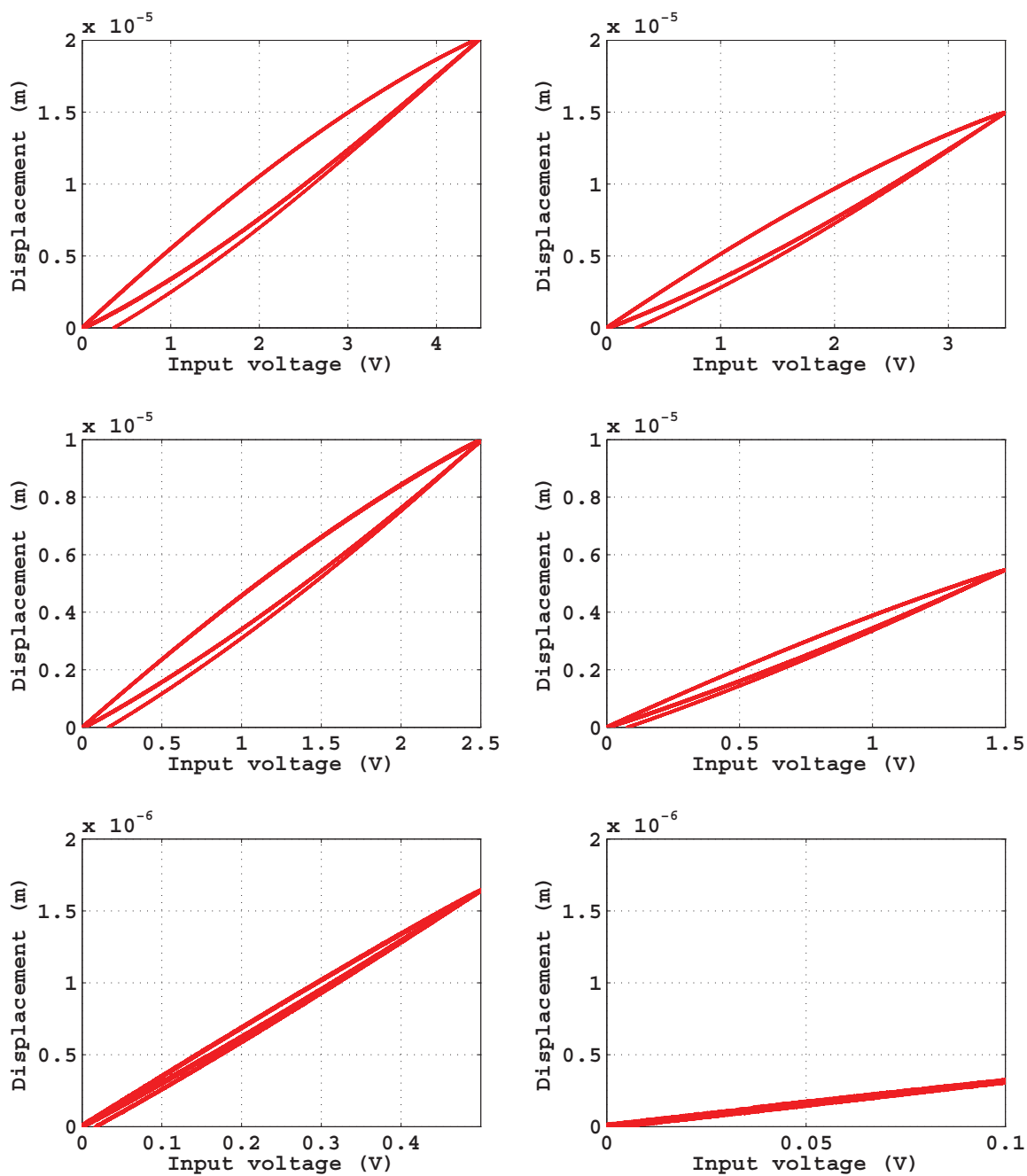
Figure 5.2: The *hysteresis* phenomenon observed over the experimental platform at different input voltage amplitudes for the horizontal movement of the piezoelectric actuator.
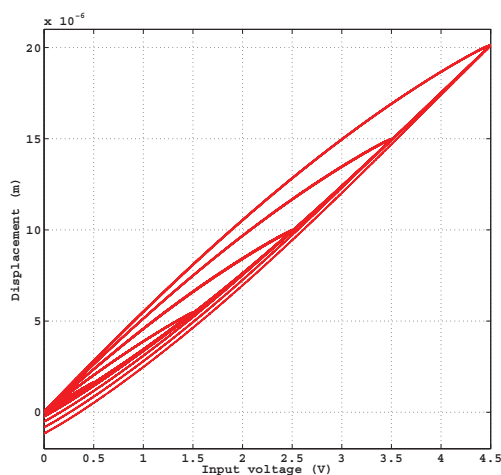
Figure 5.3: The *hysteresis* phenomenon observed over the experimental platform for the horizontal movement of the piezoelectric actuator.
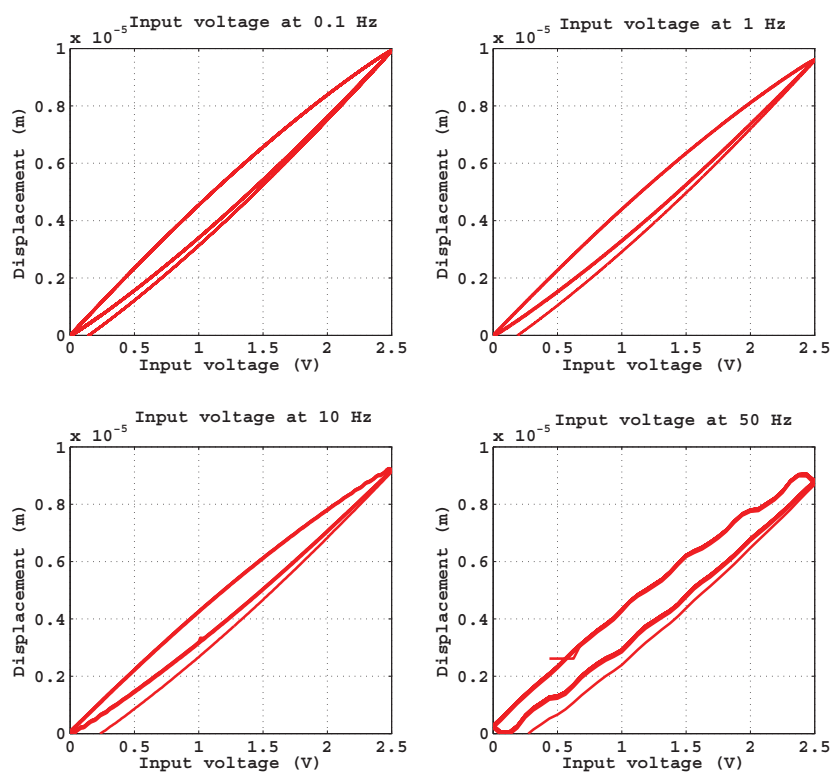
Figure 5.4: The *hysteresis* phenomenon observed over the experimental platform at different rates of input voltage for the horizontal movement of the piezoelectric actuator.
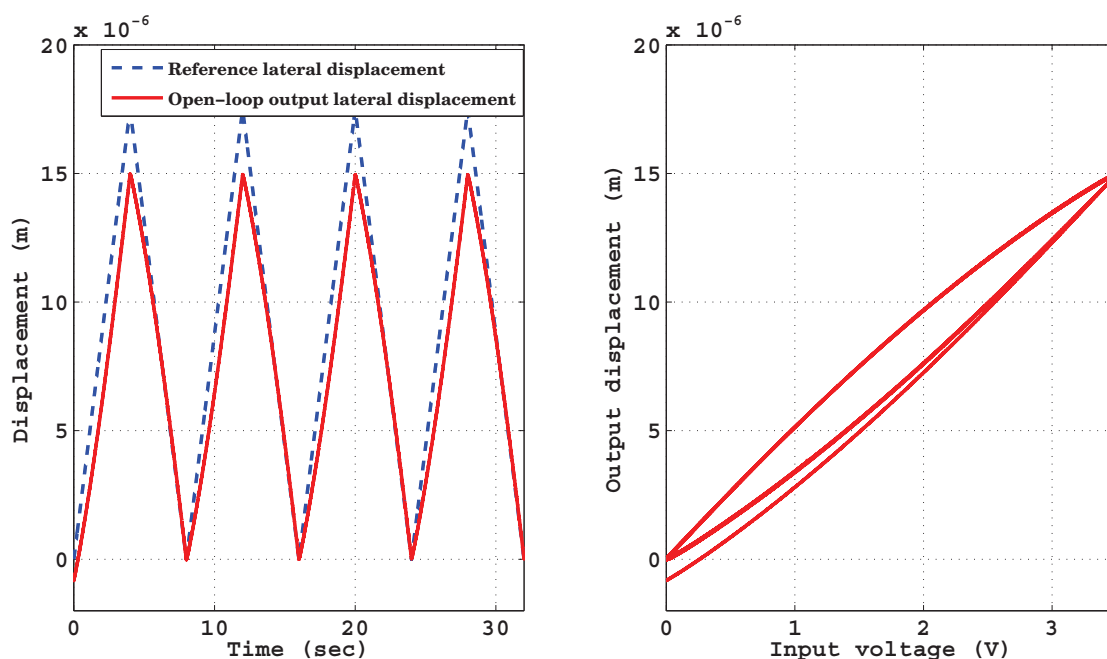
Figure 5.5: Experimental result of open-loop reference tracking and observed *hysteresis* loop for the horizontal movement of the piezoelectric actuator.
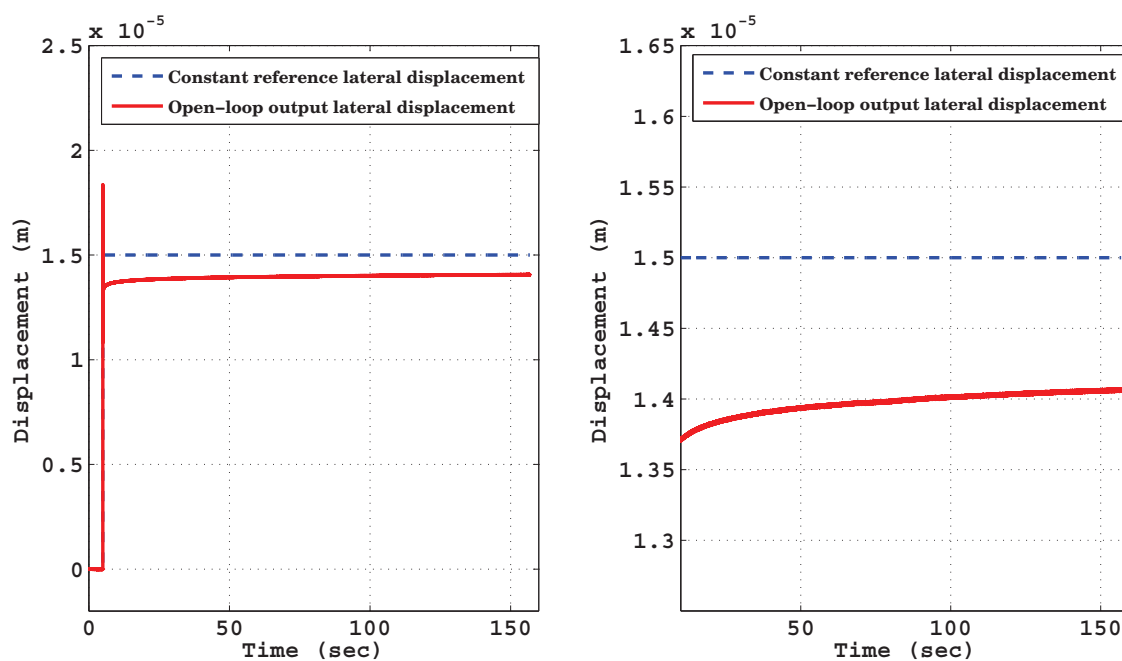
Figure 5.6: Experimental result of open-loop step response for the horizontal movement of the piezoelectric actuator with *creep* phenomenon.

5.3.2   Creep

The drift of the displacement of piezoelectric actuator for a constant reference voltage is another undesirable phenomenon, commonly known as creep. This phenomenon has been observed (Fig. 5.6) for the horizontal motion of piezoelectric actuator in x-direction over the experimental platform of Gipsa-lab.

Two types of creep models (based on static logarithmic nonlinearity and a dynamic linear model) have been proposed in the literature, which have already been mentioned in Chapter 2. In the next section, we will show how this effect can be handled, together with hysteresis, via an RST controller.

5.3.3   Controller design for scanning (horizontal) movement of piezoelectric actuator

For the purpose of horizontal scanning control, an RST controller again based on pole placement with sensitivity functions shaping is designed, considering model Eq. (5.2.4) for the dynamics. The proposed controller design methodology is already explained in Chapter 3. In short, here the closed-loop dominant poles (P_D) are placed at $200\,Hz$ with damping coefficient of 0.9. A single high frequency real pole P_F is added at 0.2 and an integrator is used for H_S fixed part of the controller in order to achieve zero steady-state error. The achieved closed loop responses are given in Fig. 5.7 and Fig. 5.8.

Fig. 5.7 shows a good closed-loop tracking of a reference scanning signal in horizontal x-direction and also it can be observed that the hysteresis phenomenon is dealt with the designed controller. However, a fast scanning speed in horizontal x-direction can not eliminate completely the hysteresis phenomenon as shown in the second part of Fig. 5.7. Fig. 5.8 shows that the feedback control law also virtually eliminates the phenomenon of creep and the system tracks the constant reference signal.
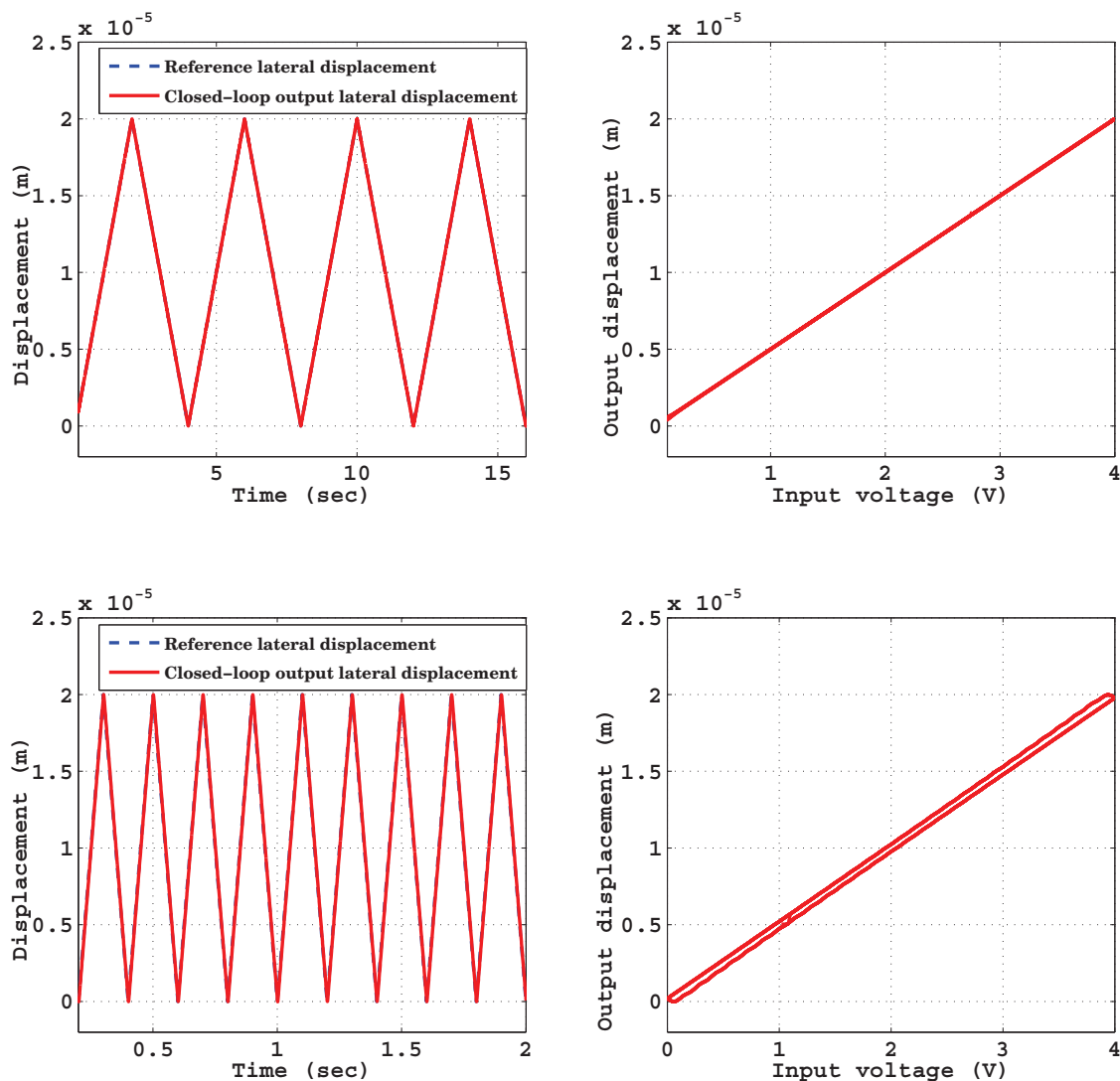
Figure 5.7: Experimental result of closed-loop reference tracking and observed *hysteresis* loop for the horizontal movement of the piezoelectric actuator.

5.4   Cross-Coupling Effects and Compensation

In this section, the measurement precision of the tunneling current in vertical z-direction is analyzed while scanning in horizontal x-direction in the presence of cross-coupling phenomenon.
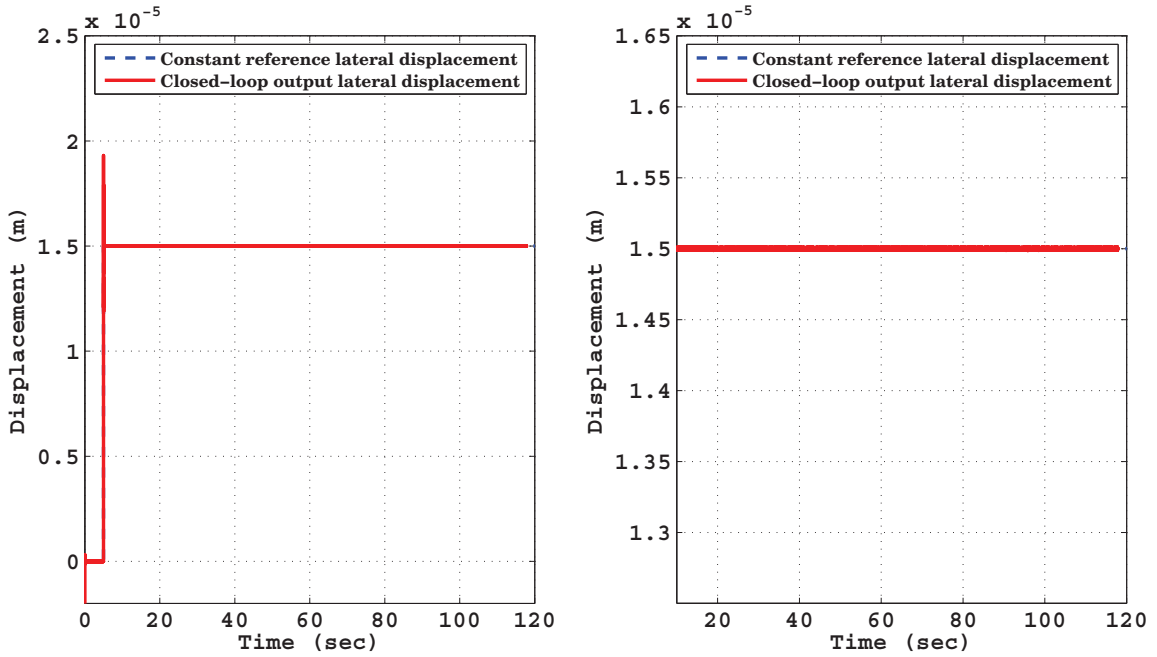
Figure 5.8: Experimental result of closed-loop step response for the horizontal movement of the piezoelectric actuator with compensation of *creep* phenomenon.

5.4.1 Cross-coupling effects on tunneling current measurement

The controller design for the considered system of tunneling current in the vertical z-direction is discussed in Chapter 3 and experimentally validated in Chapter 4. The controller design for horizontal x-direction (scanning) is discussed in previous section. Here, the purpose is to analyze the performance of these controllers in the presence of the coupling phenomenon. The general feedback block diagram is shown in Fig. 5.9.

Some simulation results are presented with maximum scanning speed of 100 Hz and different scanning range in horizontal x-direction. Fig. 5.10 shows the simulation result with scanning range of 0.01 μm. The desired tunneling current value was 0.5 nA and the maximum $\pm 10\%$ variations was allowed in the tunneling current (i_t). It can be observed that the tunneling current variation remains within the desired limits. If a simulation is performed with a slightly larger scanning range 0.05 μm as presented in Fig. 5.11, it can be observed that the variation in tunneling current becomes unacceptable because of the coupling based positioning error in vertical z-direction. More increase in scanning range
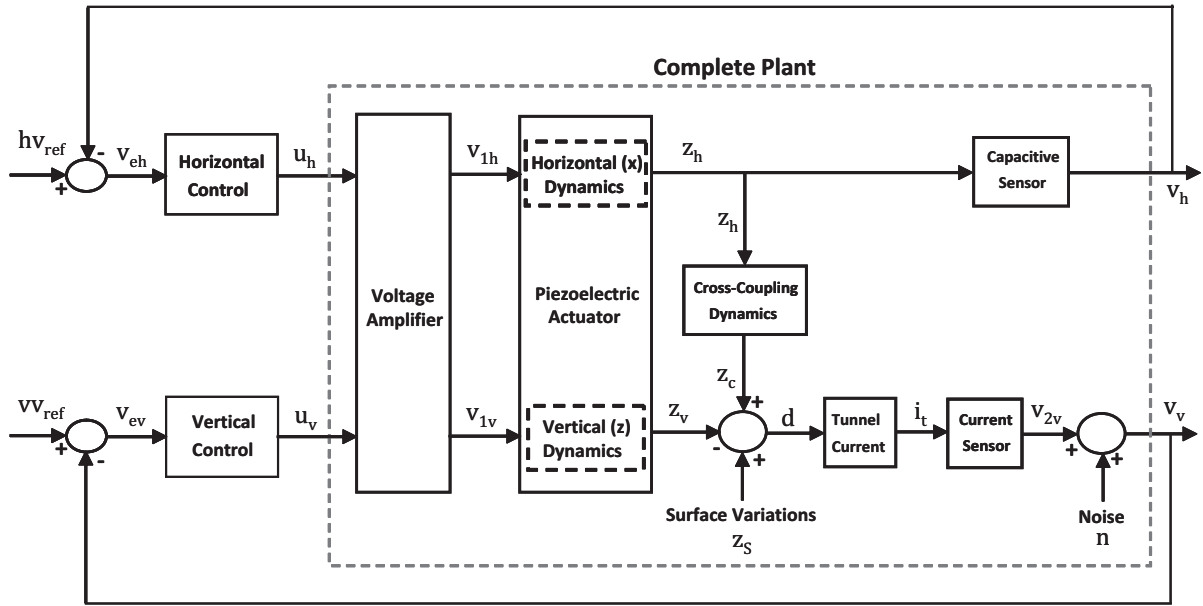
Figure 5.9: Complete block diagram of MIMO plant with individual controllers for horizontal and vertical directions in the presence of cross-coupling dynamics.

(*e.g.* 0.1 μm) causes more variation in the tunneling current as shown in Fig. 5.12.

One possible solution, proposed in the next section, is to design a MIMO controller by considering the dynamics of the system in the horizontal x-direction, the vertical z-direction and the cross-coupling effect, as depicted by Fig. 5.13.

5.4.2 LQR control design for MIMO system

In this subsection, a Linear Quadratic Regulator (LQR) approach is considered as a first solution for the MIMO control of the plant described by Eq. (5.2.16) of the considered system of tunneling current, having horizontal, vertical and cross-coupling dynamics. The general block diagram of the feedback loop considered here is shown in Fig. 5.13.

Complete details about LQR controller design can be found for instance in [Zhou et al., 1996], the main features are briefly recalled here. Consider a general linear time-invariant system:

$$\begin{cases} \dot{x} &= Ax + Bu \\ y &= Cx + Du \end{cases} \qquad (5.4.1)$$

with state vector, $x(t) \in \mathbf{R}^n$, input vector, $u(t) \in \mathbf{R}^m$ and output vector $y(t) \in \mathbf{R}^l$. If
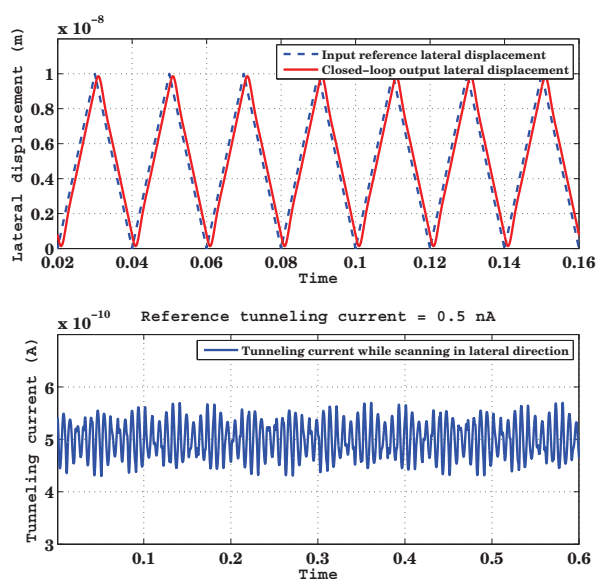
Figure 5.10: Simulation result with horizontal scanning speed of 100 Hz, scanning range of **0.01** μ**m** and corresponding tunneling current variations in vertical z-direction in the presence of sinusoidal surface variations (z_S) of frequency of 800 rad/sec (127.32 Hz) and an amplitude of 0.5 Å.
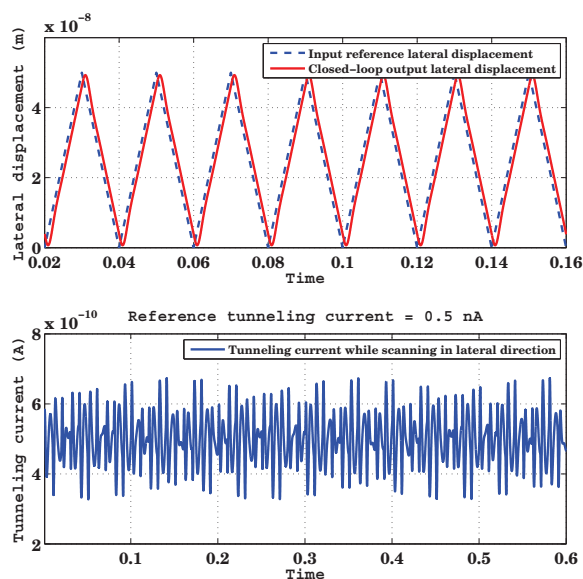
Figure 5.11: Simulation result with horizontal scanning speed of 100 Hz, scanning range of **0.05** μ**m** and corresponding tunneling current variations in vertical z-direction in the presence of sinusoidal surface variations (z_S) of frequency of 800 rad/sec (127.32 Hz) and an amplitude of 0.5 Å.
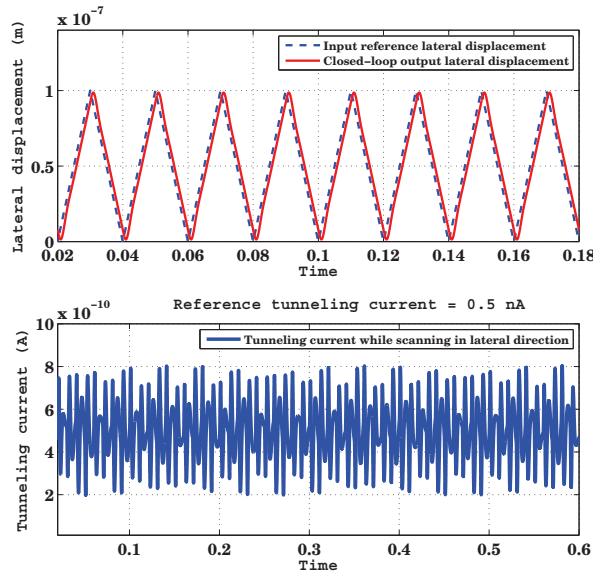
Figure 5.12: Simulation result with horizontal scanning speed of 100 Hz, scanning range of **0.1** μ**m** and corresponding tunneling current variations in vertical z-direction in the presence of sinusoidal surface variations (z_S) of frequency of 800 rad/sec (127.32 Hz) and an amplitude of 0.5 Å.
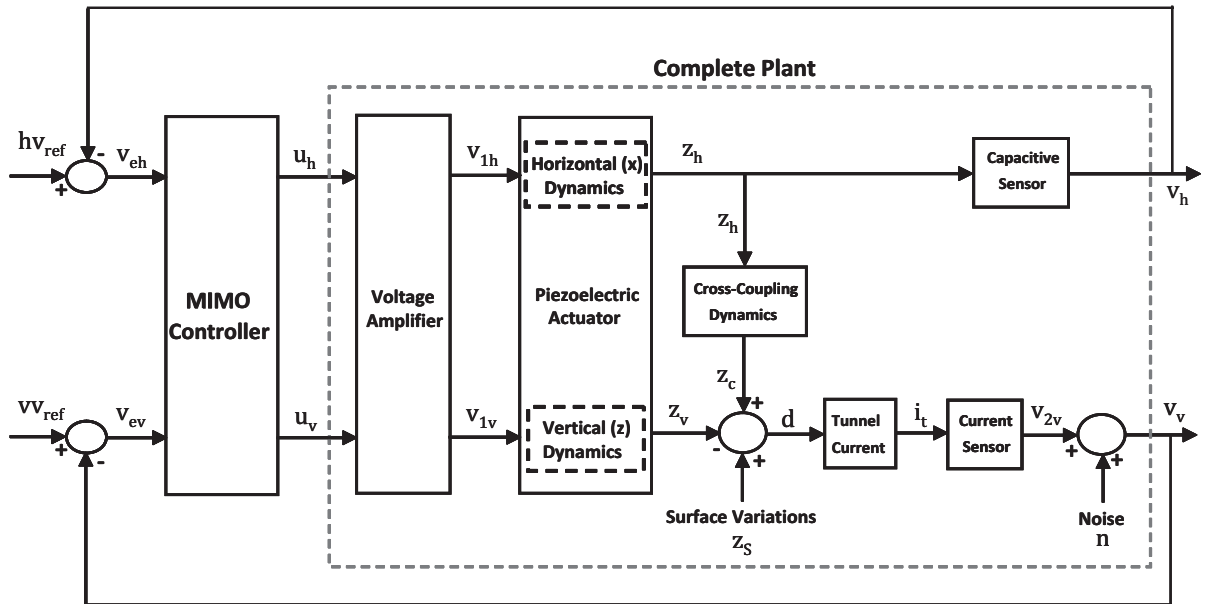

Figure 5.13: Complete general block diagram of MIMO plant with MIMO controller for horizontal and vertical directions in the presence of cross-coupling dynamics.

all the states are measurable, the state feedback:

$$u = -Kx \qquad (5.4.2)$$

with state feedback gain matrix, $K \in \mathbf{R}^{m \times n}$, can be applied to obtain desirable closed loop dynamics:

$$\dot{x} = (A - BK)x \tag{5.4.3}$$

For LQR control, the following cost function is defined:

$$J = \frac{1}{2} \int_0^\infty [x(t)^T Q x(t) + u(t)^T R u(t)] \, dt \tag{5.4.4}$$

By substituting Eq. (5.4.2) into Eq. (5.4.4):

$$J = \frac{1}{2} \int_0^\infty x(t)^T (Q + K^T R K) x(t) \, dt \tag{5.4.5}$$

The objective of LQR control is to find a state feedback gain matrix (K), such that the cost function Eq. (5.4.5) is minimized. In Eq. (5.4.5), the matrix $Q \in \mathbf{R}^{n \times n}$ is a weighting matrix for the states and matrix $R \in \mathbf{R}^{m \times m}$ is a weighting matrix for the input signals. Q should be selected to be positive semi-definite and R to be positive definite. The optimal solution is classically given by:

$$K = R^{-1} B^T P \tag{5.4.6}$$

with P obtained by solving:

$$A^T P + P A + Q - P B R^{-1} B^T P = 0 \tag{5.4.7}$$

This result is the Algebraic Riccati Equation (ARE).

Summarizing, the procedure to find the LQR state feedback gain matrix K is:

- Select the weighting matrices Q and R;

- Solve Eq. (5.4.7) to find P;

- Compute K using Eq. (5.4.6).

With this, the optimal feedback $u = -R^{-1} B^T P x$ is obtained.

Application

For the considered system of tunneling current, the complete MIMO plant model is given in (5.2.16), where $x(t) \in \mathbf{R}^4$, input vector, $u(t) \in \mathbf{R}^2$ and output vector $y(t) \in \mathbf{R}^2$. In order to compensate for possible static errors, an integral action can be included in the control as usual. For the considered MIMO plant, having two inputs (u_h and u_v) and two outputs (v_h and v_v), two integral actions are included by defining the extended system as follows: $A_e = \begin{pmatrix} A & 0 \\ -C & 0 \end{pmatrix}$ and $B_e = \begin{pmatrix} B \\ 0 \end{pmatrix}$ where $A_e \in \mathbf{R}^{6 \times 6}$ and $B_e \in \mathbf{R}^{6 \times 2}$. The two weighting matrices $Q \in \mathbf{R}^{6 \times 6}$ and $R \in \mathbf{R}^{2 \times 2}$ are tuned in order to achieve the desirable closed-loop results.

Fig. 5.14 shows the simulation result with the proposed LQR controller in the presence of maximum scanning speed of $100\,Hz$ and the scanning range of $0.1\,\mu m$ in the horizontal x-direction. For vertical z-direction, the desired tunneling current value was again $0.5\,nA$. It can be observed that with this large scanning range in the horizontal x-direction, the tunneling current variation in the vertical z-direction remains within the desired limits (the maximum $\pm 10\%$ variation allowed). This simulation result shows the improvement in the performance as compared to (Fig. 5.12) individual controllers for each direction for the considered system of tunneling current.

The control could be of course improved by extending the approach to robust techniques.

5.5 Conclusion

In this chapter, the vertical system (tunneling current measurement) and horizontal system (scanning) have been considered together, in the presence of cross-coupling phenomenon. In the first section, the coupling-caused positioning error in vertical z-direction has been highlighted. Then, a corresponding dynamic modeling of MIMO plant has been proposed in the next section.

The dynamic nonlinearities (hysteresis and creep) of the piezoelectric actuator have
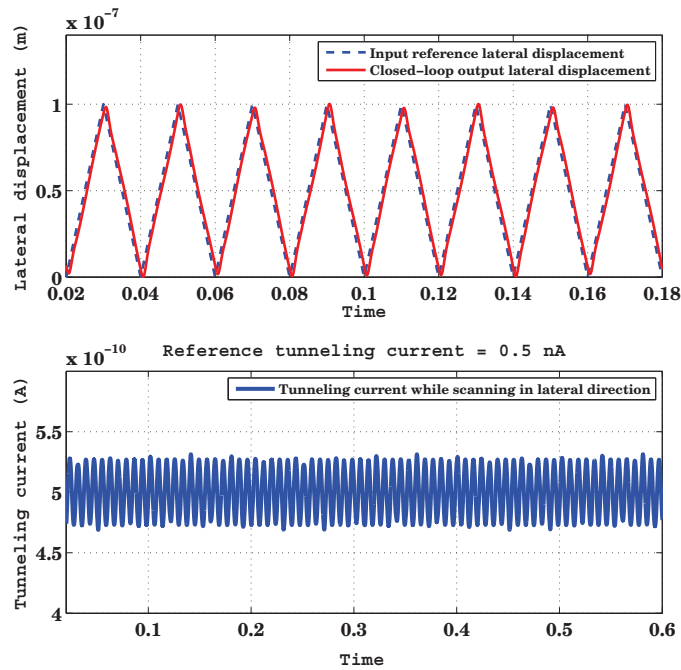
Figure 5.14: With MIMO control, the horizontal scanning speed of 100 Hz with scanning range of **0.1** μ**m** and corresponding tunneling current variations in vertical z-direction in the presence of sinusoidal surface variations (z_S) of frequency of 800 rad/sec (127.32 Hz) and an amplitude of 0.5 Å.

been experimentally observed, while scanning in the horizontal x-direction. A controller based on pole placement with sensitivity function shaping has been designed and experimentally validated in order to achieve better tracking. The creep phenomenon has been eliminated by the proposed control design and the nonlinear hysteresis phenomenon has been reduced, although fast tracking in the horizontal x-direction still requires a better control scheme in the presence of the hysteresis phenomenon. A lot of research has already been done in this particular area, which has been highlighted in Chapter 2.

Finally, the coupling-caused positioning error for the tunneling current measurement system in the vertical z-direction has been analyzed in simulations in the presence of individual controllers and also with MIMO LQR controller for the horizontal and the vertical directions. The variation of tunneling current has been observed within the desired limits with the proposed MIMO LQR controller better than with the individual controllers, in the presence of fast speed with large scanning range in the horizontal

x-direction.

GENERAL CONCLUSION AND PERSPECTIVES

General Conclusion

The main idea behind this work was to provide a contribution to an emerging domain of *nanotechnology* from control point of view. The tunneling current phenomenon, which occurs at nanometer scale and can be of strong interest for actual applications, was chosen for this purpose. Based on this phenomenon, an experimental platform has been developed in Gipsa-lab Grenoble by the control group allowing to validate the control techniques (at ambient atmosphere) proposed in the present work.

In the first part of this work, the tunneling current phenomenon has been explained and corresponding applications have been highlighted. Nanopositioning is required for the precise measurement of the tunneling current. The problems associated with the nanopositioning in terms of precision, bandwidth, robustness, actuator nonlinearities and cross-coupling issues have been presented, and then analyzed for the considered system of tunneling current in the other parts of the work.

A dynamic modeling corresponding to the considered system has been proposed and desired performance requirements have been translated into control requirements. Two robust control techniques, firstly pole placement with sensitivity function shaping method and then mixed-sensitivity H$_\infty$ approach, have been used and a comparison with the more conventionally used classical PI controller has been performed in simulations. The comparison results for the considered system of tunneling current have confirmed better performances in terms of precision and disturbance rejection with the proposed controllers than with the PI.

The challenging part of this work was the experimental validation (at ambient atmosphere) of the proposed control schemes, while working at nanometer scale by keeping the distance between two electrodes (tip and sample surface) less than 1×10^{-9} m without contact. This part of the work started with the system identification, went on with obtaining experimental results in time and frequency domains, finally allowing for an experimental comparison between the proposed and conventional control techniques. The experimental results have shown stronger attenuation of external disturbances for a large

band of frequencies with the proposed H_∞ control, even providing a larger closed loop bandwidth, as compared with the proposed controller designed by pole placement with sensitivity function shaping and the conventional PI control.

One of the great applications of tunneling current is to scan a sample surface with atomic scale resolution. This scanning (in horizontal x-direction) introduces the problem of actuator nonlinearities and also positioning error for the tunneling current measurement (in vertical z-direction) because of the actuator cross-coupling. These issues have been discussed in the last part of this work. Experimental results with the proposed control design based on pole placement with sensitivity function shaping method for horizontal x-direction have shown an attenuation of actuator nonlinearities effects. Finally, a Linear Quadratic Regulator (LQR) approach has been analyzed in simulation for the MIMO control of the plant having horizontal, vertical and cross coupling dynamics. Less variations in the tunneling current has been observed with the proposed MIMO controller as compared to the individual controllers for each direction (horizontal x-direction and vertical z-direction) for the considered system of tunneling current.

Perspectives

In view of the results obtained in this work, various perspectives can be thought of which are listed below:

Considering the dynamics of the piezoelectric actuator (120 kHz), modifications in the hardware can be made in order to achieve large closed-loop bandwidth by increasing the bandwidth of the voltage amplifier (4 kHz) (which was the limiting bandwidth in vertical z-direction) and also the tunneling current sensor (13 kHz) (at the cost of a lower gain). Another issue of the hardware was with the data acquisition cards which introduced the limitation of the sampling frequency (30 kHz) and didn't allow to work with high order controllers. Field-Programmable Gate Array (FPGA) technology could be exploited for high speed data acquisition.

During power spectral density analysis of the measured tunneling current, a peak at

low frequency (around 350 Hz) was observed in all the tests with all type of controllers. The amplitude of the peak varied in different tests. The reason of this peak seems to be experimental, although the exact reason is not determined yet which needs to be identified to further enhance the performance. A Notch filter [Procházka & Landau, 2003] can be introduced as the fixed part of the controller, at the cost of increasing the order of the controller by two.

Exact model of cross-coupling dynamics needs to be identified. Unfortunately, tunneling current is not a good sensor to accurately identify the coupling-caused positioning error in the vertical z-direction. By scanning in the horizontal x-direction, the variations in the tunneling current can be because of the coupling-caused positioning error and in the same time, because of the sample surface variations. The proposed MIMO controller needs to be validated experimentally, after the identification of cross-coupling dynamics. The control can of course be improved by extending the approach to robust MIMO control techniques.

This thesis was focused on the analysis of tunneling current measurement, although for scanning in horizontal x-direction, the experimentally observed hysteresis phenomenon can be modeled and then compensated (many related work is highlighted in Chapter 2) in order to enhance the tracking performance. The same holds for the creep phenomenon of the piezoelectric actuator.

The experimental platform allows for the situation with an oscillating sample surface, the analysis of the performance of the tunneling current measurement system in such a configuration is also a perspective of interest.

More generally, the impact of a better tunneling current measurement can be analyzed in various other applications, and for instance when using tunneling current as a displacement sensor in the presence of the electrostatic actuator as in [Blanvillain, 2010].

Appendix 1: Some experimental problems with tunneling current
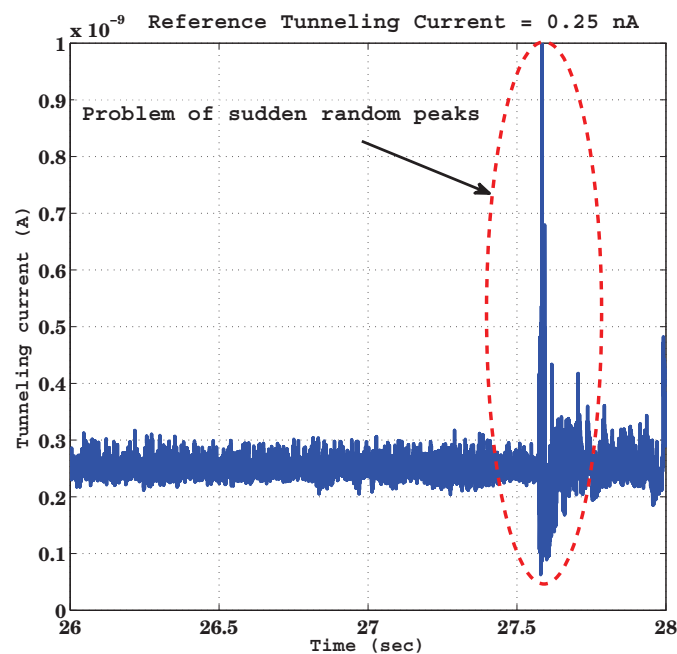
Figure 6.1: Random peaks in the measurement signal

Among the experimental problems that could disturb an operation, one can mention the occurrence of sudden and unexpected peaks in the measurement signal (Fig. 6.1, Fig. 6.2). Here are some possible practical remedies to this:

- Environmental conditions play vital role while working at nanometer scale. External disturbances must be avoided as much as possible and the experiment should not be performed while there are movement of heavy vehicles in the surroundings of the experimental lab.
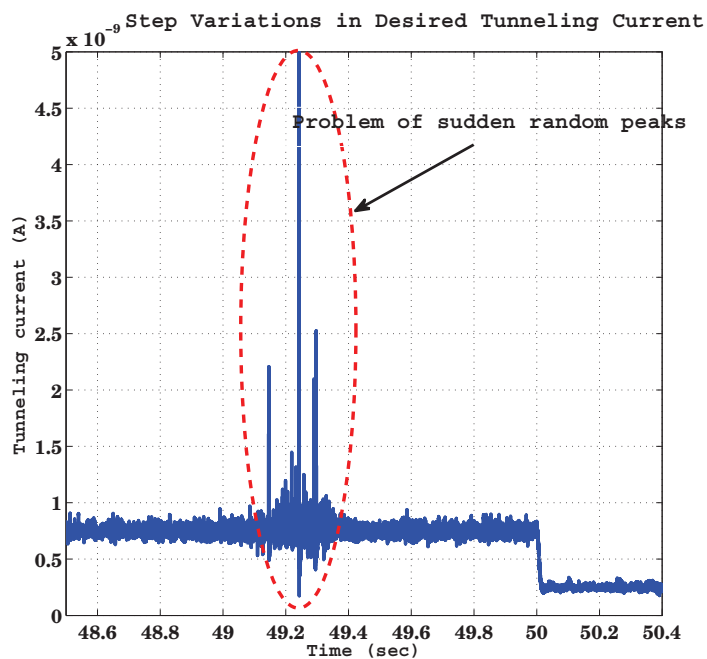
Figure 6.2: Random peaks in the measurement signal
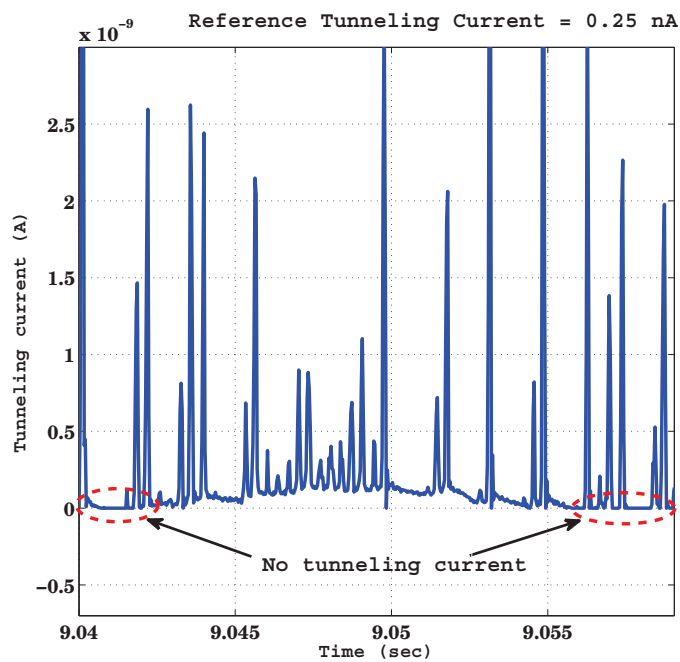
Figure 6.3: Undesire-able response of tunneling current with random peaks, no tunneling current and large variations

- The lateral position of the tip over the sample surface can be changed with the help of precision micrometer screws.

- The sample surface can be cleaned.

- If the problem as shown in Fig. 6.3 occurs, the tip and/or sample surface can be changed.

Bibliography

Abramovitch, D. Y., Andersson, S. B., Pao, L. Y. & Schitter, G. [2007], A tutorial on the mechanisms, dynamics, and control of Atomic Force Microscopes, *in* '*American Control Conference, New York City, USA*'.

Al Janaideh, M., Feng, Y., Rakheja, S., Su, C. & Rabbath, C. [2009], Hysteresis compensation for smart actuators using inverse generalized prandtl-ishlinskii model, *in* 'American Control Conference, 2009. ACC'09.', IEEE, pp. 307–312.

Ang, W. T., Khosla, P. K. & Riviere, C. N. [2007], 'Feedforward controller with inverse rate-dependent model for piezoelectric actuators in trajectory-tracking applications', *IEEE Transactions on Mechatronics* **12**(2), 134–142.

Anguiano, E., Oliva, A. & Aguilar, M. [1998], 'Optimal conditions for imaging in scanning tunneling microscopy : Theory', Review of Scientific Instruments **69**(2), 3867–3874.

Anguiano, E., Oliva, A., Aguilar, M. & Pena, J. [1996], 'Analysis of scanning tunneling microscopy feedback system : Experimental determination of parameters', Review of Scientific Instruments **67**(8), 2947–2952.

Aphale, S. S., Bhikkaji, B. & Moheimani, S. O. R. [2008], 'Minimizing scanning errors in piezoelectric stack-actuated nanopositioning platforms', *IEEE Transactions on Nanotechnology* **7**(1), 79–90.

Aphale, S. S., Devasia, S. & Moheimani, S. O. R. [2008], 'High-bandwidth control of a piezoelectric nanopositioning stage in the presence of plant uncertainties', *Nanotechnology* **19**(12).

Balas, M. [1978], 'Active control of flexible systems', Journal of Optimizing Theory and Applications **25**(3), 415–436.

Bardeen, J. [1961], 'Tunnelling from a many-particle point of view', *Physical Review Letters* **6**(2), 57–59.

Besançon, G., Voda, A. & Chevrier, J. [2004], Force estimation in fundamental physics: an observer application, *in 'IFAC Symposium on System, Structure and Control, Oaxaca, Mexico'*.

Besançon, G., Voda, A. & Colinet, E. [2007], Towards oscillation control in a vibrating cantilever nonlinear NEMS, *in 'European Control Conference, Greek'*.

Besançon, G., Voda, A. & Jourdan, G. [2009], Kalman observer approach towards force reconstruction from experimental afm measurements, *in '15th IFAC Symposium on System Identification (SYSID), Saint-Malo, France'*.

Bhikkaji, B., Ratnam, M., Fleming, A. J. & Moheimani, S. O. R. [2007], 'High-performance control of piezoelectric tube scanners', IEEE Transactions on Control Systems Technology **15**(5), 853–866.

Bhikkaji, B., Ratnam, M. & Moheimani, S. O. R. [2007], 'PVPF control of piezoelectric tube scanners', Sensors and Actuators **135**(2), 700–712.

Binnig, G. & Rohrer, H. [1986], 'Scanning tunneling microscopy', IBM J. Res. Develop. **30**, 355–369.

Binnig, G., Rohrer, H., Gerber, C. & Weibel, E. [1982], 'Surface studies by scanning tunneling microscopy', *Physical Review Letters* **49**(1), 57–61.

Binnig, G. & Smith, D. [1986], 'Single-tube three-dimensional scanner for scanning tunneling microscopy', Review of Scientific Instruments **57**(8), 1688–1689.

Blanvillain, S. [2010], Contrôle nanoscopique du mouvement par courant tunnel : étude et réalisation, PhD thesis, UJF, Grenoble.

Bibliography

Blanvillain, S., Voda, A., Besancon, G. & Buche, G. [2009], The tunnel current as a subnanometer motion sensor, *in* 'European Control Conference, Budapest, Hungry'.

Bocko, M. F. [1990], 'The scanning tunneling microscope as a high-gain, low-noise displacement sensor', Review of Scientific Instruments **61**(12), 3763–3768.

Bonnail, N. [2001], Analyse de données, modélisation et commande pour la microscopie en champ proche utilisant des actionneurs piézoélectriques, PhD thesis, Universite de la Mediterranee Aix-Marseille II.

Bonnail, N., Tonneau, D., Capolino, G. A. & Dallaporta, H. [2000], Dynamic and static responses of a piezoelectric actuator at nanometer scale elongations, *in* 'Industry Applications Conference, Rome, Italy'.

Bonnail, N., Tonneau, D., Jandard, F., Capolino, G. A. & Dallaporta, H. [2004], 'Variable structure control of a piezoelectric actuator for a scanning tunneling microscope', *IEEE transaction on Industrial Electronics* **51**(2), 354–363.

Bordoni, F. & Karim, M. [1994], 'Fundamental noise, electromechanical transduction and their role in resonant gravitational-wave detectors', Classical and Quantum Gravity **11**(6A), 61–72.

Bredekamp, A. & Tapson, J. [1999], *A scanning tunneling microscope control system with potentiometric capability*, Vol. 1, IEEE.

Bredekamp, A. & Tapson, J. [n.d.], A scanning tunneling microscope control system based on fast microcontrollers, *in* 'Communications and Signal Processing, 1998. COMSIG'98. Proceedings of the 1998 South African Symposium on', IEEE, pp. 225–228.

Brokate, M. & Sprekels, J. [1996], *Hysteresis and phase transitions*, Springer.

Butterworth, J., Pao, L. & Abramovitch, D. [2009], 'A comparison of control architectures for atomic force microscopes', *Asian Journal of Control* **11**(2), 175–181.

Bibliography

Chen, C. J. [2008], *Introduction to Scanning Tunneling Microscopy, Oxford University Press.*

Chen, X., Su, C.-Y. & Fukuda, T. [2008], 'Adaptive control for the systems preceded by hysteresis', *IEEE Transactions on Automatic Control* **53**(4), 1019 –1025.

Croft, D., Shed, G. & Devasia, S. [2001], 'Creep, hysteresis, and vibration compensation for piezoactuators: Atomic force microscopy application', *Journal of Dynamic Systems, Measurement, and Control* **123**, 35.

Curtis, R., Mitsui, T. & Ganz, E. [1997], 'An ultrahigh vacuum high speed scanning tunneling microscope', *Review of Scientific Instruments* **68**(7), 2790–2796.

Devasia, S., Eleftheriou, E. & Moheimani, S. O. R. [2007], 'A survey of control issues in nanopositioning', *IEEE Transactions on Control Systems Technology* **15**(5), 802 – 823.

Ekinci, K. L. [2005], 'Electromechanical transducers at the nanoscale: Actuation and sensing of motion in nanoelectromechanical systems (NEMS)', Small **1**(8-9), 786– 797.

El Feninat, F., Ellis, T., Sacher, E. & Stangel, I. [2001], 'A tapping mode afm study of collapse and denaturation in dentinal collagen', *Dental Materials* **17**(4), 284–288.

Fowler, R. & Nordheim, L. [1928], 'Electron emission in intense electric fields', *Proceedings of the Royal Society of London. Series A, Containing Papers of a Mathematical and Physical Character* **119**(781), 173–181.

Gao, W., Hocken, R. J., Patten, J. A., Lovingood, J. & Lucca, D. [2000], 'Construction and testing of a nanomachining instrument', *Precision Engineering* **24**(4), 320–328.

Hodgdon, M. [1988*a*], 'Applications of a theory of ferromagnetic hysteresis', IEEE Transactions on Magnetics **24**(1), 218–221.

Hodgdon, M. [1988*b*], 'Mathematical theory and calculations of magnetic hysteresis curves', IEEE Transactions on Magnetics **24**(6), 3120–3122.

Bibliography

Hooge, F. N. [1969], '1/f noise is no surface effect', Physics Letters **29**(3), 139–140.

Hu, H. & Mrad, R. B. [2002], 'On the classical preisach model for hysteresis in piezoceramic actuators', *Mechatronics* **13**(2), 85 – 94.

Iyer, R. & Tan, X. [2009], 'Control of hysteretic systems through inverse compensation', *IEEE Control Systems Magazine* **29**(1), 83–99.

Janaideh, M. A., Rakheja, S. & Su, C.-Y. [2009], 'Experimental characterization and modeling of rate-dependent hysteresis of a piezoceramic actuator', *Mechatronics* **19**(5), 656 – 670.

Janaideh, M. A., Su, C. Y. & Rakheja, S. [2008], 'Development of the rate-dependent prandtl-ishlinskii model for smart actuators', *Smart Materials and Structures* **17**(3), 035026.

Jandt, K. D., Finke, M. & Cacciafesta, P. [2000], 'Aspects of the physical chemistry of polymers, biomaterials and mineralised tissues investigated with atomic force microscopy', *Colloids Surfaces B-Biointerfaces* **19**(4), 301–314.

Jiles, D. & Thoelke, J. [1989], 'Theory of ferromagnetic hysteresis: determination of model parameters from experimental hysteresis loops', IEEE Transactions on Magnetics **25**(5), 3928–3930.

Johnson, J. B. [1925], *Physics Review* **26**, 77.

Johnson, J. B. [1928], 'Thermal agitation of electricity in conductors', Physics Review **32**, 97–109.

Jung, H., Shim, J. & Gweon, D. [2000], 'New open-loop actuating method of piezoelectric actuators for removing hysteresis and creep', *Review of Scientific Instruments* **71**(9), 3436–3440.

Kassies, R., der Werf, K. O. V., Lenferink, A., Hunter, C. N., Olsen, J. D., Subramaniam, V. & Otto, C. [2005], 'Combined AFM and confocal fluorescence microscope for applications in bio-nanotechnology', *Journal of Microscopy* **217**, 109–116.

Bibliography

Katzir, S. [2006], 'The discovery of the piezoelectric effect', *THE BEGINNINGS OF PIEZOELECTRICITY* pp. 15–64.

Kenny, T., Kaiser, W., Rockstad, H., Reynolds, J., Podosek, J. & Vote, E. [1994], 'Wide-bandwidth electromechanical actuators for tunneling displacement transducers', *Microelectromechanical Systems, Journal of* **3**(3), 97–104.

Krasnoskl'skii, M. A. [1983], *Systems with hysteresis*, Springer.

Lagoute, J. [2003], Images et fluctuations du courant sur surfaces métalliques et fils moléculaires adsorbés en microscopie à effet tunnel, PhD thesis, Université Toulouse III.

Landau, I. D. & Karimi, A. [1998], 'Robust digital control using pole placement with sensitivity function shaping method', International Journal of Robust and Nonlinear Control **8**, 191–210.

Landau, I. D. & Zito, G. [2006], *Digital Control Systems: design, identification and implementation*, *Springer*.

Landau, L. D. & Lifshitz, E. M. [1977], *Quantum Mechanics*, Pergamon Press, Oxford.

Liaw, H. C., Shirinzadeh, B. & Smith, J. [2008], 'Sliding-mode enhanced adaptive motion tracking control of piezoelectric actuation systems for micro/nano manipulation', *IEEE Transactions on Control Systems Technology* **16**(4), 826 –833.

Libioulle, L., Houbion, Y. & Gilles, J. M. [1995], 'Very sharp platinum tips for scanning tunneling microscopy', *Review of Scientific Instruments* **66**(1), 97–100.

Liboff, R. [1998], *Introductory quantum mechanics*, Addison-Wesley.

Lin, F.-J., Shieh, H.-J., Huang, P.-K. & Teng, L.-T. [2006], 'Adaptive control with hysteresis estimation and compensation using rfnn for piezo-actuator', *IEEE Transactions on Ultrasonics, Ferroelectrics and Frequency Control* **53**(9), 1649 –1661.

Bibliography

Liu, C. H., Barzilai, A. M., Reynolds, J. K., Partridge, A., Kenny, T. W., Grade, J. D. & Rockstad, H. K. [1998], 'Characterization of a high-sensitivity micromachined tunneling accelerometer with micro-g resolution', Journal of Microelectromechanical Systems **7**(2), 235 –244.

Liu, C. H. & Kenny, T. W. [2001], 'A high-precision, wide-bandwidth micromachined tunneling accelerometer', Journal of Microelectromechanical Systems **10**(3), 425 – 433.

Liu, C., Rockstad, H. & Kenny, T. [1999], Robust controller design via μ-synthesis for high-performance micromachined tunneling accelerometers, *in* 'American Control Conference, 1999. Proceedings of the 1999', Vol. 1, IEEE, pp. 247–252.

Macki, J. W., Nistri, P. & Zecca, P. [1993], 'Mathematical models for hysteresis', Society for Industrial and Applied Mathematics **35**(1), 94–123.

Maess, J., Fleming, A. & Allg
"ower, F. [2008], 'Simulation of dynamics-coupling in piezoelectric tube scanners by reduced order finite element analysis', *Review of Scientific Instruments* **79**, 015105.

Mahmood, I. & Moheimani, S. [2009], 'Making a commercial atomic force microscope more accurate and faster using positive position feedback control', *Review of Scientific Instruments* **80**, 063705.

Mayergoyz, I. D. [2003], *Mathematical models of hysteresis and their applications*, Elsevier.

Mayergoyz, I. & Friedman, G. [1988], 'Generalized preisach model of hysteresis', IEEE Transactions on Magnetics **24**(1), 212–217.

Nakakura, C. Y., Phanse, V. M., Zheng, G., Bannon, G., Altman, E. I. & Lee, K. P. [1998], 'A high-speed variable-temperature ultrahigh vacuum scanning tunneling microscope', Review of Scientific Instruments **69**(9), 3251–3258.

Nyquist, H. [1928], 'Thermal agitation of electric charge in conductors', *Physics Review* **32**, 110–113.

Bibliography

Ohara, T. & Youcef-Toumi, K. [1995], Dynamics and control of piezotube actuators for subnanometer precision applications, *in* 'American Control Conference, 1995. Proceedings of the', Vol. 5, IEEE, pp. 3808–3812.

Oliva, A., Anguiano, E., Denisenko, N., Aguilar, M. & Pena, J. [1995], 'Analysis of scanning tunneling microscopy feedback system', Review of Scientific Instruments **66**(5), 3196–3203.

Oropeza-Ramos, L., Kataria, N., Burgner, C., Astr
"om, K., Brewer, F. & Turner, K. [2008], Noise analysis of a tunneling accelerometer based on state space stochastic theory, *in* 'Solid-State Sensor, Actuator, and Microsystems Workshop, Hilton Head, SC'.

Pao, L., Butterworth, J. & Abramovitch, D. [2007], Combined feedforward/feedback control of atomic force microscopes, *in* 'American Control Conference, 2007. ACC'07', IEEE, pp. 3509–3515.

Pare, T. & J.P.How [1998], Robust stability and performance analysis of systems with hysteresis nonlinearities, *in* 'IEEE International American Control Conference, Pennsylvanla'.

Procházka, H. & Landau, I. [2003], 'Pole placement with sensitivity function shaping using 2nd order digital notch filters', *Automatica* **39**(6), 1103–1107.

Ratnam, M., Bhikkaji, B., Fleming, A. & Moheimani, S. [2005], PPF control of a piezoelectric tube scanner, *in* '44th IEEE Conf. Decision & Control Eur. Control Conf., Seville, Spain'.

Rockstad, H. K., Tang, T. K., Reynolds, J. K., Kenny, T. W., Kaiser, W. J. & Gabrielsond, T. B. [1996], 'A miniature, high-sensitivity, electron tunneling accelerometer', Sensors and Actuators **53**(1-3), 227–231.

Rogers, B. L., Shapter, J. G., Skinner, W. M. & Gascoigne, K. [2000], 'A method for production of cheap, reliable Pt-Ir tips', Review of Scientific Instruments **71**(4), 1702–1705.

Sain, P., Sain, M. & Spencer, B. [1997], Models for hysteresis and application to structural control, *in* 'IEEE International American Control Conference, Albuquerque, NM, USA'.

Salapaka, S. & Sebastian, A. [2003], Control of the nanopositioning devices, *in* 'IEEE Conference on on Decision and Control, Hawaii, USA'.

Salapaka, S., Sebastian, A., Cleveland, J. P. & Salapaka, M. V. [2002], 'High bandwidth nano-positioner: a robust control approach', *Review of Scientific Instruments* **73**(9), 3232–3241.

Salvini, A. & Fulginei, F. [2002], 'Genetic algorithms and neural networks generalizing the jiles-atherton model of static hysteresis for dynamic loops', IEEE Transactions on Magnetics **38**(2), 873–876.

Sasaki, A., Iwata, F., Katsumata, A., Akiyama, T. & Fujiyasu, H. [1997], 'A stable scanning tunneling microscope designed for investigations of organic thin films in air', Review of Scientific Instruments **68**(2), 1296–1299.

Schitter, G. & Stemmer, A. [2004], 'Identification and open-loop tracking control of a piezoelectric tube scanner for high-speed scanning probe microscopy', IEEE Transaction on Control System Technology **12**(3), 449–454.

Schottky, W. [1926], 'Small shot effect and flicker effect', *Physics Review* **28**, 74–103.

Sebastian, A. & Salapaka, S. M. [2005], 'Design methodologies for robust nanopositioning', IEEE Transactions on Control Systems Technology **13**(6), 868–876.

Shi, J., Wu, Y., Su, C. & Zou, Q. [2009], A control approach to cross coupling compensation of piezotube scanners in tapping-mode imaging, *in* 'Proceedings of SPIE', Vol. 7378, p. 73781E.

Shim, J. & Gweon, D. [2001], 'Piezo-driven metrological multiaxis nanopositioner', Review of Scientific Instruments **72**(11), 4183–4187.

Bibliography

Simmons, J. [1963], 'Generalized formula for the electric tunnel effect between similar electrodes separated by a thin insulating film', *Journal of Applied Physics* **34**(6), 1793–1803.

Skogestad, S. & Postlethwaite, I. [1996], *Multivariable Feedback Control: Analysis and design*, John Wiley & Sons.

Song, G., Zhao, J., Zhou, X. & De Abreu-García, J. [2005], 'Tracking control of a piezoceramic actuator with hysteresis compensation using inverse preisach model', *IEEE/ASME Transactions on Mechatronics* **10**(2), 198–209.

Sorensen, A. H., Hvid, U., Mortensen, M. W. & Morch, K. A. [1999], 'Preparation of platinum/iridium scanning probe microscopy tips', Review of Scientific Instruments **70**(7), 3059–3067.

Su, C. Y., Wang, Q., Chen, X. & Rakheja, S. [2005], 'Adaptive variable structure control of a class of nonlinear systems with unknown prandtl-ishlinskii hysteresis', IEEE Transactions on Automatic Control **50**(12), 2069–2074.

Sugita, S., Mera, Y. & Maeda, K. [1996], 'Origin of low frequency noise and 1/f fluctuations of tunneling current in scanning tunneling microscopes', *Journal of Applied Physics* **79**(8), 4166–4173.

Taylor, M. [1993], 'Dynamics of piezoelectric tube scanners for scanning probe microscopy', *Review of scientific instruments* **64**(1), 154–158.

Tersoff, J. & Hamann, D. [1983], 'Theory and application for the scanning tunneling microscope', *Physical review letters* **50**(25), 1998–2001.

Tien, S., Zou, Q. & Devasia, S. [2004], Control of dynamics-coupling effects in piezo-actuator for high-speed afm operation, *in* 'American Control Conference, 2004. Proceedings of the 2004', Vol. 4, IEEE, pp. 3116–3121.

Tsukada, M., Kobayashi, N., Brandbyge, M. & Nakanishi, S. [2000], 'Physics of artificial nano-structures on surfaces', *Progress in Surface Science* **64**(3-8), 139–155.

Bibliography

Visintin, A. [1994], *Differential models of hysteresis*, Springer.

Waltman, S. & Kaiser, W. [1989], 'An electron tunneling sensor', *Sensors and Actuators* **19**(3), 201–210.

Wang, J., Zhao, Y., Cui, T. & Varahramyan, K. [2002], 'Synthesis of the modeling and control systems of a tunneling accelerometer using the matlab simulation', *Journal of Micromechanics and Microengineering* **12**, 730.

Wang, Q. & Su, C. Y. [2006], 'Robust adaptive control of a class of nonlinear systems including actuator hysteresis with prandtl-ishlinskii presentations', *Automatica* **42**(5), 859–867.

Weinstein, V., Slutzky, M., Arenshtam, A. & Ben-Jacob, E. [1995], 'A method for preparation of Pt-Ir tips for the scanning tunneling microscope', *Review of Scientific Instruments* **66**(4), 3075–3076.

Wu, Y., Shi, J., Su, C. & Zou, Q. [2009], 'A control approach to cross-coupling compensation of piezotube scanners in tapping-mode atomic force microscope imaging', *Review of Scientific Instruments* **80**, 043709.

Yamanaka, K., Noguchi, A., Tsuji, T., Koike, T. & Goto, T. [1999], 'Quantitative material characterization by ultrasonic AFM', *Surface Interface Analysis* **27**(5-6), 600–606.

Yie, Z., Kataria, N., Burgner, C., Astrom, K., Brewer, F. & Turner, K. [n.d.], Control design for force balance sensors, *in* 'American Control Conference, 2009. ACC'09.', IEEE, pp. 4208–4214.

Zhou, K., Doyle, J., Glover, K. et al. [1996], *Robust and optimal control*, Vol. 40, Prentice Hall Upper Saddle River, NJ.